7-3-2023

Cast Iron Repair Through Directed Energy Deposition and Ancillary Processing Modes

Jakob D. Hamilton
jdh3685@rit.edu

RIT

Cast Iron Repair Through Directed Energy Deposition and Ancillary Processing Modes

A dissertation submitted in partial fulfillment of the requirements for the degree of Doctor of Philosophy in Mechanical and Industrial Engineering

Jakob D. Hamilton

B.S. Engineering Science, Wartburg College

M.S. Industrial and Systems Engineering, Rochester Institute of Technology

Kate Gleason College of Engineering
Rochester Institute of Technology
Rochester, New York
July 3rd, 2023

Cast Iron Repair Through Directed Energy Deposition and Ancillary Processing Modes
by
Jakob D. Hamilton

Committee Approval:
We, the undersigned committee members, certify that we have advised and/or supervised the candidate on the work described in this dissertation. We further certify that we have reviewed the dissertation manuscript and approve it in partial fulfillment of the requirements of the degree of Doctor of Philosophy in Engineering.

Dr. Iris V. Rivero (Advisor) Date
Department Head of Industrial and Systems Engineering and Kate Gleason Professor

---

Dr. Denis Cormier Date
Earl W. Brinkman Professor, AMPrint Center Director, Industrial and Systems Engineering

---

Dr. Yunbo Zhang Date
Assistant Professor, Industrial and Systems Engineering

Dr. Rui Liu Date
Assistant Professor, Mechanical Engineering

Dr. Scott Williams Date
Professor, School of Chemistry and Materials Science

Certified by:

Dr. Katie McConky Date
Director, PhD in Mechanical and Industrial Engineering

To my parents, Chris and Brenda,

my brothers, Alexander and Joshua,

and my cat Cece,

thank you.

Acknowledgement

First and foremost, I must thank my advisor Dr. Iris Rivero for years of guidance and wisdom in learning to conduct meaningful research. I am beyond grateful for the contributions, knowledge, and connections that have led to my success in the last five years. I feel well prepared to give back to the Industrial Engineering community in research, teaching, and advising capacities, and I am immensely grateful.

Next, I would also like to thank the Industrial and Systems Engineering Department, the Mechanical Engineering Department, and their respective faculty for providing the resources and expertise that allowed me to conduct research. Specifically, I owe many thanks to Dr. Denis Cormier for providing state-of-the-art equipment and research faculty through the AMPrint Center. I will miss the Hybrid, the SEM, the high-speed camera, and the CT scanner dearly. Additional faculty that I owe thanks include Dr. David Trauernicht, Dr. Will Zhang, Dr. Rui Liu, Dr. Scott Williams, Dr. Surendra Gupta, William Humphrey, Ted Kinsman, Jeremy Siegfried, and Dr. Michael Thurston. RIT has provided top-notch resources, and I am happy to direct future graduate students to the MIE programs. I also owe many thanks to engineering, physics, and mathematics professors during my time at Wartburg College, specifically, Dr. Daniel Black, Dr. LeAnn Faidley, Dr. Ben Bousquet, Dr. Mariah Birgen, and Dr. Brian Birgen.

I also owe thanks to our collaborators across the country that have cultivated years of fruitful research: Dr. Prahalada Rao at Virginia Tech, Dr. Leon Liao, Dr. Matt Frank, and Dr. Beiwen Li at Iowa State, Dr. Hantang Qin at the University of Wisconsin, and Dr. Ola Harrysson and Dr. Christopher Rock at NC State. Additionally, I have immense gratitude for Dr. Jason Jones, Nathan Northrup, Peter Coates, and all the Hybrid Manufacturing Tech. team for their continued support of our machine and research objectives. I also owe gratitude to Kenneth Court and Matthew Macchione of Advanced Atomization for their advice and lending of resources.

I would be remiss to forget to mention the team at Raytheon Technologies Research Center. Two summers in the AMPCC taught me endless fundamentals of powder bed fusion, in-situ monitoring,

optics, and numerical modeling. To Dr. Brian Fisher, I cannot thank you enough for the contributions to my own development as a researcher. Additional thanks are owed to Tom Skiba, Josh Norman, Dr. Faramarz Zarandi, and Dr. Venkat Vedula for supporting my efforts as a process intern.

Many thanks are also owed to Rob Kraynik, Jan Maneti, John Bonzo, Rick Wurzer, and Craig Arnold at RIT for their continued advice on all aspects of fixturing, tooling, precision machining, etc. No doubt, I will continue to bust endmills and snap drills, but I understand key concepts in machining now more than ever. I also owe thanks to the machine shop and club team students that provided hours of laughter and entertainment as we learned CNC machining: Zeb Blank, Ethan George, Frankie Aiello, and Ethan Patane.

I also owe a thank you to important colleagues and friends. Dr. Andrew Greeley has offered countless musings about our shared research and responsibility in keeping hybrid manufacturing available at RIT. (Soon to be Dr.) Petra Cazzanelli has provided years of support and commiseration throughout the research process. Taza Razvi has been a major influence on my work ethic, especially in this last semester. My colleagues within the iMED lab have also played a crucial role in my research development: Dr. Srikanthan Ramesh, Samantha Sorondo, Emily Sarles-Lazarus, Camila Ceballos, Valeria Marin, and A. Cardinali. Thank you to all my Rochesterian friends I've gathered along the way. Also, thank you to my cycling buddies for keeping me out of the lab during the summer.

Abstract

A cast iron repair process that restores above 80% of the original tensile strength without thermal pre-conditioning is presented. Cast iron, an integral alloy to transportation and agricultural sectors, is a difficult alloy to repair owing to the presence of discrete graphite flakes and the tendency to form brittle iron-carbide phases and porosity. Preheating and post-process annealing assist in preventing premature fracturing but are economically and environmentally impractical for large castings. Thus, methods that circumvent these limitations while avoiding defect formation are crucial.

Laser-based directed energy deposition (DED) offers a highly controllable method of remanufacturing cast iron and high carbon steel components. Lower thermal input and dilution in DED contribute to less porosity and smaller thermal gradients compared to welding processes. The result is that, under a narrow range of process parameters (laser power, scanning speed, etc.), defects can be avoided. This study expands the DED processing window of cast iron and steel through ancillary processing strategies, namely, varying filler material composition, wire feeding, and melt pool vibration. Using nickel-based filler material, 82% of the cast iron ultimate tensile strength may be restored without auxiliary preheating and annealing cycles. In-situ high speed imaging complements this work by quantifying process stability under various processing conditions (laser power, scanning speed, etc.). Using low thermal input conditions, the repair strength may be maximized while reducing gas generation and escapement during melting. Wire feeding was also found to maximize process stability by reducing the amount of graphite that was vaporized or oxidized during laser exposure. A novel method of localized ultrasonic melt pool vibration was shown to refine the microstructure in deposited stainless steel 316L and promote equiaxed grain formation. The use of these technologies enhances the robustness of DED techniques, expanding the application scope and lowering the cost to entry for iron and steel repair. As society aims toward technologies that reduce greenhouse gas emissions and energy consumption, this work provides a foundation for laser-based DED restoration of cast iron and dissimilar material structures.

Table of Contents

Contents

List of Figures

List of Tables

List of Relevant Acronyms

AM – Additive Manufacturing

BCC – Body-centered cubic

CGI – Compacted graphite iron

CMOS – Complementary metal-oxide semiconductor

CNC – Computer numerical control

CT – Computed tomography

DC – Direct current

DED – Directed energy deposition

EDS – Energy-dispersive x-ray spectroscopy

FCC – Face-centered cubic

FET – Field effect transistor

FZ – Fusion zone

GCI – Gray cast iron

GTAW – Gas-tungsten arc welding

HAZ – Heat affected zone

HVOF – High-velocity oxygen fuel [welding]

IN625 – Inconel 625

NDE – Non-destructive evaluation

PMZ – Partially melted zone

SEM – Scanning electron microscope

SS316L – Stainless steel 316L

TIG – Tungsten inert gas [welding]

WAAM – Wire-arc additive manufacturing

Chapter 1 - Introduction

1.1 Introduction

Remanufacturing and repair industries are gaining traction as viable methods to reduce industrial energy use, emissions, and cost. In 2019, direct industrial emissions and indirect energy-generating emissions in all manufacturing facilities accounted for 29.7% of the total U.S. greenhouse gas emissions [1]. Of the emissions native to iron and steel production processes, coke production for producing iron from raw ore accounts for most CO_2 emissions [1]. In part to technological improvements and reliance on steel recycling, the iron and steel production sector reduced CO_2 emissions by 60% between 1990 and 2019 [1]. Utilization of repair and remanufacturing technologies further reduces greenhouse gas emissions as well as reducing the energy and costs of producing new components via traditional subtractive and formative manufacturing processes [2]–[5]. To harness these benefits, design for remanufacturing must be incorporated into product lifecycles [5]. Technology development for remanufacturing serves to widen the range of applications and reduce the barrier to adoption [4].

Additive manufacturing (AM) technologies have garnered considerable attention within sustainable repair and remanufacturing applications. Directed energy deposition (DED) is one AM technique that, due to its localized nature, is widely considered ideal for repair. Like welding, DED couples an energy source (electron beam, laser, or plasma arc) with material delivery (blown-powder or fed-wire) at a single location to build up material as seen in Figure 1. The choice of energy source and material delivery method dictate the process cost, deposition rate, and print resolution. DED generally provides lower thermal input, dilution, and distortion compared to tungsten inert gas (TIG) welding and high velocity oxygen fuel coatings (HVOF) [6]–[8]. DED also provides a high level of control, allowing for tuning of parameters such as laser power, scanning speed, scanning pattern, deposition rate, etc. Several parameters are also dependent on one another. Stepover and layer height, for example, are nominal values that are chosen based on the track geometry dictated by laser power, scanning speed, etc. The thermal conditions promoted in DED are highly dependent on the process parameters, and the material properties of deposits are subsequently dependent on these thermal conditions [9], [10]. Finding

process parameter combinations that provides high strength, full density, and minimal distortion remains a foundation in DED literature [11]–[17].

Repair and remanufacturing applications of DED suffer from these challenges and more. The high process cost limits the utility to high-value components such as tooling or large castings. Residual stresses from non-equilibrium solidification threaten the integrity of interfacial bonding between the repair core and the deposited material, especially in the case of a bimetallic interface [18]–[20]. Tensile residual stresses formed from rapid solidification in DED also degrade the fatigue life of components [21], [22]. Additionally, the stress-driven geometric distortion in DED threatens the geometrical accuracy of repaired components [23]–[25]. Gas pockets and pores are also a known problem in cast iron repair. The discrete carbon flakes or nodules form carbon monoxide and carbon dioxide gases when heated above 1000°C [26]. Knowing that gray cast iron holds a liquidus temperature near 1280°C, it is expected that gaseous CO and CO_2 may be trapped in the rapidly solidifying melt pool. In components exposed to gas or oil during service, the volatility of residual hydrocarbons contributes to additional porosity in the solidified material as the hydrocarbons decompose during laser exposure [27]. Repairing medium- and high-carbon steels also presents challenges in DED. The rapid solidification at the interface "quenches" the partially melted zone (PMZ), creating microstructures such as martensite and ledeburite which are brittle and prone to hot cracking [28]–[32]. The key to mitigating many of these issues lies in low spatial and temporal thermal gradients, two major challenges to the highly transient and localized DED process. The consequences of improper thermal conditions are significantly reduced mechanical strength and fatigue life at the interface of the deposited repair and the substrate core [18], [31].

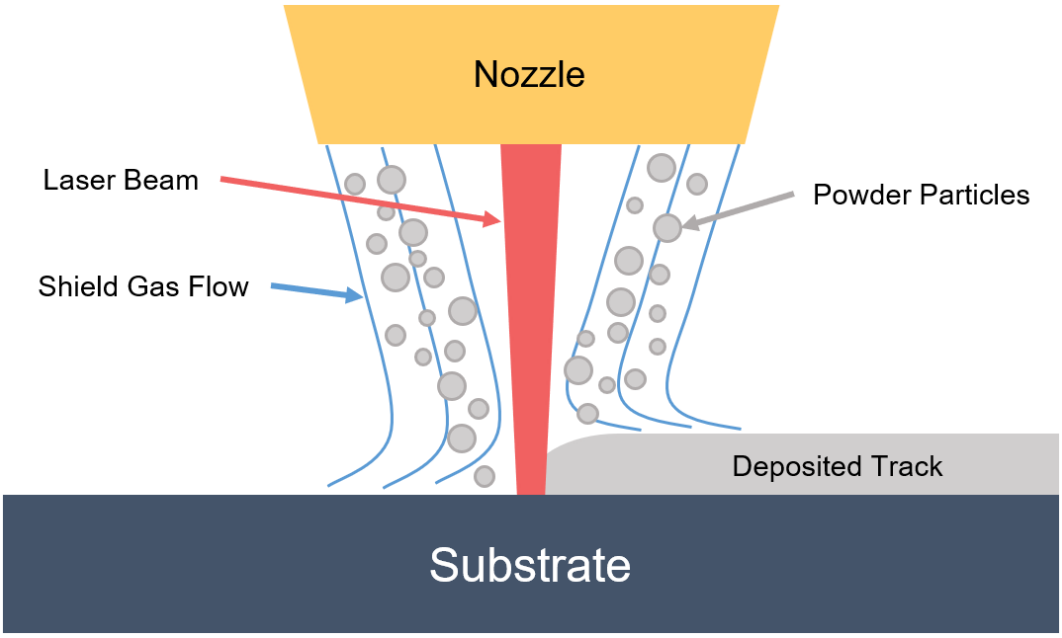

Figure 1. Generalized depiction of a blown-powder laser DED system.

In the context of repair of steels and cast iron, considerable attention has been given to optimizing deposition-specific process parameters for powder-based DED [19], [20], [31], [33]. Laser power, scanning speed, and material feeding rate are commonly studied as independent factors affecting the dimensions and mechanical behavior of deposited materials. Factors that promote higher temperatures, i.e., higher laser power and slower scanning speed, create sufficient dilution but suffer from increased trapped gas porosity. Additional works have studied the effects of different scanning strategies on residual stresses, distortion, and geometrical accuracy [15], [23], [34]–[41]. Nevertheless, few works have explored unique process conditions to enhance repair quality. Traditional nickel-based filler materials in cast iron welding have transitioned to cast iron DED repair; however, the structural outcomes between low-cost stainless steel and high-cost nickel-based superalloys has not been established. Furthermore, parameter considerations for differing modes of material deposition are also under-reported, especially in depositions on high-carbon iron alloys. Wire-based DED processes offer lower resolution compared to blown-powder systems; however, wire is considerably less expensive compared to atomized powder making it more cost effective for cast component repair. Lastly, little consensus has been reached on the metallurgical effect of melt pool vibration in DED. Methods of melt pool agitation may be effective for

improving metallurgical quality in large component repair; however, few works have developed part-agnostic vibration strategies [42], [43].

The proposed study aims to further the fundamental understanding of powder- and wire-based DED processes for the repair of cast iron and carbon steel alloys. To justify the process cost, the development will aim toward iron alloy repair in absence of preheating, a significant limitation in repairing large components. The effect of ancillary process modes on the strength of steel alloys repaired via DED will be studied.

1.2 Research Objectives

The goal of the proposed study is to understand the fundamental mechanics of DED processing to improve outcomes of DED-based repair by employing novel processing techniques, quantifying the resulting mechanical characteristics (porosity, dilution, interfacial strength, etc.), and explaining the mechanism that led to the achievement of such outcomes. The goal will be fulfilled by achieving the following objectives:

1.2.1 Specific Objective 1

Unveil the impact of feedstock composition and quantify the porosity and strength characteristics of the bimetallic interface in gray cast iron repairs.

1.2.2 Specific Objective 2

Quantify the process and metallurgical deviations between powder- and wire-fed laser DED repair of low-carbon steel using geometrically normalized deposition conditions and high-speed melt pool imaging.

1.2.3 Specific Objective 3

Develop localized melt pool vibration to homogenize the microstructure and reduce porosity in repaired structures.

1.3 Organization

The following section will discuss relevant background literature for achieving the above objectives. Following this discussion, Chapters 3, 4, and 5 provide complete manuscripts in preparation as peer-reviewed journal articles. Two peer-reviewed journal articles are provided in Appendices A and B as foundational literature to support these chapters. Chapter 6 will further discuss the relevant findings and the implications on short-term and long-term research objectives.

Chapter 2 - Literature Review

2.1 Cast Iron

Cast iron alloys are incredibly important to global infrastructure, finding utility in transportation, manufacturing, agricultural, energy, construction, and more, and for justifiable reasons. The low cost allotropes of iron and carbon offer excellent strength, manufacturability, thermal conductivity, vibration damping, and wear resistance [44]. Cast iron also offers incredible versatility, allowing for mechanical behavior to be tailored for specific applications (Table 1). Gray cast iron retains excellent thermal control and vibration damping, making it ideal for brakes and other rotating components. Compacted graphite iron (CGI), considered a successor to ductile and gray irons, has high tensile strength and toughness, making it ideal for engine components ranging from passenger vehicles to large (>10 ton) industrial engines [45]. High-alloy cast irons are designed with varying major constituent elements such as Ni, Mo, and Cr to obtain specific material properties [46]. Because the carbon remains in solution during solidification, high-alloy white irons are important for hardfacing and grinding applications where the incredible hardness of carbide structures is required. Considering its availability, excellent properties, and ease of use, it is no surprise that cast iron has been steadily employed for over 5,000 years* [47].

Common Grades of Cast Iron

Grade	Graphite Form	Advantages	Applications
Gray cast iron	Lamellar flakes	Wear resistance, damping	Brake drums, discs; clutch plates; pressure vessels, housings, valves, fittings [48]
Ductile cast iron	Spheroidal nodes	High strength, ductility	Engine components; turbochargers; pumps; valves; hydraulics; wind turbine mechanics [49]
Compacted graphite iron	Rounded flakes	High strength, thermal conductivity	Engine cylinders and heads; exhaust manifolds [45]
White cast iron	Fe_3C formation	Strength at elevated temps, wear resistance	Dry friction components; brake shoes; rollers [50]
Malleable iron	Aggregates	Ductility and toughness	Pistons; transmission gears; flanges; compressor components; universal joint yokes [51]
High-alloy irons	Varying	High hardness, corrosion and wear resistant	Grinding and crushing applications; impellers; mixing apparatuses [46]

Table 1. Common cast iron allotropes and their respective applications.

* There is debate on the first use of iron castings, stemming from 6,000 B.C.E. in Mesopotamia to 3,000 B.C.E. in Anatolia. Ancient cultures developing forgings of iron and copper often connected metals to the sky and heavens, even suggesting the metallurgist was of divine origin [47].

Cast iron is commonly defined as an Fe alloy with major alloying elements of C and Si that solidifies as a eutectic structure [44]. The high solubility of C in Fe results in three major structures, a) Fe and graphite or b) Fe and Fe_3C or c) Fe, Fe_3C, and graphite. The formation potential of each allotrope or *graphitization potential* is dependent on both the cooling rate and constituent elements. Higher cooling rates, such as those in welding, encourage a reduction in graphite size and increase the chilling tendency, or the formation of brittle martensitic and ledeburitic phases [44]. The chilling tendency, while ideal for high hardness applications, decreases the strength of the solidified alloy. Inoculant elements such as Al or Ca may also be included during melting to increase the graphitization potential and reduce the chilling tendency.

2.2 Repair Technologies

Repair and remanufacturing applications have found success using a variety of fusion-based processes. TIG welding, for example, is a popular method of material repair as it can achieve high resolution and high-quality results [52]. Residual stresses and distortion caused by the high heat input present significant challenges to the process. Low deposition rates and the potential of tungsten inclusions in the weld are also limitations [53]. Plasma transferred arc welding and electron beam welding were developed to mitigate these issues, but the high process cost and complexity has limited their application scope [52], [53]. HVOF coatings provide very little porosity in deposited repairs but show low dimensional accuracy and require extensive secondary machining operations [52]. There are few processes that adequately meet the requirements of dimensional accuracy, high strength, and low process cost and complexity.

One challenge of repairs is providing enough heat input for fusion while preventing the excessive heat input that contributes to residual stresses, distortion, high dilution, and porosity. The heat input is often studied post-mortem by quantifying the size of the partially melted zone (PMZ) and the heat affected zone (HAZ), shown in Figure 2. As the heat input into a repair increases, the size of these zones and melt track depth increase [53]. Dilution ratio (η) is one weld-depth metric commonly used in repair

literature and is defined in terms of the total melt track volume (V_m) and the melt track volume beneath the surface of the substrate (V_d) [54]:

$$\eta = V_d/V_m \tag{2.1}$$

In practice, linear depth or area are used in place of volumes. Chemical composition gradients have also been used to quantify dilution [20]. High dilution is undesirable, especially in carbon steels, as the increased carbon content at deeper fusion roots promotes solidification cracking and brittle martensite formation.

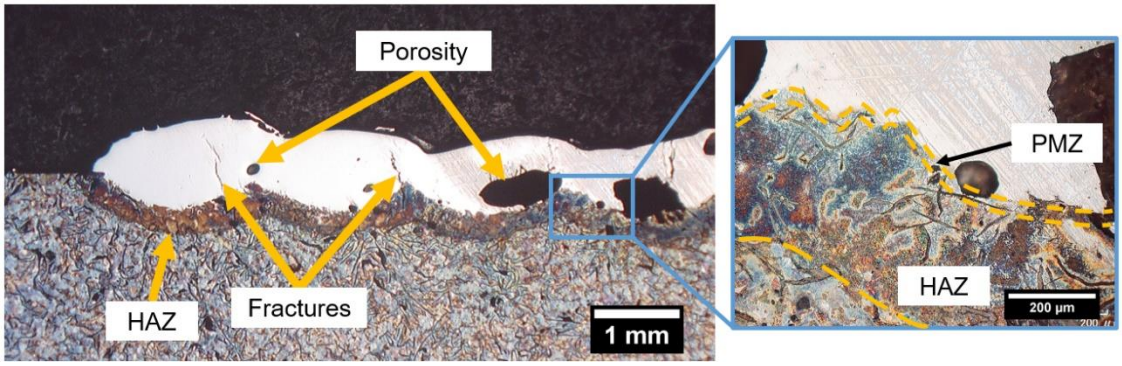

Figure 2. A stainless steel DED coating deposited on gray cast iron.

2.3 Directed Energy Deposition

Directed energy deposition (DED) is constituted as wire or powder delivered directly to the focal location of a high-intensity energy source such as a laser, electron beam, or plasma arc. Selective material deposition is performed until a component is built. Because the process is localized, DED is well suited for multi-material and functionally graded parts as well as large components that would be impractical to fit within a powder bed fusion chamber [55], [56]. DED also offers a high level of control, granting numerous parameters (laser power, scanning speed, toolpath, etc.) to achieve optimal metallurgical outcomes [52]. DED is not without limitations, however. The rapid heating and cooling created by localized energy sources create non-uniform thermal fields that promote residual stresses and distortion [9], [56]. Grain anisotropy during processing contributes to inconsistent strength in different loading directions [13], [57]. Porosity in generated structures is promoted by insufficient or excessive heat input, evaporation of volatile elements, or process-generated gas unable to escape the melt pool [9]. Finding adequate thermal conditions to minimize porosity and residual stress while maximizing the material

strength is a significant challenge in metal AM development and is often exacerbated by the open-source nature of DED platforms [55], [56].

In the context of repair, DED performs as a lower heat input option compared to traditional methods. In a comparative study of DED and shielded metal arc welding, Yu et al. showed that DED produced a HAZ 21 times smaller than the welding process [58]. The process complexity outlined above remains critical in repair contexts. Current trends in repair literature seek to unveil 1) the quality of the repair compared to conventionally processed parts, 2) the integrity of the HAZ, and 3) mechanical performance of bimetallic material systems. The following section will elaborate on these trends.

2.4 Deposition-specific Parameters

Of the tunable parameters in DED, deposition-specific parameters (laser power, scanning speed, material feeding rate, etc.) are amongst the most popular to study. As mentioned previously, the thermal conditions inherent to the process are highly dependent on the energy and material sources [9], [10]. As the melt pool temperature changes, the morphology of the melt pool and solidified track change. Ocelík et al. studied combinations of laser power and linear mass deposition rate to show the geometrical variance, microhardness, and microstructure of a Co-based alloy deposited on gray cast iron [19]. The authors suggested porosity may be minimized by maintaining dilution between 5-15%, producing a cladding contact angle of at least 100°, and minimizing shielding gas usage. Arias-González et al. performed a similar study of NiCrBSi alloy deposited on ductile and gray cast iron [20]. Samples with higher dilution generally showed higher trapped gas porosity in deposited tracks. Interfacial porosity in FeNiCr alloy cladded on nodular cast iron notably decreased the tensile strength in a study conducted by Li et al. [33]. The parameter-driven thermal gradients affect porosity generation in DED. In these studies, porosity was generated in both single-track, multi-track, and multi-layer structures. Although lack-of-fusion and keyhole porosity are potential sources, cladding on carbon steel substrates has the potential to generate CO and CO_2 gases which can be trapped in the solidifying melt pool [53], [59]. Tong et al. observed that

slower scanning speeds when cladding Cr onto gray cast iron lengthened the molten duration of the melt pool and reduced the amount of trapped gas in the solidified track [60].

Because of the high carbon content and rapid cooling, brittle metastable phases such as martensite and ledeburite may form in the cladding process. Li et al. investigated crack propensity from varying power input while depositing Ni-Cu on nodular cast iron [28]. Excessive power produced "chilled" ledeburite structures surrounding graphite nodules. The nodules acted as fracture initiation points for the brittle ledeburite under stress. Residual stresses and distortion are also functions of the heat input; however, little work has been conducted to quantify the stresses generated in repaired structures. The author's recent work in quantifying these stresses is outlined in Section 7.

2.5 Filler Material Composition

Several of the challenges in cast iron repair are directly linked to graphite within the melt pool. When a Fe-C alloy undergoes rapid solidification, C atoms have insufficient time to segregate out of solution to form homogeneous carbon flakes or nodules. Instead, chilled metastable formations of iron carbides, Fe-C, form. These hypereutectic intermetallic phases are naturally brittle and often fracture under thermally driven solidification stresses. Because of this, filler materials that react favorably with carbon are preferable.

Filler/Deposition Material	**References**
Ni or Ni-base alloys	[27], [28], [61]–[64]
Cr or Cr-base alloys	[60], [65]
Fe-base alloys	[29], [33], [58], [63], [66]–[68]
Co-base alloys	[69]
Mo	[65]

Table 2. List of studies with various materials deposited on cast iron through laser-based DED or laser surface alloying.

Fe-base alloys are a common choice for filler materials cast iron repair, owing to the similarity in major constituents. Fe alloys are also relatively inexpensive compared to preferable Ni alloys. Issues arise

near the high-carbon boundary between the cast iron and the Fe-based cladding material. This scenario, described above, generates Fe-C phases at this boundary and around partially dissolved graphite particles [29], [33], [63]. Martensite formation is commonly observed as a matrix phase at the cast iron interface with scattered graphite particles and hypereutectic ledeburite shells [29], [33]. A schematic of the graphite particle evolution is shown in Figure 3. As graphite particles dissolve, carbon saturates the iron-rich melt pool and forms martensite, the white region under the melt pool, upon solidification. These intermetallic phases offer incredible strength but little ductility. Shrinkage stresses during solidification can induce premature cracking, even in instances where preheating has effectively lowered the thermal gradient [63], [68]. Intermetallic phases can also be found throughout the deposited material, with interdendritic carbides forming around austenite dendrites [68].

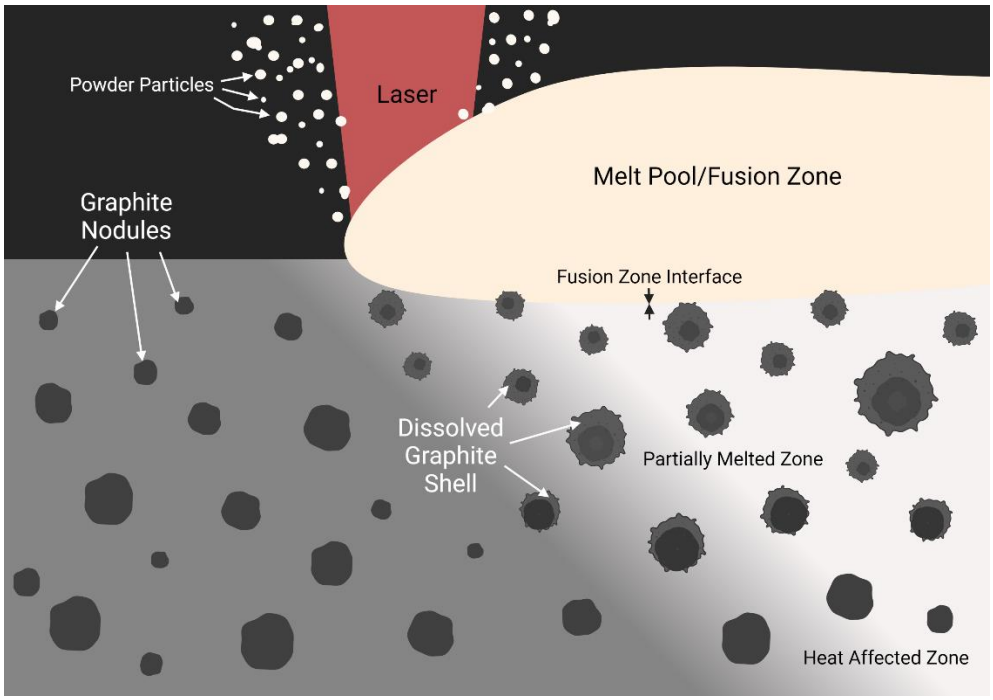

Figure 3. Illustration of graphite nodule evolution during laser DED. Note: the depth of the partially melted zone and heat affected zone are exaggerated for clarity. Illustrated using BioRender.

A Co alloy was also studied in a seminal study by Ocelík et al. [69]. The in-depth analysis provided several guidelines for reducing porosity in laser cladding on gray cast iron. The chosen alloy, a mixture of Co, 28% Cr, 4.5% W, and 1% of Si and C, offered similar behavior than comparable studies with Fe-Ni-Cr alloys. Dendrites of γ-Co formed at the interface region, surrounded by eutectic γ-Co and

W- and Cr-carbide phases. Intermetallic phases were also found in the partially melted zone (PMZ) in the gray cast iron. Melting and re-solidification of the carbon-saturated iron melt produced martensitic phases which remained after solidification and formed cracks after cooling. Under optimal process parameters, the authors were able to eliminate cracking and pores in coatings up to 3 mm.

Ni and Ni-base alloys are often viewed as the optimal filler material choice for cast iron repair. The justification for this opinion stems from several elemental advantages [70], [71]:

1. Ni has a relatively low carbon solubility limit of 0.5% at the eutectic temperature. This behavior results in precipitation of carbon as graphite within the fusion zone (FZ).
2. The density of graphite is considerably lower than Ni. During solidification, the precipitation as graphite increases the volume of the fusion zone, reducing the shrinkage stresses during cooling.
3. The suppression of intermetallic phases and high ductility of Ni-based alloys are ideal for resisting the tensile stresses exerted during cooling.

Like the materials discussed above, complex atomic interactions occur when dissolving carbon in a molten pool of Ni. The microstructure of Ni-cladded cast iron depends on the other constituent alloying elements, although these are typically a combination of Fe and Cr. When subjected to rapid solidification, a dendritic Ni matrix phase may form with Fe-Cr laminar eutectics forming as precipitates [64]. Concentration of Cr near the cast iron interface has also been noted [64], likely due to the preferential formation of metallic carbides with early groups of transition metals (Sc, Ti, W, Cr) over later transition metal groups (Fe, Co, Ni) [72]. This affinity is based in the atomic radius ratio between carbon and metal atoms according to Hägg's rule [73]. Atomic systems with a ratio between 0.41 and 0.59 have interstitial sites where carbon may reside. If this ratio exceeds 0.59 as in late transition metals, carbon atoms require phases with large unit cells that have larger interstitial sites for carbon atoms to reside [72].

Early studies of Ni-based alloy cladding noted an absence of fracturing immediately after repair with cracks forming over time [64]. Later studies confirmed this behavior, noting that the thermal gradients in cladding without preheating formed cracking in deposited Ni alloys [63]. Lestan et al. found

that Ni-base alloy with 17% Cr and 4% Fe was a resilient alloy and resisted fracturing due to high thermal gradients in repair of cast iron [63]. Li et al. found that a hybrid filler approach of NiCu alloy as a buffer layer and low-expansion Fe-36Ni alloy suppressed major cracking [62]. In most cases, introduction of preheating and slow cooling is required to obtain the graphite precipitation and low-stress FZ that avoids interfacial cracking [70].

2.6 Powder-based vs. Wire-based DED

Because of the process flexibility, the material deposition methods vary between DED processes. Currently, principal feedstock materials are in powder or wire form. Wire-fed DED offers several advantages compared to powder-fed DED:

- *Material efficiency*: Wire DED processes can exhibit up to 100% material usage [74], whereas powder DED may only capture 40-80% of powder [75]. The material usage efficiency is also less parameter-dependent in wire DED [76]. Considering the high-cost and energy usage to generate flowable powder [77], high material usage offers economic and environmental incentives.
- *Deposition rate*: Wire-based DED offers considerably higher deposition rates. Taminger & Hafley reported deposition rates up to 330 g/min with electron-beam wire deposition [78]. Powder-fed DED operates near 10 g/min [74].
- *Safety*: Metal powder offers critical safety challenges [79]. The high surface area to volume ratio encourages oxidation which may produce dangerous fumes and even combustion. Inhalation of fine powder is also problematic, and respiratory personal protective equipment is needed when handling metal powder.

Several studies have offered direct comparisons between feeding modes. Syed et al. observed few differences between the metallurgical quality of powder- and wire-fed DED; however, inter-dendritic porosity was found in powder-based DED samples [76]. In both modes, lack-of-fusion porosity between adjacent tracks were observed, indicating the criticality of process optimization. Borges et al. studied stainless steel depositions and concluded that, while powder generated more porosity, wire fed deposits

were more sensitive to position and feed rate [80]. Heigel et al. compared Inconel 625 wire- and powder-fed depositions [81]. The authors found that powder produced higher melt-pool temperatures at equivalent parameters owing to the higher laser absorption efficiency from particles in-flight. The increased laser absorption contributed to higher dilution as well, a conclusion confirmed by Abioye et al. [82]. Heigel et al. further suggested that powder feeding is the superior feeding mode owing to lower thermal distortion. Blinn et al. also concluded that powder-fed depositions of 316L were superior, offering fewer nonmetallic inclusions and improved fatigue life [83].

It is well established that powder-based processes are inherently more expensive compared to wire-based processes, largely due to the high cost of the flowable gas-atomized powder and powder handling equipment. Despite this, limitations in distortion and process sensitivity pose significant challenges to wire-fed DED. The continuity of material fed into the melt pool dictates crucially different process behavior in wire-based DED, and this has not been well reported in literature. Currently, the majority of carbon steel AM repair literature has focused on laser-based, powder-fed processes [19], [20], [27], [84]. A significant gap exists in the reporting of the quality of castings remanufactured through wire-fed DED processing modes.

2.7 Vibration-assisted DED

Several instances of DED systems have been equipped with subsystems to introduce mechanical vibrations to the rapidly solidifying melt pool. There are several advantages to adding vibration to the melt pool and have been described similarly over a range of frequencies (50 Hz – 41 kHz). The minute displacements caused by mechanical waves induce acoustic streaming and cavitation in the liquid around growing dendrites [85]–[87]. The mixing caused by this phenomenon creates bending stresses that are sufficient to fracture and redistribute the crystals throughout the melt pool. These fragments encourage nucleation in the liquid metal, thus reducing grain size. Todaro et al. offered another explanation for the grain refinement in their study of ultrasonic part vibration during deposition of stainless steel 316L [88]. Ultrasound effectively lowered the temperature gradient by 50% at the solid-liquid interface. This

reduction encouraged enough constitutional supercooling to encourage grain refinement. Constitutional supercooling occurs when the liquid temperature ahead of the solidification front falls below the freezing temperature of the liquid due to compositional changes [89]. At these temperatures, nucleation begins spontaneously in the liquid, refining the grain structure further. Reduced porosity using vibration strategies has also been attributed to the increased melt flow from minute displacements, although the fundamentals for porosity escapement from vibration have yet to be established [85], [90].

Creating cavitation within the melt pool has primarily relied on streaming acoustic waves from transducers through the build platform [91]–[94]. Other systems have relied on oscillatory mechanical movements through the machine kinematics (X, Y, Z axes) for creation of melt pool motion [95]. The frequencies and amplitudes for motion have varied. Tsujino et al. reported optimal weld strengths in aluminum plates at 27 kHz and 40 kHz operating between 2-7 μm displacement [92]. Chen et al. found grain refinement in wire-arc deposited Cu-8Al-2Ni-2Fe-2Mn alloy at 20 kHz [93]. Ma et al. reported a significant increase in tensile strength in cold-metal-transfer arc welding of Inconel 625 onto a 28 kHz vibrating substrate [94]. This is owing to the grain refinement strengthening dictated by the Hall-Petch relationship:

$$\sigma_{HP} = k/\sqrt{d} \tag{1.1}$$

This defines the grain boundary strengthening (σ_{HP}) in terms of a material-specific Hall-Petch coefficient (k) and the average grain size (d) [96]. The inverse relationship between strengthening and grain size dictates methods of grain refinement will result in strengthening, down to a limit of <10 nm grain size [97].

Cong & Ning noted that ultrasonic vibration of the part during powder-based DED of stainless steel reduced gas-induced porosity and cracking and increased the dilution into the substrate [85]. The grain refinement caused by vibration also improved mechanical performance of the deposited material. Li et al. also noted a decrease in grain size using low frequency (500-1400 Hz) part vibration during TiC/AlSi10Mg powder DED [98]. The authors found an optimal vibration near 1000 Hz and 10 μm

amplitude to draw out gas porosity while not incurring additional porosity from excessive melt pool cavitation. Zhang et al. also found that vibration around 36 Hz reduced porosity from 6.66% to 1.52% in Al-Mg wire-arc additive manufacturing (WAAM) [90]. Chen et al. were able to achieve nearly isotropic material properties in a Cu-Al alloy deposited by WAAM using part vibration (20 kHz) [93]. The authors concluded that the grain refinement, twinning and dislocation formation, and precipitation strengthening were all driving factors for the strength behavior.

On a fundamental level, the use of in-situ vibration increases the range of acceptable process parameters by reducing defects from imperfect process conditions. However, a need exists to form part-agnostic vibration strategies. Additive manufacturing requires mass and volume changes throughout the process which make the vibration kinetics and the subsequent melt pool agitation inconsistent throughout the process [86]. The requisite energy to induce vibration scales with the transmission media size, making part-level vibration also impractical for large components [86]. Yuan et al. recently developed a method of localized ultrasonic melt pool vibration [86]. An ultrasonic probe contacts the deposited surface at a constant 20 mm offset distance to induce consistent mechanical waves at the melt pool. Although the authors showed a decrease in Ti-6Al-4V and stainless steel 316L grain sizes using this technique, columnar grains remained in the Ti-6Al-4V sample [86], [99]. The authors noted that the ultrasonic intensity was lower than the required intensity to induce melt pool cavitation approximately one-third of the time. This is in part to the attenuation caused by having the probe offset from the melt pool. Reducing the offset distance or increasing the vibration amplitude were offered by the authors as improvements. There are also geometrical limits to this methodology. For one, the deposition surface must be longer than the 20 mm offset distance to provide ultrasonic vibration, effectively lowering the resolution of the print process. Secondly, the morphology of the transmission media will affect the effective vibration. The agitation observed at the melt pool will be different when depositing on a thin wall vs. a surface, for example. Methods that circumvent the geometrical and energy limitations of current ultrasonic vibration assistance platforms are needed for creating robust fusion-based processes that have high-strength and uniform material properties.

Chapter 3 – Laser-based Directed Energy Deposition Remanufacturing of Gray Cast Iron using Stainless Steel 316L and Inconel 625 Filler Materials[†]

Jakob D. Hamilton[a], David Trauernicht[b], Denis Cormier[a,b], Iris V. Rivero[a]

[a] Department of Industrial and Systems Engineering, Rochester Institute of Technology, One Lomb Memorial Drive, Rochester, NY 14623
[b] AMPrint Center, Rochester Institute of Technology, One Lomb Memorial Drive, Rochester, NY, 14623

Corresponding Author: Iris V. Rivero, iris.rivero@rit.edu, One Lomb Memorial Drive, Rochester Institute of Technology, Rochester, NY 14623

Highlights

- Stainless steel 316L and Inconel 625 were used to restore gray cast iron properties using laser directed energy deposition.
- Laser-powder and laser-wire repaired structures show differing microstructural characteristics.
- With and without in-process thermal cycles, the cast iron tensile strength was restored up to 98.7% and 85.9%, respectively.

Keywords: additive manufacturing, remanufacturing, directed energy deposition, gray cast iron

Abstract

Directed energy deposition has been identified as an ideal candidate for restoring damaged or worn cast iron components such as agricultural engine blocks, housings, and manifolds. While this laser-based process offers superior control of the heat input compared to traditional arc-based repair, gaseous porosity and brittle intermetallic structures reduce the strength and ductility of the fusion zone. Varying combinations of Fe-Ni-Cr alloys have found success in remanufacturing cast iron using laser-based DED, but little attention has been given to the consequence of filler material composition and form, i.e., wire vs. powder. This study quantifies structural characteristics in cast iron repairs and offers microstructural and process-specific insights to support these observations. With appropriate thermal conditions, up to 98.7%

[†] This chapter is in preparation for submission to Acta Materialia.

of the original tensile strength of gray cast iron may be achieved. These results point towards superior gray cast iron restoration using tunable laser-based DED.

1. Introduction

Aftermarket remanufacturing is a burgeoning portion of industry for several reasons [52], [84], [100]. First, rebuilding worn material is a cost effective alternative to replacement for components that are no longer in production or are not widely available like in supply chain shortages. The capital cost and development time for tooling in casting and forging are rarely justified for small-batch replacement operations. Also important to consider are the sustainability ramifications of remanufacturing. It takes considerably less energy for building-up material on an existing core via welding or thermal spray than to recast and machine the same component. This furthers the cost savings within the aftermarket repair sector.

While remanufacturing has typically relied on arc-based welding processes for restoring worn or defected material volume, the high thermal input with welding can create significant defects in the heat affected zone. Solidification cracking is common and is exacerbated in cases where the base and filler materials have differing thermal expansion coefficients. Any process instability or material incompatibilities may also result in porosity, which significantly reduces the fatigue life in components. Low heat input technologies like thermal spray or cold spray avoid these issues but require additional post process machining due to the low resolution of material deposition.

In these cases, laser-based directed energy deposition (DED) finds utility owing to its tunable thermal input and fine (<3mm) resolution. Laser power, scanning speed, and material feeding rate can all be adjusted to optimize dilution and adhesion [101]. The tunable aspect has offered significant technological development in cast iron remanufacturing, where the high carbon composition and rapid melting and solidification often create brittle microstructures and microporosity in the fusion zone. In addition to defect remediation through process parameter control, varying combinations of Fe-Ni-Cr alloys have been studied. Fernández et al. showed that NiCrBSi cladding on gray cast iron formed hard Cr

precipitates within dendritic Ni structures [102]. Despite slow cooling of the part, residual stresses formed fractures in the brittle fusion zone over a period of 4 months. Lestan et al. coated varying grades of cast iron using Ni-17Cr-4Fe powder [103]. Fractures were noted in nearly all samples due to the formation of interfacial martensite and thermal stresses. Weng et al. performed laser cladding of Fe-15Cr-4Ni powder on ductile cast iron and observed similar behavior at the interface [67]. Martensite and ledeburite in the partially melted zone fractured under residual stresses estimated to be 1688 MPa. Li et al. identified the formation mechanics of martensite and "chilled" ledeburite within the partially melted zone for Fe-13.5Cr-5Ni coatings on ductile cast iron [29]. Their subsequent work using Fe-35Ni-10Cr and Ni-base alloy powders achieved partial remediation of these brittle phases [27], [33], [62]. Porosity remained a significant issue within these repairs as they served as stress concentration sites that initiated tensile fractures. Stainless steel 316L (Fe-17Cr-12Ni) was recently used to restore gray cast iron tensile strength but required significant preheating and annealing to prevent premature failure [104].

Of these studies, no consensus of Fe-Cr-Ni alloy composition for remanufacturing gray cast iron has been reached. Defining the structural effects of each composition under specific laser deposition conditions, i.e. thermal and material inputs, is difficult and time consuming. Furthermore, few studies have examined the metallurgical complexity of the diluted cast iron base material, austenitic filler materials, and the mixture of these dissimilar alloys. This study examines this complexity within the context of the unique process physics of powder- and wire-fed laser DED. Two common austenitic alloys, stainless steel 316L and Inconel 625, are studied as filler materials. The compositional and metallurgical consequences within the filler zone are quantified and connected to bulk mechanical properties.

2. Methodology

2.1 Experimental Setup

A Hybrid Manufacturing Technologies (McKinney, TX) AMBIT FLEX system retrofitted within a Hardinge GX250-5axis CNC vertical milling center was used for all experiments. Two separate tools were used: one for powder deposition (2.4 mm spot size) and one for wire deposition (2.0 mm spot size).

The powder used was gas atomized (d_{10}=49 μm, d_{50}=61 μm, d_{90}=92 μm) stainless steel 316L (SS316L). Two wires were used in experiments: SS316L welding wire (d=1.07 mm) and Inconel 625 (IN625) welding wire (d=0.76 mm). Ni-base alloys are preferable for cast iron repair due to their low carbon solubility limit but are considerably more expensive than Fe-Cr-Ni alloys such as SS316L. Gray cast iron (GCI) plates were used as substrates (ASTM A48 Class 40). The composition of these alloys is shown in Table 3.

Material	**Ag**	**C**	**Co**	**Cr**	**Cu**	**Fe**	**Mn**	**Mo**	**N**	**Nb+Ta**	**Ni**	**O**	**P**	**S**	**Si**	**Sn**	**Ti**
GCI plate	-	3.12	-	-	0.38	bal.	0.71	-	-	-	-	-	0.15	0.09	2.20	0.05	-
SS316L	-	0.01	-	17.0	<0.01	bal.	0.80	2.3	0.2	-	12.1	0.03	<0.005	0.004	0.45	-	-
IN625	<0.4	<0.1	<1.0	20-23	-	<5	<0.5	8-10		3.15-4.15	>58	-	0.01	0.01	<0.5	-	0.4

Table 3. Chemical composition (wt%) for the substrate and powder used in the experiment.

Although the head geometry varies between powder and wire additive tools, any effective differences in gas flow or laser spot size are assumed negligible. The complex fluid behaviors in laser-based DED are significantly understudied and addressing these effects on the resultant structures remains outside the scope of this research. Other head-specific parameters are presented in Table 4.

Attribute	**Powder**	**Wire**
Spot Size	2.4 mm	2.0 mm
Nozzle Gas	10 L/min	20 L/min
Shield Gas	5 L/min	-
Carrier Gas	2 L/min	-
Material delivery	Coaxial around the vertical axis	60° along vertical axis

Table 4. Fixed parameters for each material feeding mode.

2.2 Experiment

Three levels of treatment combinations were explored and compared to the properties of the original gray cast iron mechanical properties. Groove-repair samples were fabricated to compare the

interfacial strength of remanufactured cast iron (Figure 4). Optimal parameters (laser power, feed rates, and temperature control modes) were derived from quantified stability analysis using in-situ high-speed imaging and previous work [104]. The parameters used for each are shown in Table 5. A 300°C preheat and subsequent 2-hour anneal were utilized on SS316L samples to prevent solidification cracking and excessive martensite formation. Because of the high material capture efficiency in wire-based DED, only two layers were needed to fill the groove in wire-fed repairs.

	Laser Power	Laser Feed Rate	Material Feed Rate	Temperature Control Mode	No. of Layers
SS316L, Powder	750 W	650 mm/min	6.08 g/min	Preheat/Anneal	4
SS316L, Wire	1,250 W	1000 mm/min	7.19 g/min	Preheat/Anneal	2
IN625, Wire	1,500 W	500 mm/min	8.66 g/min	None	2

Table 5. Parameters used in each treatment combination.

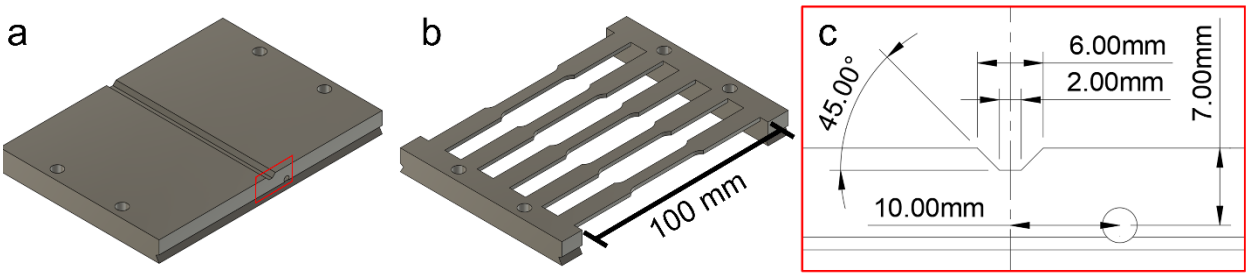

Figure 4. Drawing of the trapezoidal groove cross section and thermocouple location with dimensions.

2.3 Characterization

Microstructural characterization was performed on cross-sections of the groove repair samples. After being mounted in epoxy, samples were ground and polished and etched using a solution of nitric acid (3% vol) in ethanol (97% vol) for 10 seconds. To better view the filler material microstructure, additional etching using hydrochloric acid (98% vol) in hydrogen peroxide (2% vol) was performed after taking microstructural images. These images were taken using scanning electron microscopy (SEM). Energy-dispersive x-ray spectroscopy (EDS) was also performed to view location-dependent composition of the remanufactured structures. Vickers microhardness was measured on mounted samples using a 200

gram load following ASTM E384 standard [105]. Porosity analysis was conducted on machined tensile samples using computed tomography (CT). Pore thresholding was conducted using Volume Graphics Studio MAX (Heidelberg, Germany).

Uniaxial tensile testing was performed to gauge the bulk mechanical strength of repaired cast iron structures. Sample dimensions followed subsize tensile testing samples described in ASTM E8 [106]. Strain rate was specified at 2.0 mm/min, and crosshead displacement was used for strain measurement. A 2500 kg load cell was used to measure tensile stress.

3. Results

3.1 Microstructure and Composition

Welded samples showed heterogeneous microstructures owing to the varying compositions between base and weld alloys and the rapid solidification rate (Figure 5). The cast iron substrates maintained pearlite structures through the heat affected zone (HAZ) up to 200μm from the fusion zone (FZ) for both filler compositions. Within the partially melted zone (PMZ), resolidified cast iron appeared primarily as acicular martensite with ledeburite forming in the high carbon regions between graphite flakes and the fusion line. Ledeburite, a eutectic formation of austenite and cementite, likely formed as carbon from graphite flakes diffused into molten iron and solidified before carbon atoms could diffuse into stable structures. In addition to ledeburite, islands and peninsulas of martensite were present along the fusion line (Figure 6). This macrosegregation is a product of fluid flow due to Marangoni convection, rapid solidification, and the differences in liquidus temperature between cast iron and the austenitic filler materials. Liquidus temperatures for IN625 and SS316L are 1350°C and 1400°C-1450°C, respectively, and are considerably higher than that of gray cast iron (~1200°C). This, along with a general immiscibility between the filler and base materials, creates a condition where superheated base metal may be pulled upward into the melt pool due to Marangoni flow and quickly freeze as heterogeneous regions at the fusion line [107].

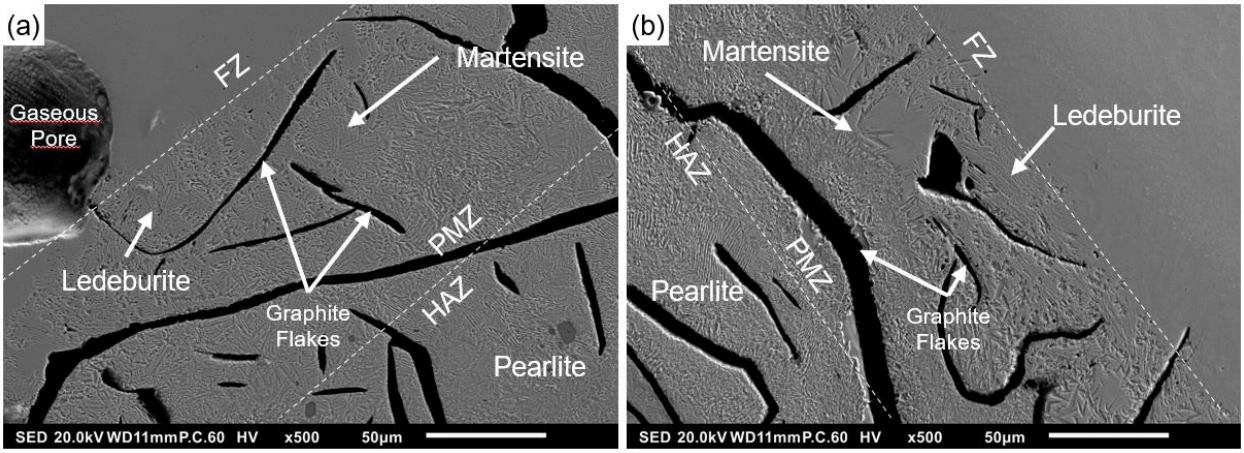

Figure 5. Examples of heterogeneous microstructures in the partially melted zone for remanufactured samples using (a) SS316L powder and (b) IN625 wire.

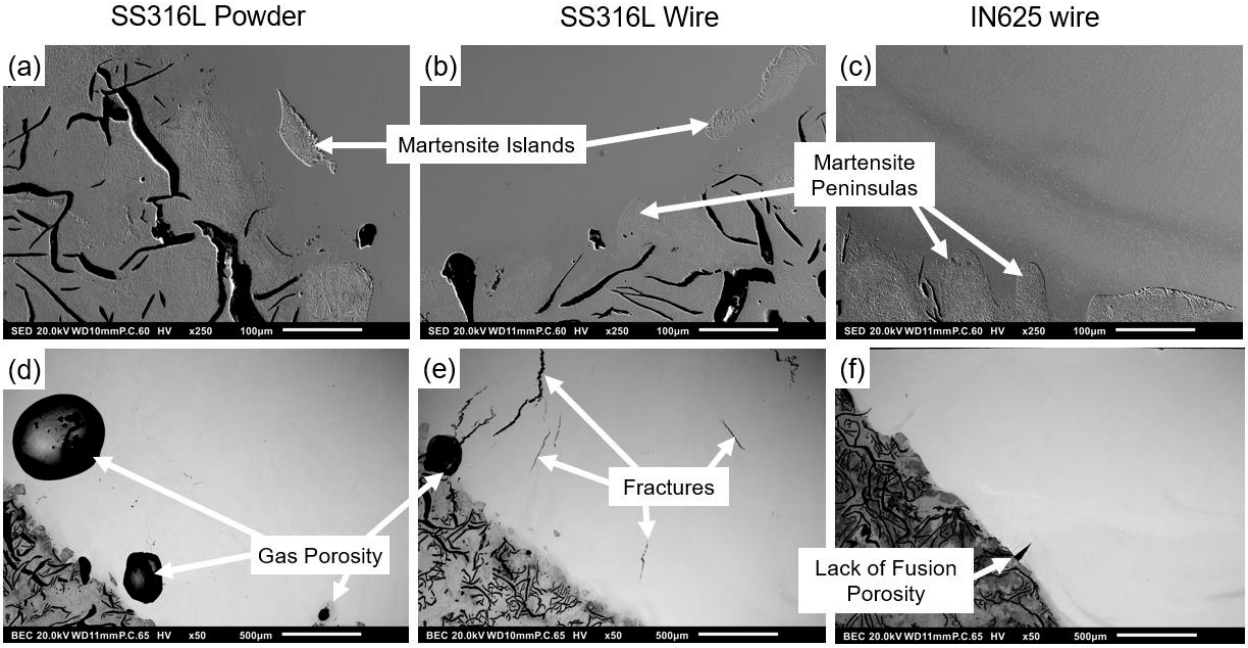

Figure 6. Macrosegregation, porosity, and fractures within the fusion zones of (a,d) SS316L powder, (b,e) SS316L wire, and (c,f) IN625 wire. Macrosegregation is visible as islands and peninsulas of resolidified cast iron.

Fusion zones also showed unique microstructures. In both SS316L samples, epitaxial growth occurred along the solidification front. Columnar dendrites grew from the solid boundary toward the center of the deposited track. Near the top of deposited tracks, grains were oriented along the travel direction and thus appeared as equiaxed grains in cross-sectioned images. Two notable differences were observed between powder and wire samples: 1) fewer pores were located along the interface in SS316L wire samples, and 2) SS316L powder samples resisted solidification cracking within the fusion zone. As

seen in Figure 6(e), large (300-800 μm) fractures appear near the top of the FZ in SS316L wire samples. Previous work has shown the sensitivity of GCI repair to incident laser energy when using SS316L alloy [104]. The higher power necessary to achieve stable melting in wire deposition causes elevated melt pool temperature. The deviation in thermal expansion between GCI and SS316L is exacerbated at higher temperature differentials, likely resulting in the solidification cracking. Although the melt pool temperature is likely higher in wire-fed repair, the melt pool retains less dilution with the GCI. The near 100% capture efficiency in wire DED creates a functionally larger melt pool, and the force of surface tension draws the height of the deposited track upward. This results in less direct laser exposure on the GCI and less graphite vaporization, one initiator for trapped gas porosity [68]. Compositionally, wire and powder samples showed only slight variation.

IN625 wire samples resisted solidification cracking in the FZ and showed epitaxial growth toward the center of the melt track. In these samples, bands of Fe formed parallel to the interface within the FZ (Figure 7). Similar to the Fe-C macrosegregation along the interface, these Fe rich bands likely resulted from Marangoni convection mixing the base and filler alloys. Higher thermal input from the elevated laser power in these samples creates larger thermal gradients that accelerate molten fluid motion. The lower energy input, i.e., low laser power and high scanning speed, in powder samples did not encourage the same level of melt pool convection. Unlike the islands and peninsulas visible in Figure 6, these bands are comprised of the cast iron base that has sufficiently mixed with the filler material in the melt pool and solidified within the melt. The microstructure in these bands depends on the elemental composition.

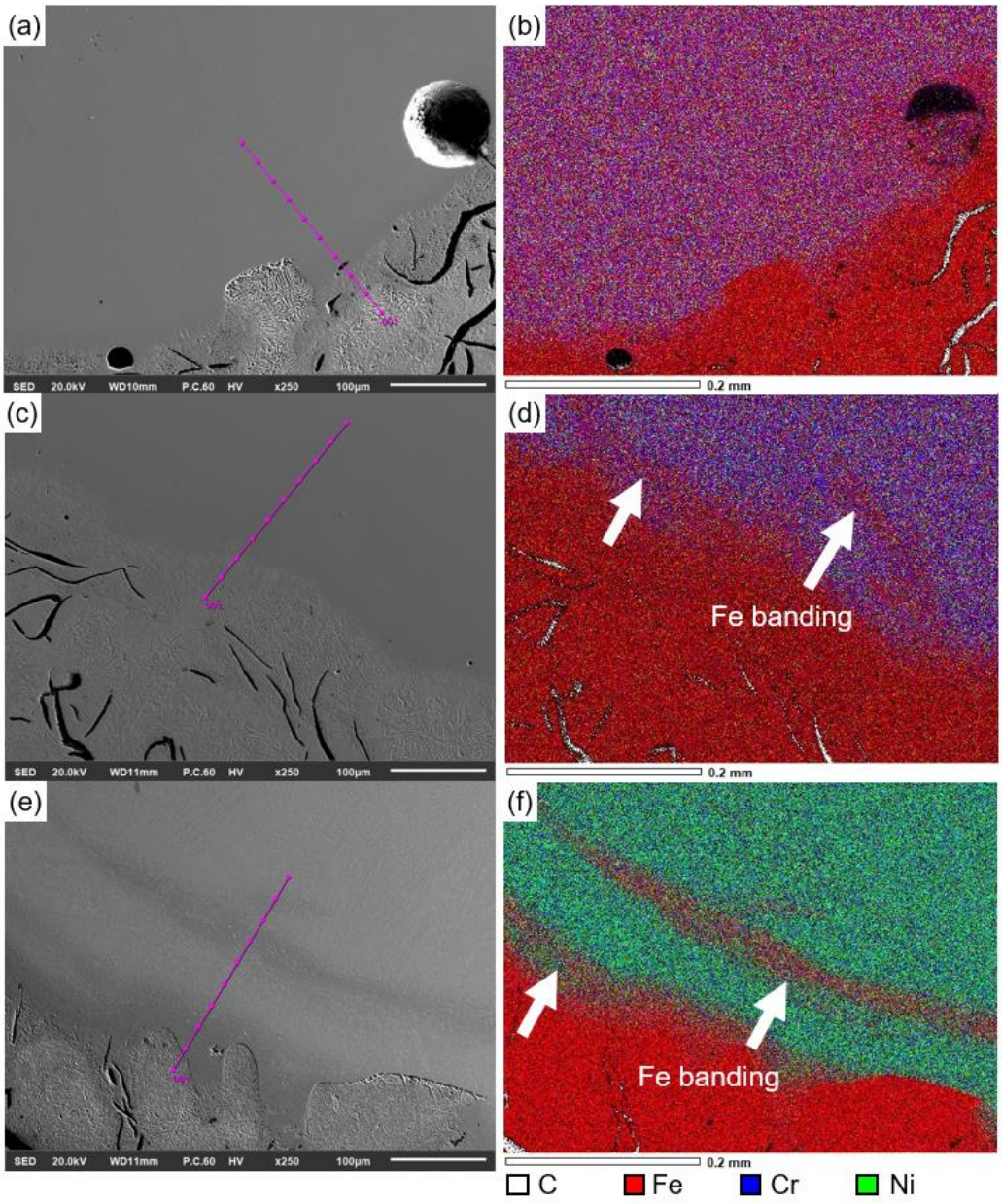

Figure 7. SEM and EDS images of the FZ and PMZ of (a, b) SS316L powder, (c, d) SS316L wire, and (e, f) IN625 wire deposits on gray cast iron.

In addition to banding near the bimetallic interface, IN625 filler promoted an Fe gradient throughout the fusion zone, visible in Figure 8. Toward the bottom of the fusion zone, Fe concentration was measured at 18-30%, 4-6 times as much as the allowable concentration of 5% Fe in IN625 alloy. This composition trends toward the nominal IN625 values near the top of the fusion zone. The Fe gradient likely serves to suppress solidification cracking by creating a gradient in mechanical properties across the

interface and throughout the fusion zone. This Fe gradient was not visible through SS316L samples. The consequence of the stark change in composition is an abrupt difference in mechanical properties and coefficient of thermal expansion. A slight gradient in Cr was noted, with decreased Cr near the PMZ interface. The variation in Fe, Cr, and Ni composition throughout the FZ indicates there are likely multiple allotropes of iron present in SS316L samples.

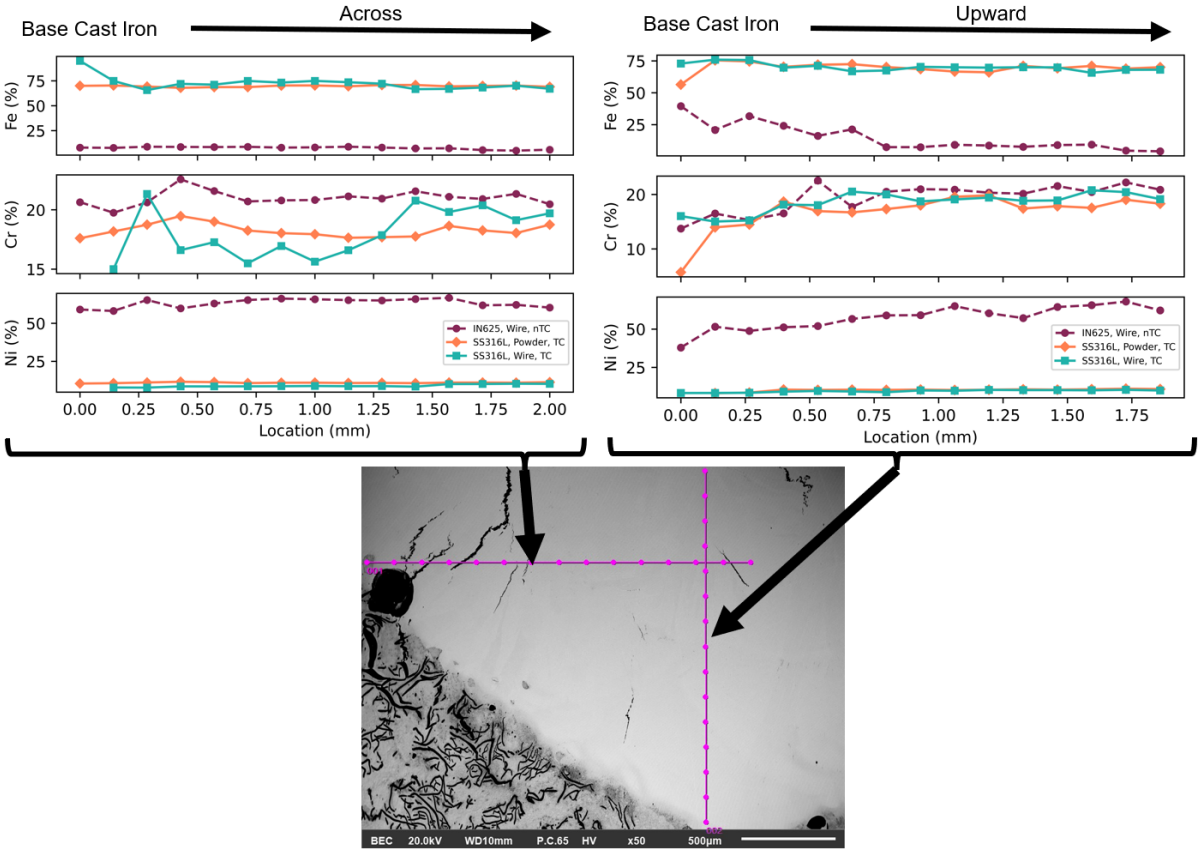

Figure 8. EDS composition of the major constituent metals (Fe, Cr, Ni) throughout the FZ for each filler material.

The propensity for ferrite, martensite, and austenite formation in Fe-Ni-Cr alloys is commonly predicted through Schaeffler's diagram [108]. The SS316L and IN625 alloys in this study are especially interesting to examine owing to the high carbon content in the bands and diluted regions. Alloys rich in Ni, C, N, and Mn favor austenite formation, while alloys with Cr, Mo, Si, Nb, and Al favor ferrite formation. Within the IN625 melt pool, there are sufficient amounts of Ni and C, and the formation of ferrite was suppressed. Instead, the mixture maintains the austenitic structure of the surrounding filler.

Within the SS316L melt pool, the comparatively low Ni content creates conditions where a combination of austenite, ferrite, and martensite was possible. Mixtures of ferrite and austenite are generally preferred for crack resistance [108]. However, in the case of cast iron repair, austenitic structures are preferable due to their higher C solubility than that of ferrite. The FCC austenitic crystal structure maintains larger interstitial sites for C atoms to occupy compared to BCC ferrite. Because of this, less C was rejected during solidification in Ni-based IN625 and less was available in the PMZ for martensite and ledeburite formation.

The composition across the FZ/PMZ interface was measured at the evenly spaced points in Figure 7(a, c, e) and displayed in Figure 9. C atoms are maintained in IN625 over 0.18 mm from the FZ/PMZ interface. C atoms are also observed albeit to a lesser extent in SS316L wire deposits. It is likely that the austenite in the Fe bands (Figure 7(d)) contain C in solution with Fe. However, as noted earlier, the lower Ni content in SS316L discourages austenite formation and carbon solubility. The Fe bands are also observable as elevations in Fe concentration and depressions in Cr concentration between 0.15 and 0.18 mm. Equivalent Ni and Cr concentrations are calculated from the observed elemental compositions and plotted on Schaeffler's diagram (Figure 10). Both SS316L modes were expected to form martensite in addition to austenite and ferrite in the FZ. This was exacerbated near the PMZ interface, where decreased Cr composition shifts the solidification mode into full martensite. Neither alloy achieved the preferable austenite and ferrite solidification mode. IN625 successfully avoided martensite formation throughout the PMZ and FZ, making it an ideal candidate for crack avoidance. Although the microstructures are primarily martensite and ledeburite near the FZ/PMZ interface, it should be noted that both Ni and Cr were observed within the PMZ for IN625 wire and SS316L powder samples. This indicates there was sufficient melt pool motion to dilute portions of the filler material within the cast iron despite low thermal input. In both cases, insufficient concentration of Ni and Cr hindered the formation of austenite or ferrite.

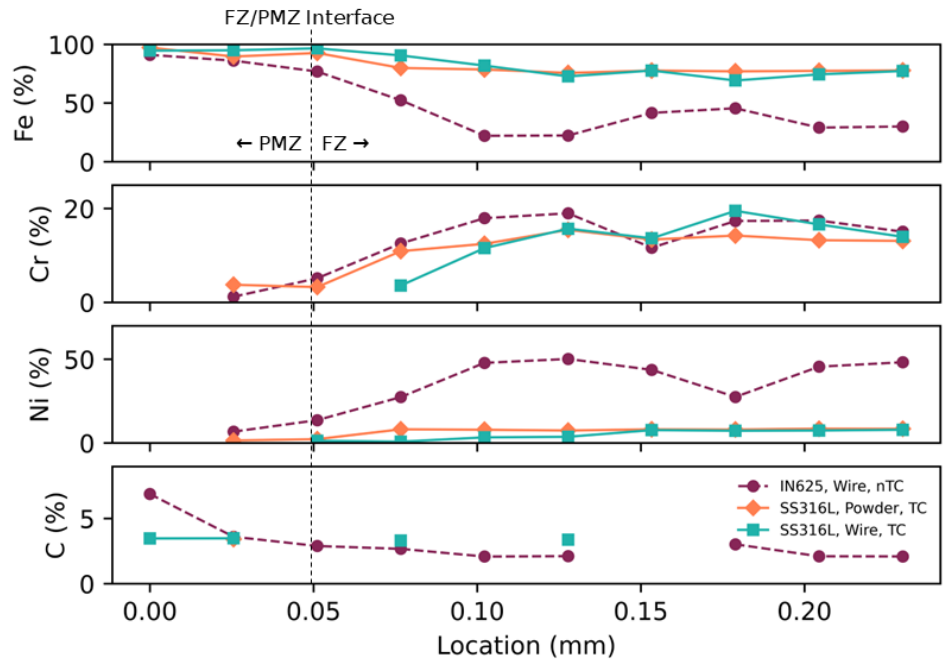

Figure 9. Elemental composition of each sample across the FZ/PMZ interface as observed by EDS.

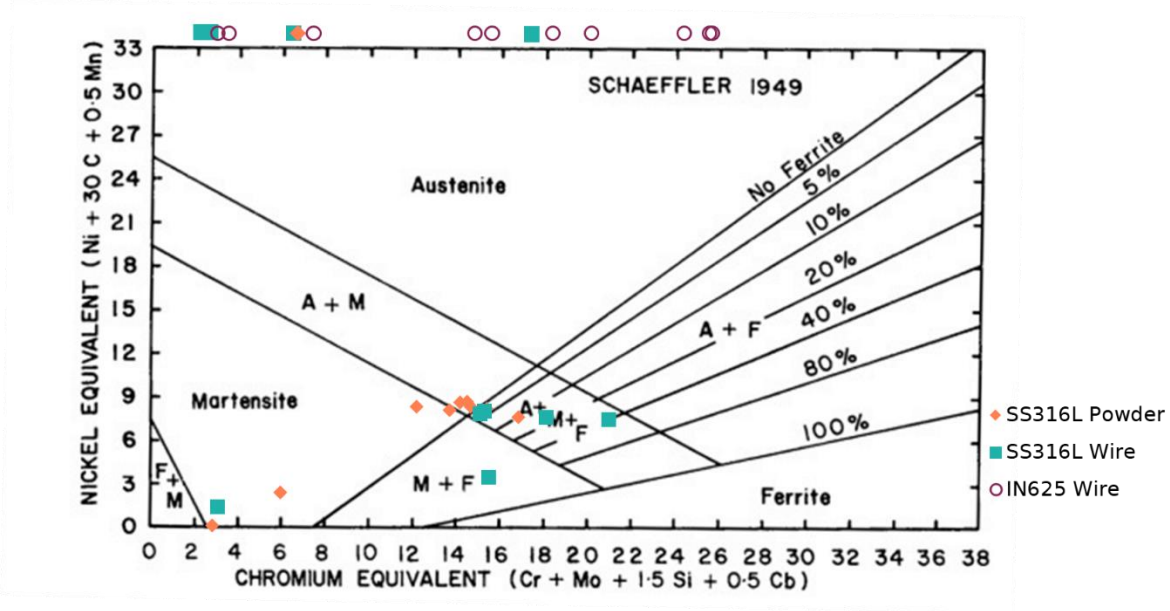

Figure 10. Schaeffler's diagram for each alloy condition calculated from the measured elemental compositions. Points above the chart lie above the upper Y-axis limit.

3.2 Microhardness

Samples were subjected to microhardness measurements within the FZ to unveil the compositional effects on material strength (Figure 11). Each material combination showed a spike in

hardness at the PMZ interface where martensite was present. Measurements showed consistency with only minor decreases in microhardness upward through the FZ. These trends confirm the compositional observations and predictions in the previous section: the concentration of hard martensitic phases decreases as distance from the PMZ increases. Near the top of the FZ, softer austenite and ferrite phases create regions of lower microhardness.

IN625 also showed a change in microhardness between 0.6 and 0.85 mm upwards from the interface. This decrease corresponds to the change in Fe noted in Figure 8. This confirms previous inclinations that the gradient composition induced a gradient in mechanical properties. The strength gradient is likely better at suppressing the thermal stresses induced by fusion processes and is likely the reason for nearly no fractures present within the IN625 FZ.

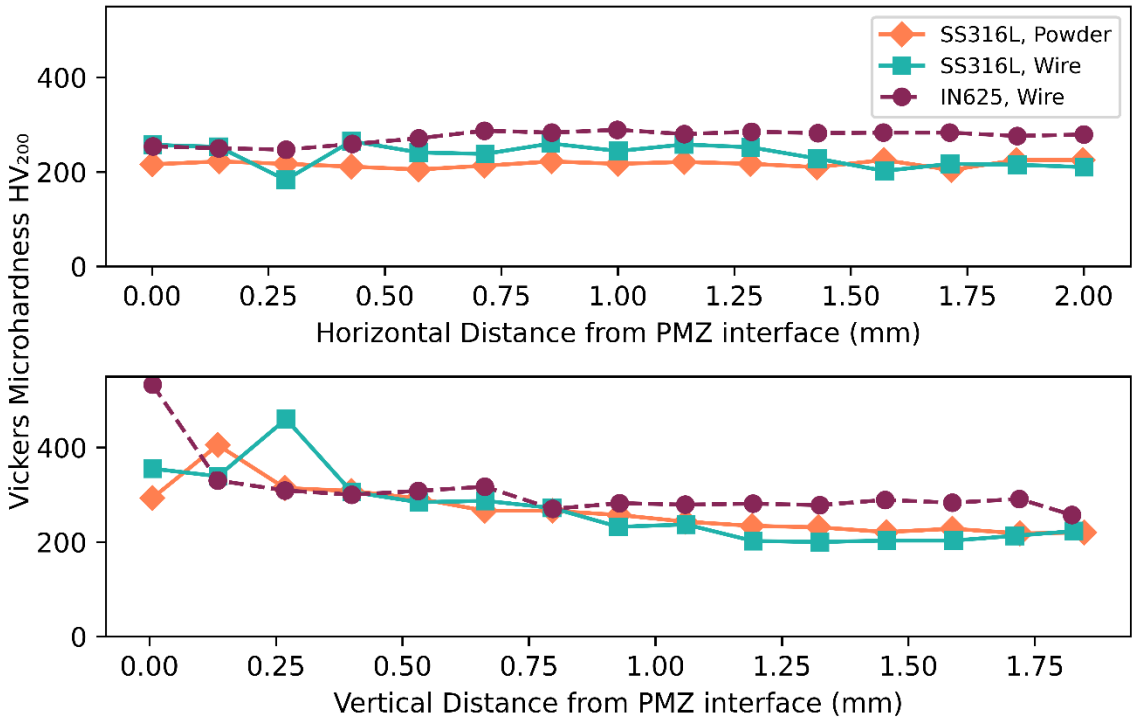

Figure 11. Microhardness at locations horizontally and vertically from the PMZ as depicted in Figure 8.

3.3 Porosity

Varying levels of porosity and fracturing were formed during the deposition process, and these are visible in Figure 12. The SS316L powder sample showed large, round pores within the FZ and small

pores above the bimetallic interface. This behavior aligns with previous work with cast iron [27], [61], [101]. Oxidation within the melt pool encourages gas generation and entrapment in the rapidly solidifying melt pool. SS316L wire also produced small interfacial pores but showed less trapped gas porosity within the FZ. IN625 samples showed considerably less gas-generated porosity but suffered from lack-of-fusion pores near the bimetallic interface. This is likely a consequence of inadequate thermal input or improper stepover to fill the empty regions between deposition tracks [109]. While the non-spherical geometry of lack-of-fusion porosity is detrimental to the fatigue life, these defects require only trivial modifications to the process parameters to prevent.

Solidification cracking was present throughout the repair as previously noted in the microstructural analysis. These fractures followed both longitudinal and transverse directions relative to the laser travel direction, indicating that the stresses produced during laser deposition were also bidirectional. All samples produced interfacial fractures within the PMZ. Unsurprisingly, the brittle phases found within the PMZ were unable to remain intact under the thermal stresses produced during DED.

Figure 13 shows the quantitative distribution of pore diameters for each sample. Repairs with SS316L powder produced more pores of all sizes than wire samples. While several argon gas flows are incident to the melt pool in powder deposition, the complex fluid dynamics between discrete powder particles, their carrier gas flow, and the surrounding shielding gas flow likely creates turbulence that introduces oxygen to the melt pool. The high surface energy of the powder particles also captures moisture, introducing additional contaminants into the melt pool [110]. Additionally, the melt pool in powder DED is primarily comprised of the substrate with periodic incorporation of powder particles. During wire DED, the majority of the melt pool volume is formed from continuously melting wire. The consequence of this is that the GCI undergoes direct laser exposure in powder DED which preferentially vaporizes graphite particles. With wire DED, the larger melt pool and indirect laser exposure allow for graphite to diffuse into the melt prior to laser exposure. This is likely why wire feeding generally produced the fewest number of pores.

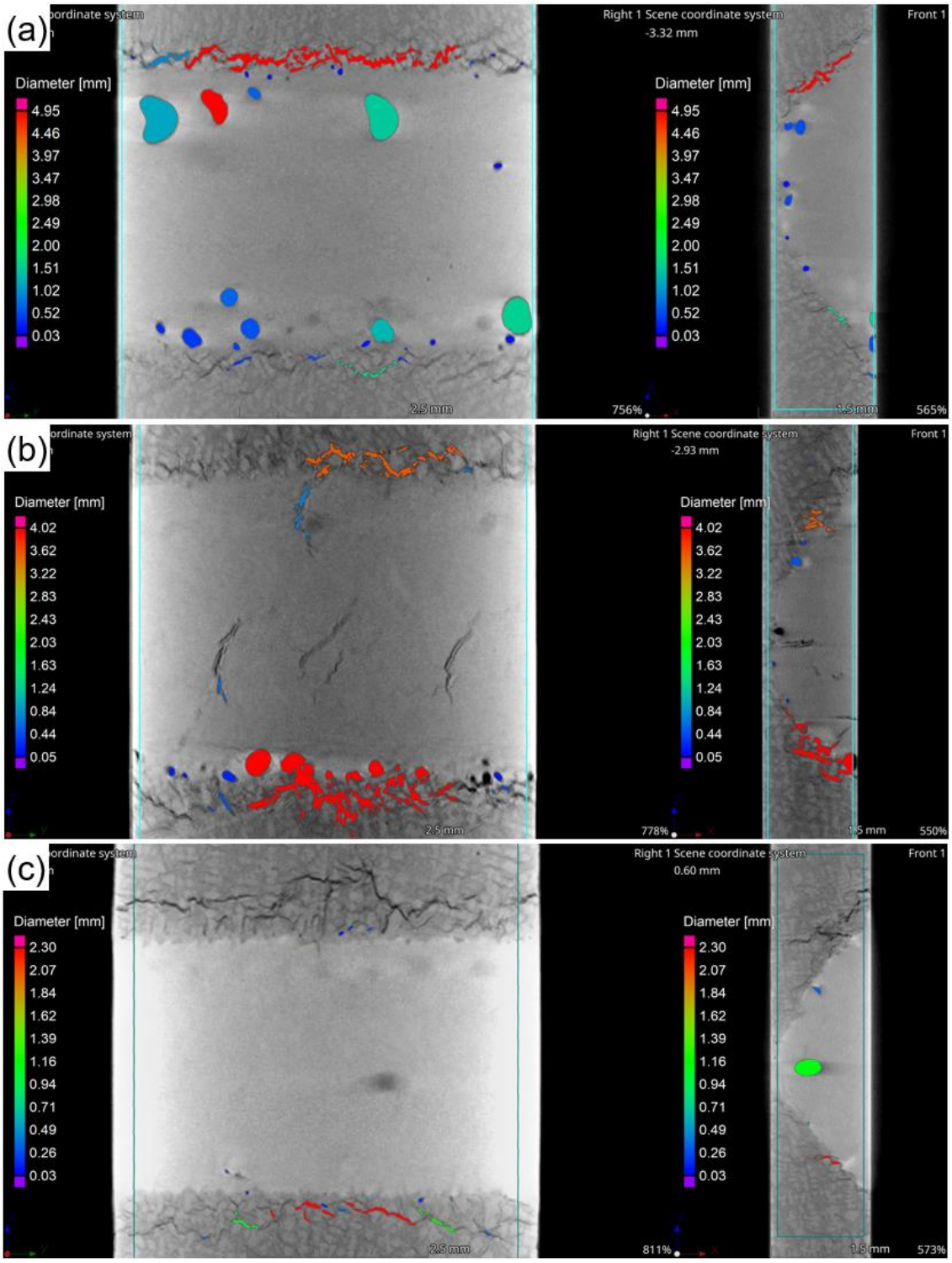

Figure 12. X-ray computed tomography scans of GCI interfacial strength bars repaired using (a) SS316L powder, (b) SS316L wire, and (c) IN625 wire using laser DED.

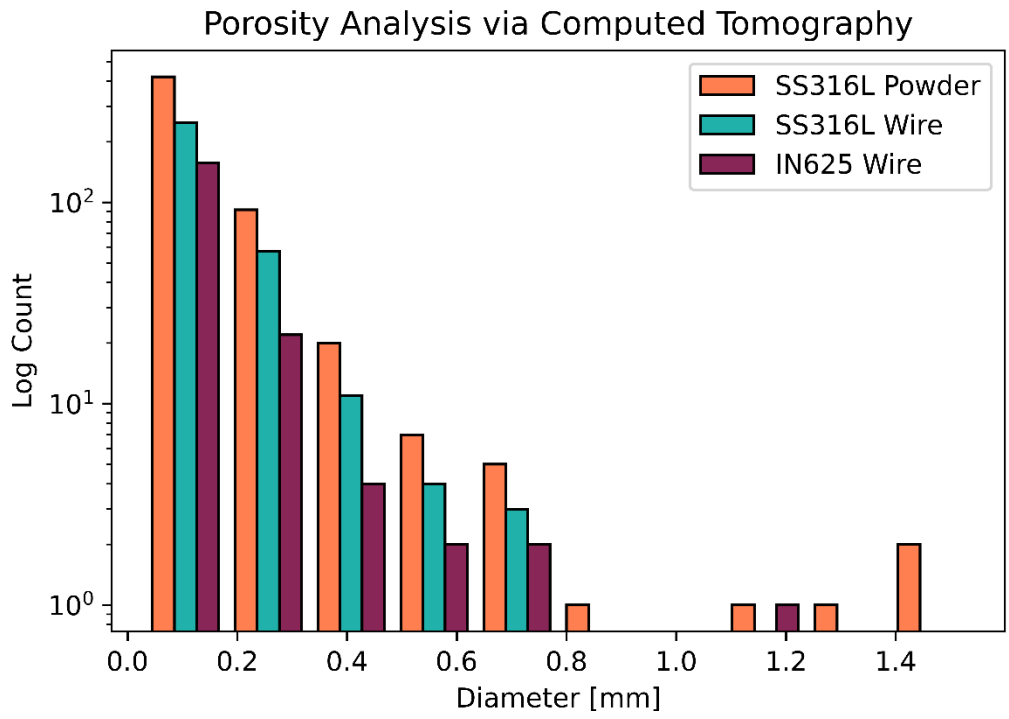

Figure 13. Porosity quantified via CT analysis for all conditions.

3.4 Interfacial Strength Samples

The tensile strength of remanufactured GCI with each alloy composition is shown in Figure 14. SS316L powder showed the highest ultimate tensile strength, achieving 98.8% of the original gray cast iron strength on average (Standard Dev. of 7.6%). SS316L wire showed similar repair integrity, successfully regaining 97.7% of the cast iron strength (Standard Dev. of 4.4%). The decreased ductility in the wire sample is likely a product of the solidification cracking visible in microstructural images. IN625 wire restored 85.9% of the cast iron strength in absence of preheating and annealing (Standard Dev. of 4.8%). Application of these thermal cycles would increase this strength.

As expected from the PMZ/HAZ fractures visible in CT images (Figure 12), samples primarily broke at the FZ/PMZ interface. The martensite and ledeburite structures have inherently low ductility, creating a zone where brittle fracture was prominent. Because of this, the gas porosity and thermal cracking in the FZ for SS316L were negligible defects with regard to the overall strength of the repair.

Reduction of these defects remains important, however, improving the interface microstructure proves to be the next meaningful challenge for restoring the material strength to its original state.

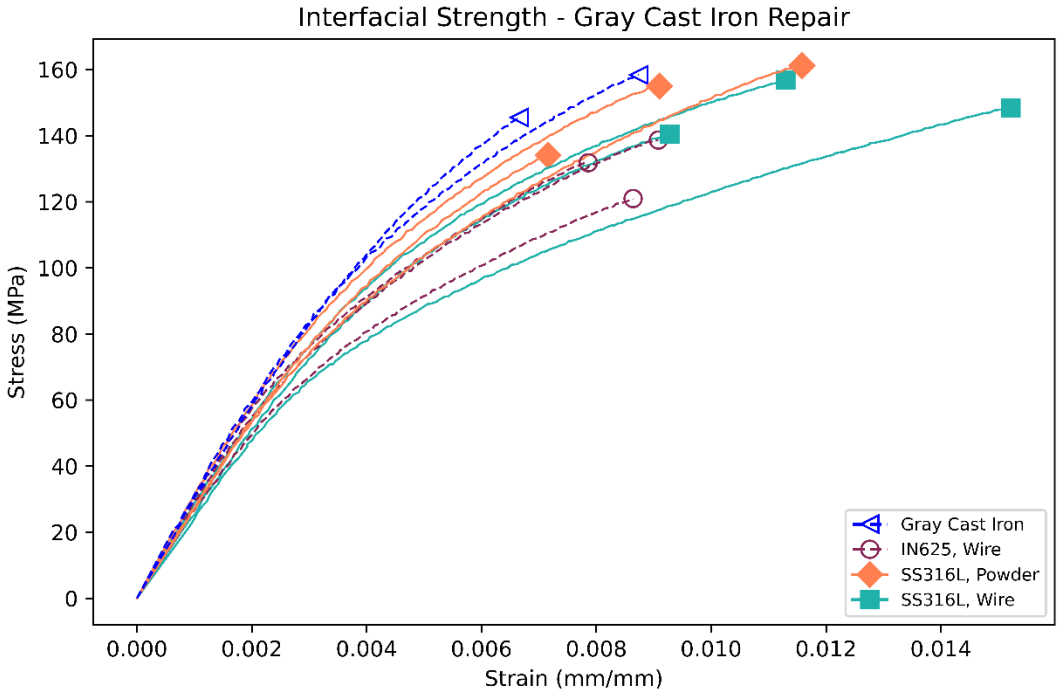

Figure 14. Tensile strength of repaired cast iron groove samples.

4. Discussion

In selecting alloys to contribute to GCI repair, special attention must be paid to the composition of major constituent metals: Fe, Cr, and Ni. The concentration of each element throughout the FZ will affect the propensity for brittle phase formation and the diffusion of C from the base cast iron. Successful repairs should minimize martensite and ledeburite formation through 1) preheating and slowly cooling restored volumes and 2) selecting alloys that are amenable to C absorption. Although GCI tensile strength was only fully regained when preheating and annealing were performed, the restoration of 85.9% strength with IN625 in absence of heat treatment is notable. Preheating and annealing add significant time and cost to the remanufacturing process, and these expenditures increase exponentially with increasing part volume. The ability to remanufacture cast iron in absence of heat treatment expands applicability of DED to large components, remote locations, or in-service structures. Further work should be conducted on similar Ni-base alloy performance in laser-based DED remanufacturing.

Another aspect of the process to consider is the input material geometry. Powder and wire diffuse into the melt pool differently, creating inherently different process physics and regimes for process stability. Because of the low surface energy to volume ratio, wire requires less energy per unit volume to overcome surface tension before diffusing into the melt pool. Previous work has shown that powder particles, when not immediately absorbed into the melt pool, float on the surface before diffusing into the liquid [111]. This requires energy transfer from the melt pool and absorption of the incident laser energy, leaving less energy for gas porosity migration out of the melt pool. On the other hand, powder can be deposited at lower laser power owing to stochastic powder capture. A significant fraction of powder particles, often between 30-60%, are not captured in the process [112], leaving considerably more laser energy per unit mass to melt the captured particles. Wire DED often captures 100% of the incident wire due to the continuity of wire. The consequence of this means that, for common wire diameters (0.75-1.1 mm), sufficient laser energy must be provided to fully melt the wire and maintain the melt pool. Herein, powder was able to be deposited at lower thermal input, creating a shallow dilution zone with minimal brittle phase formation. The tradeoff is the formation of additional trapped gas porosity and the high cost and safety risks of gas atomized powder. Future work in GCI remanufacturing should explore low thermal input of DED using powder and wire filler materials. Wire-laser DED remains a relatively nascent process, and the process windows for different alloy systems and wire diameters are largely undefined. This work serves to bridge the state-of-the-art between powder and wire DED processes. Additional work should be conducted to find the optimal deposition parameters for wire-based DED remanufacturing.

One of the key areas for remediation is the formation of interfacial fractures. All samples showed fractures within the PMZ, a consequence of brittle phase formation and the non-uniform deformation produced during localized thermal input. It should be noted that, despite performing nearly as well as the original GCI, these fractures would contribute significantly toward premature failure under cyclic loading. In applications where fatigue life is critical, crack prevention remains a priority. While IN625 showed favorable porosity remediation and gradient composition throughout the FZ, the thermal stresses during deposition and the carbon-rich phases at the interface promoted solidification cracking. Reduction of non-

uniform stresses requires a reduction in the thermal gradient during deposition. This may be achieved through preheating and slow cooling of the cast iron core and a reduction in the laser energy input during remanufacturing operations. Even with these prescriptive actions, the high carbon content in GCI remains a difficult aspect of cast iron remanufacturing. Future technology development should focus on 1) quantifying and minimizing thermal stresses produced using specific deposition conditions, 2) detecting fracture formation in-process, and 3) providing fracture remediation steps in situ.

5. Conclusions

Gray cast iron was successfully remanufactured using SS316L and IN625 filler materials in laser directed energy deposition (DED). In-process preheating and annealing cycles restored 97.7-98.7% of the cast iron tensile strength using both stainless steel 316L wire and powder materials. Without in-situ heating, IN625 restored tensile strength up to 85.9%. Porosity and fractures within the fusion zone are noted for all alloys and are more prominent in SS316L samples. Gradient Fe concentration and high Ni content allow IN625 to suppress significant thermal stresses and create gradient mechanical properties throughout the fusion zone. The lower thermal input in the laser DED process allows for considerably less dilution than comparable arc-based processes and a reduction in brittle phase formation. This, combined with careful alloy and process parameter selection, present laser-DED as an ideal candidate for gray cast iron remanufacturing. On a broader scale, wire DED promises higher deposition rates and efficiency with lower safety risks and operating costs compared to powder processes. Continued research in wire DED serves to increase process reliability through a robust understanding of process physics.

Acknowledgements

The authors would like to thank the AMPrint Center at RIT for the use of their microscopes and characterization equipment. Likewise, many thanks are in order to Jeremy Siegfried and Dr. Michael Thurston in the Golisano Institute for Sustainability at RIT for assisting in microhardness

characterization. The authors would also like to thank Samantha Sorondo within the Industrial and Systems Engineering Department for her assistance with metallurgical preparation.

Funding

This paper received no funding for the conceptualization, research, and outcomes for the results.

Competing Interests

The authors have no competing interests to report.

Chapter 4 – Visualization of Melt Pool Stability for Wire- and Powder-based Directed Energy Deposition Repair of Gray Cast Iron[‡]

Jakob D. Hamilton[a], Iris V. Rivero[a]

[a] Department of Industrial and Systems Engineering, Rochester Institute of Technology, One Lomb Memorial Drive, Rochester, NY 14623

Corresponding Author: Iris V. Rivero, iris.rivero@rit.edu, One Lomb Memorial Drive, Rochester Institute of Technology, Rochester, NY 14623

Abstract

Gray cast iron is favorable in agricultural and automotive castings for its high strength and wear resistance but offers difficulty during remanufacturing. Key challenges include restoring strength while avoiding brittle phases and porosity. While wire-based directed energy deposition (DED) repair studies are limited, powder-based DED has shown promise under specific thermal conditions. Determining these conditions is challenging due to the localized and transient nature of the process. Herein, in-situ high-speed imaging was employed for quantifying melt pool stability for optimal thermal conditions in wire- and powder-based DED repair of gray cast iron. The rate of gas generation and escapement from the melt pool was driven by laser power and traverse speed. Stable deposition conditions, i.e., minimal melt pool geometric deviation, are identified for both media types, and the resultant strength is quantified. The insights provided by in-situ imaging promote superior parameter selection and is extendable to other difficult-to-repair materials.

Keywords: additive manufacturing, repair, directed energy deposition, gray cast iron

1. Introduction

Gray cast iron is a widely used iron alloy in the automotive and transportation industries. Owing to its high strength and thermal stability, engine blocks, cylinder heads, and housings are often composed of gray cast iron. Remanufacturing of worn or defected cast iron components is of specific interest, as developing tooling for re-casting one-off components is typically cost prohibitive [113]. The design

[‡] This chapter is in preparation for submission to Scripta Materialia.

specifications and tooling required for manufacturing equivalent replacements for these components are often incomplete or unavailable, making remanufacturing a viable approach for replacement. Seminal research in remanufacturing aims to address physical limitations and lower the cost for adoption within the industrial sector [114], [115].

Arc-based welding processes have typically been employed in remanufacturing processes but not without limitations. The high heat input and rapid solidification rate contribute to brittle cementite (FeC_3) phase formation at the cast iron weld interface, regardless of the filler material composition [61], [67]–[69], [101], [116], [117]. Porosity formation is also a known problem as free carbon may vaporize or react with surrounding oxygen and form gas-trapped voids in the solidifying melt pool [68], [116]. Traditional pathways around these limitations require preheating and post-process annealing and filler metals with low carbon solubility, i.e. Ni and Ni-base alloys. Minimizing porosity requires balancing the thermal input to minimize dilution into the substrate material. Additional process parameter considerations are required when working with dissimilar filler material compositions [69], [70].

Laser-based directed energy deposition (DED) has been offered as a potential solution to these issues. Employing a laser allows for a more controllable thermal process and the potential to mitigate the above issues. Research within gray cast iron repair literature has primarily focused on optimizing and expanding the window of acceptable process parameters within powder-laser DED [61], [69], [116]. The thermal input, dictated by laser power and scanning speed, has been shown to greatly affect porosity formation and the resultant material strength.

Despite recent successes with powder, adoption of DED within industry will benefit from low-cost, low-maintenance filler materials. Wire offers similar performance to powder at a reduced cost and without flammability and health hazards of powdered metal. Wire typically offers material utilization up to 100% as compared with the <30-90% captured in powder DED [118], [119]. This allows wire to hold substantially higher deposition rates than comparable powder deposition. Despite this, little work has explored wire as a potential feedstock alternative in laser-DED cast iron repair.

This study explores process windows for both wire-laser and powder-laser DED and translates process parameter sets between media delivery modes. Key outcomes for this translation are thermal input, melt stability, track geometry, and material strength. In this pursuit, deposition outputs are quantified, and the relationship between feeding modes is established. Process differences such as gas flows and melt pool dynamics are offered as explanations for observed process differences. The findings of this study expand the regime of acceptable process parameters for atomized powder and low-cost wire in laser DED with a specific emphasis on gray cast iron repair.

2. Methodology

2.1 Experimental Setup

A 5-axis CNC machine retrofitted with a Hybrid Manufacturing Technologies (McKinney, TX, USA) AMBIT FLEX system was used for deposition. Separate wire and powder deposition heads were used for depositing stainless steel 316L (SS316L) welding wire (d=1.07 mm) and gas atomized powder (d_{10}=49 μm, d_{50}=61 μm, d_{90}=92 μm). While Ni-base alloys are preferable in high carbon steel applications, Fe-Ni-Cr alloys are commonly used for their low cost and excellent weldability [66], [117]. Gray cast iron (GCI) plates were used as substrates (ASTM A48 Class 40). Supplier chemical compositions of these materials can be found in Table 6.

Material	**C**	**Cr**	**Cu**	**Fe**	**Mn**	**Mo**	**N**	**Ni**	**O**	**P**	**S**	**Si**	**Sn**
GCI plate	3.12	-	0.38	bal.	0.71	-	-	-	-	0.15	0.09	2.20	0.05
SS316L	0.01	17.0	<0.01	bal.	0.80	2.3	0.2	12.1	0.03	<0.005	0.004	0.45	-

Table 6. Chemical composition (wt%) for the substrate and powder used in the experiment.

It should be noted that the gas flow behavior and nozzle geometry fundamentally differ between powder and wire deposition heads. While these factors are likely to affect the resultant melt pool behavior, the deviations are assumed negligible within this research. The complex gas flows are significantly understudied in DED literature and uncovering the effects of these variations is outside the scope of this work. Other head-specific parameters are presented in Table 7.

Attribute	Powder	Wire
Spot Size	2.4 mm	2.0 mm
Nozzle Gas	10 L/min	20 L/min
Shield Gas	5 L/min	-
Carrier Gas	2 L/min	-
Material delivery	Coaxial around the vertical axis	60° along vertical axis

Table 7. Process parameters for the powder and wire feeding deposition heads.

2.2 Experiment

Initial single-track experiments were conducted to quantify melt pool stability and calculate track geometry. Microstructure along the bimetallic interface was also studied, as brittle intermetallic phases formed during solidification are prone to failure. To test the resultant strength of the repair, interfacial strength samples were fabricated (Figure 15). Grooves were machined in cast iron plates and subsequently filled using DED. Tensile samples were then machined from the plate. Powder repair adhered to guidelines set forth in previous work [104]. Wire samples were completed in two layers: 3 tracks on layer 1, and 4 tracks on layer 2. To prevent brittle phase formation, the plates were heated to 300°C prior to deposition and held at temperature for 2 hours after deposition was finished.

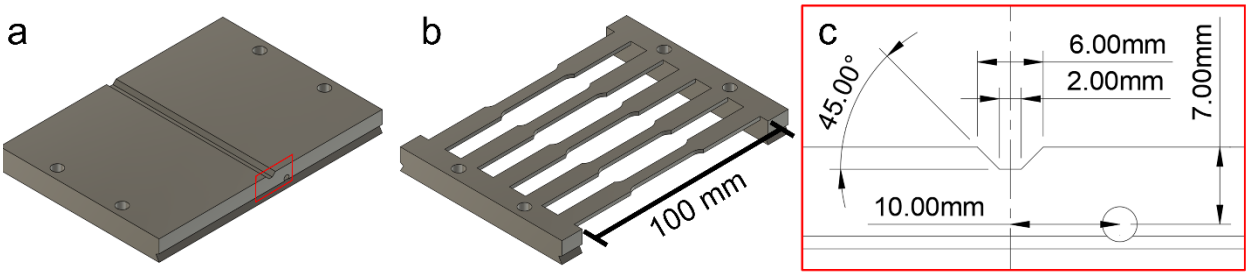

Figure 15. Drawing of the trapezoidal groove cross section and thermocouple location with dimensions.

2.3 Characterization

In-situ melt pool images were gathered using an Edgertronic SC2+ high-speed camera (Campbell, CA, USA). A low pass (<950 µm) optical filter was placed in front of the lens to block laser emissions toward the CMOS detector. Images were taken at 2,500 Hz with an ISO of 1,600 and a shutter speed of 50,000 Hz. Pixel scale at the focal plane was identified as 18.5 µm per pixel. Melt pool identification was

completed with a Python script. Noise-reducing Gaussian blur was applied to images and followed by Otsu thresholding to identify continuous light and dark regions. The melt pool region was then selected using position and size characteristics and the equivalent diameter was calculated. In this study, equivalent diameter is defined as the diameter of a circle containing equal area as the melt pool region.

Computed tomography (CT) was also performed to understand porosity formation under both wire- and powder-fed conditions. Porosity analysis was performed using VGStudio MAX from Volume Graphics, Inc. (Charlotte, NC, USA). Tensile testing was conducted on interfacial strength samples. A 2,500 kg load cell measured tensile force at 10 Hz. Strain rate was taken from crosshead displacement and kept constant at 2.0 mm per minute. Microstructural analysis was conducted on unbroken tensile samples that were epoxy mounted, ground, polished, and etched for 7 seconds in nitric acid (3 vol%) in ethanol (97 vol%).

3. Results

3.1 Melt Pool Stability – Single Tracks

As a direct comparison of parameters, tracks with identical laser power, scanning speed, and material feeding rate were deposited with wire and powder. High-speed images of powder and wire deposits at 1,500 W, 500 mm/min, and 11.7 g/min are shown in Figure 16. In the powder track, the melt pool exhibits transient size behavior; the melt pool grows as gas is generated and collapses when the gas bubble pressure exceeds the molten metal surface tension. This adheres to behavior observed in previous work. In the plotted melt pool diameter (Figure 17), these events are visible as repeating peaks 150% above the typical melt pool diameter. High-speed imaging of the wire track showed mostly consistent melt pool behavior. Stubbing of the wire produced minor instabilities in the melt pool size. Movement of the laser plume was also captured in this data, likely contributing to the deviation.

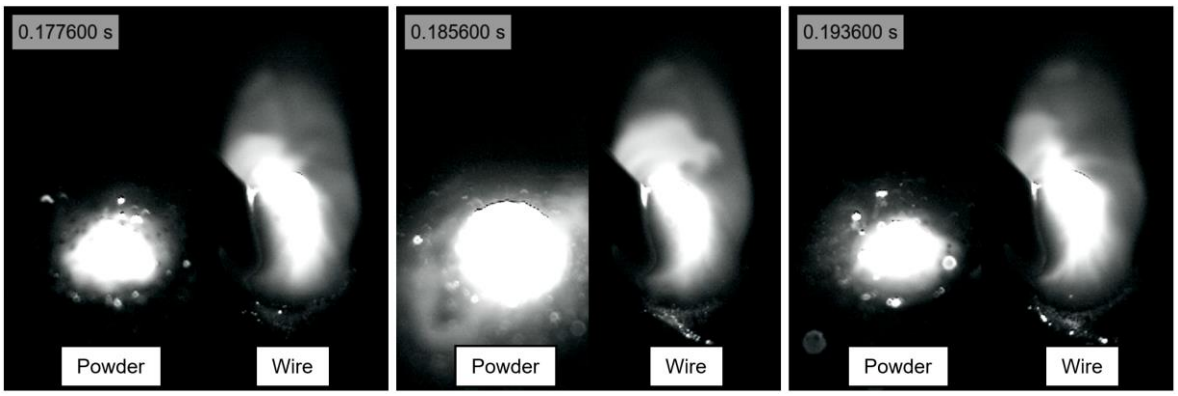

Figure 16. High-speed melt pool images for powder and wire deposition. The transient size behavior is visible in the powder images. Accompanying videos are provided in the online version of this text.

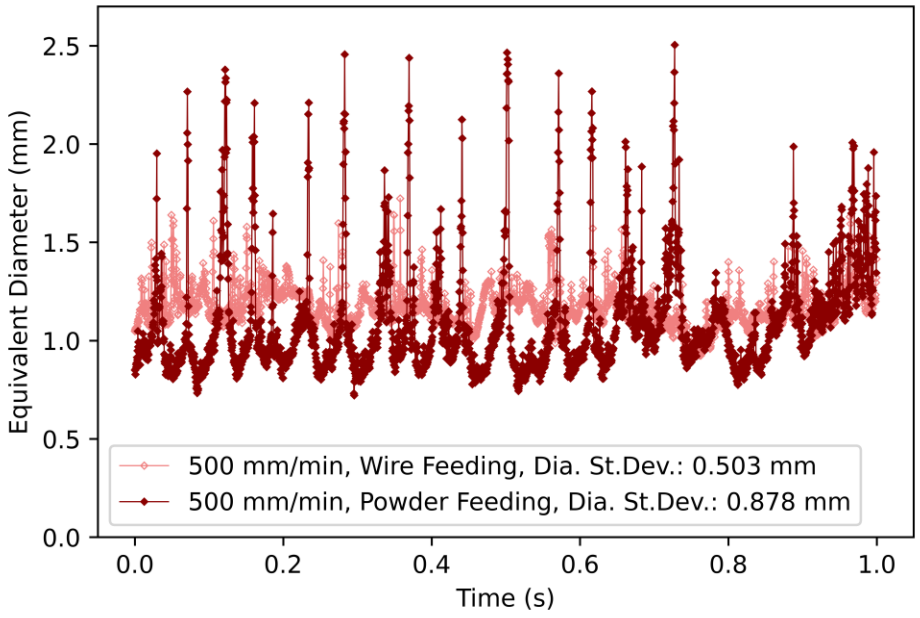

Figure 17. Equivalent diameter of the melt pool over time for wire and powder tracks at 1,500 W, 500 mm/min, and 11.7 g/min.

Further tracks were printed in a two-factor experiment for laser power and scanning speed. In these tracks, wire deposits continued to show consistently stable melt pool behavior (Figure 18). Few gas escapement events were observed, and process instabilities were inherent to the wire feeding process, i.e., stubbing or wire movement. Conversely, stability in powder deposition was dependent on process parameter selection. Parameters with high energy input, i.e., high power and low speed, initiated more gas escapement events. Low laser power tracks produced notably lower pool diameter deviation, nearly matching the stability of the wire tracks. This is evident when the standard deviation of the melt pool size

is plotted for each process parameter (Figure 19). For powder feeding, the notable decrease in melt pool size variation for low power samples suggests laser power should be minimized during deposition. Previous work in powder DED has also shown higher tensile strength at lower thermal inputs [116]. Additional powder tracks deposited at 750 W laser power demonstrated melt pool diameter deviations of 0.299 mm for 350 mm/min and 0.244 mm for 650 mm/min, i.e., 69% and 67% decreases in melt track instability, respectively. Wire tracks deposited at 750 W showed insufficient laser power to form stable beads.

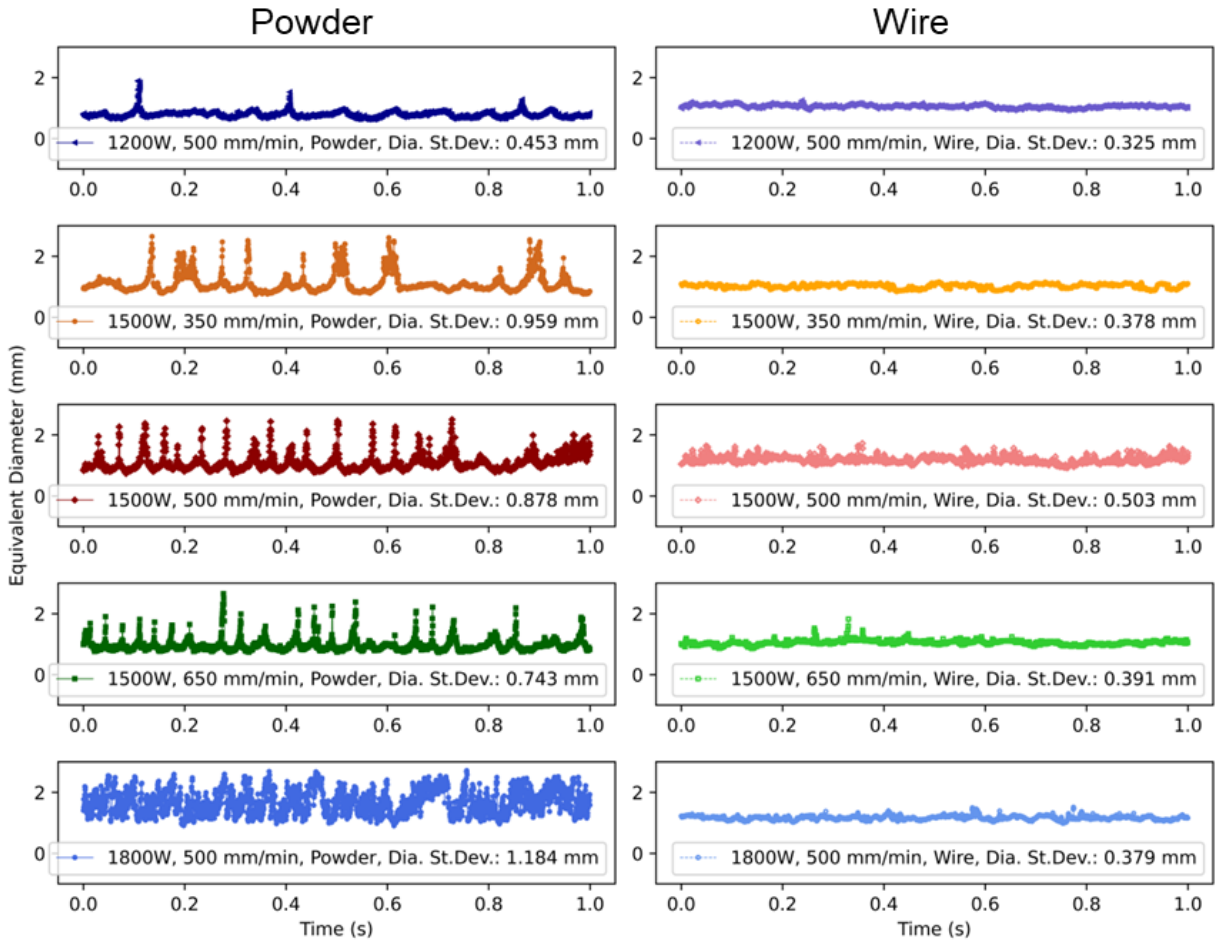

Figure 18. Melt pool size behavior for single tracks in the power and scanning speed factorial experiment.

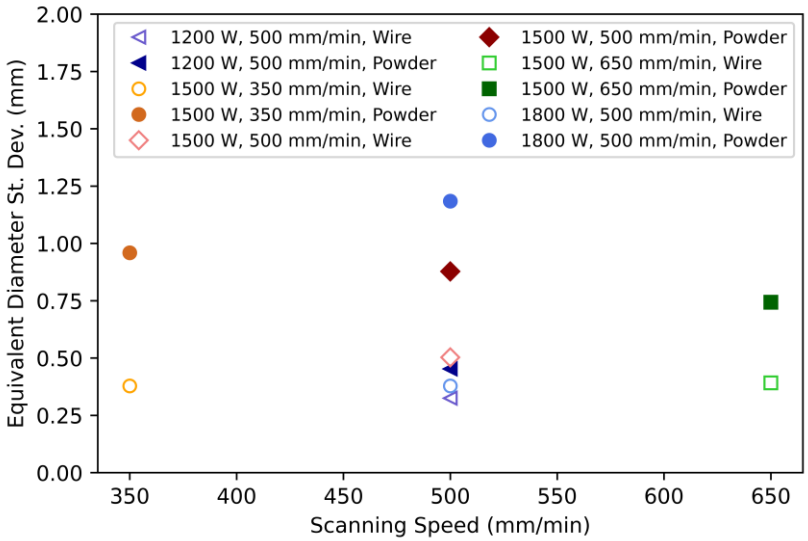

Figure 19. Melt pool size standard deviations for each of the single-track process conditions between powder and wire.

3.2 Melt Pool Stability – Interfacial Strength Sample

Figure 20 shows plotted melt pool stability between the selected process conditions. In both powder and wire samples, the melt pool size deviation remains in the stable range identified in Section 3.1. To ensure continuous conduction between the wire and melt pool, wire feeding rate and scanning speed were increased above the tested levels. Because of this, wire deposition showed higher error than normal due to wire stubbing the bottom of the melt pool. This is visible in melt pool images as the wire position quickly shifts toward the front of the melt pool and gradually moves backwards.

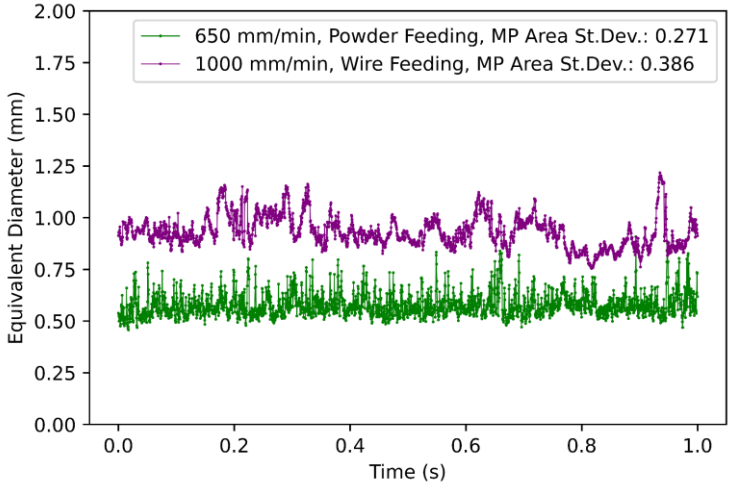

Figure 20. Melt pool stability for nominally stable powder and wire single-track samples.

3.3 Interfacial Tensile Strength

Tensile testing revealed the subsequent strength between feeding modes (Figure 21). For powder samples, the ultimate tensile strength of the cast iron was restored to 98.7% (Standard Dev. of 7.6%) using low thermal input process parameters, i.e. low power and faster scanning speeds. At 350 mm/min, interfacial strength showed a 40% decrease compared to 650 mm/min samples. The sensitivity to deposition parameters is indicative of the effect of localized heat input. Parameters that encourage deeper dilution result in lower interfacial strength [116]. Wire deposition restored tensile strength to 97.7% (Standard Dev. of 4.4%) of the cast iron strength, albeit with higher elongation than powder samples. Although the requisite laser power for stable melting was higher in wire samples, the resultant strength was similar. This is in part to the differing melt pool kinetics between the feeding modes.

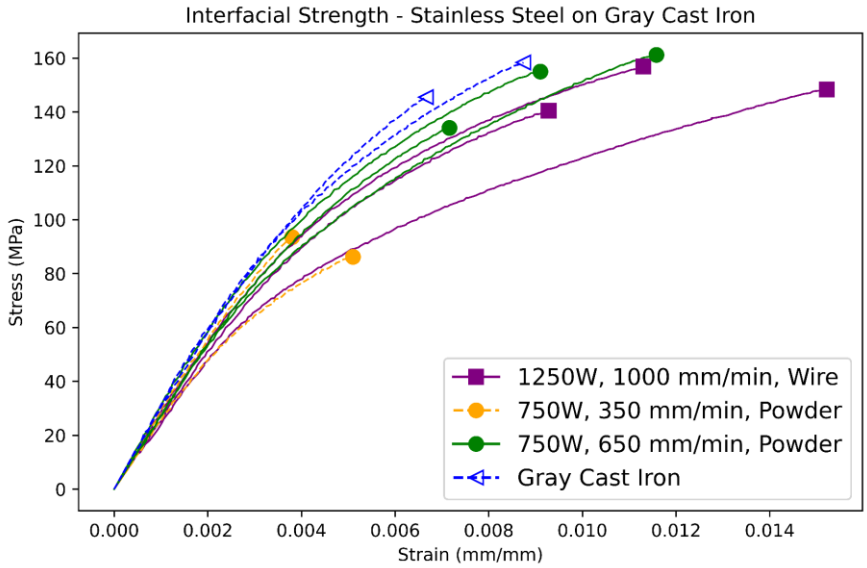

Figure 21. Interfacial strength for nominally stable process parameter combinations.

3.4 Porosity

CT scans of SS316L/GCI interfacial strength samples are shown in Figure 22. Small, round pores formed in both material feeding modes. These pores, created by the reaction of graphite with oxygen, form CO and CO_2 within the melt pool that may be trapped during solidification [61], [69], [116]. Larger round pores were also prominent in the powder-fed sample. This is likely an effect of the gas generation and a failure to escape prior to solidification. The wire-fed sample featured flat, plate-like porosity in the

fusion zone with several large pores located on the side walls of the groove. The surface normal to these flat pores was parallel to the laser travel direction, indicating these are most likely solidification fractures within the fusion zone. Pore morphology likely played a key role in the differing tensile behavior within samples. The flat pores created in wire-fed samples would allow for additional strain compared to the round pore morphology [120], [121]. The round pores and limited fractures within powder samples helped maintain the modulus of elasticity close to that of the original gray cast iron. Despite the excessive pore formation, both samples showed excellent strength compared to the base cast iron.

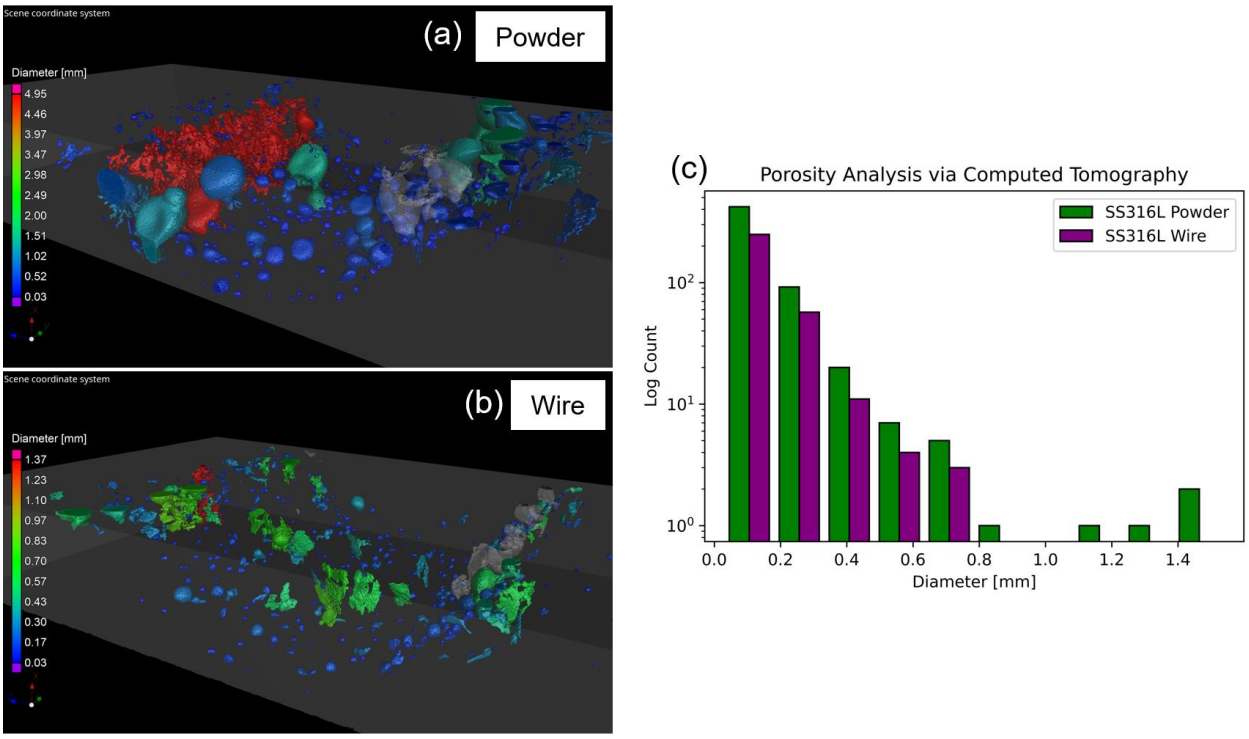

Figure 22. CT reconstructions for (a) powder and (b) wire interfacial strength samples and (c) their respective pore histograms.

4. Discussion

Several major differences are noted between powder and wire feeding modes, especially in the context of gray cast iron repair. Arguably, the most consequential aspect is the melt pool shape. In powder DED, the melt pool is formed from direct laser exposure of the base metal with powder being incorporated to form a cohesive and fully joined track. These characteristics are what make powder DED excellent for high dilution, high resolution printing. This characteristic was notably detrimental in cast

iron repair, however. Direct exposure of the cast iron led to additional formation of gas-trapped porosity, likely from graphite vaporization during laser exposure. In wire DED, the melt pool is primarily formed by the filler material. As the wire is fed toward the substrate, the wire occludes the laser, preventing the cast iron from undergoing direct laser exposure. This allows graphite flakes to diffuse into the liquid metal prior to laser exposure. The dilution into the cast iron is primarily driven by residual heat from the molten wire joining with the substrate.

The wire connection to the melt pool also drastically modifies the melt pool morphology. The high surface tension in the molten metal exerts an upward force along the wire, creating a taller track than a comparable powder processing. The taller track removes the laser exposure farther away from the substrate, improving upon the dilution issues present in powder DED.

The consequence of heat input and laser exposure is evident in high-speed monitoring of the melt pool behavior. As the graphite within the cast iron is vaporized or reacts with residual oxygen, gas porosity forms and may be trapped in the melt pool. This greatly affects the structural outcomes in the material. Understanding the connection between the transient melt pool behavior and structural outcomes allows for better parameter selection and material feeding mode for the desired application, i.e., high vs. low dilution.

The major drawback to wire DED in this study was the requisite thermal input to achieve stable melting. The molten metal transfer from the wire to the substrate is a critical determinant of process stability. Deviations in wire position or thermal input can prevent the wire from melting fully, cause stubbing, or initiate balling along the wire [122]. High laser power ensures the wire will fully melt at a wider range of wire positions, thus widening the window of acceptable process conditions. However, in dissimilar material joining, this excess thermal input exacerbates solidification cracking and porosity. Methods to minimize the thermal input while maintaining melt pool stability are especially well suited for this application.

One of the promising technologies to overcome these limitations is in-process control. In-situ monitoring was demonstrated in this study, however, the computational time for stability analysis

prevents real-time control. Low latency sensor platforms, machine learning, and other computational techniques are well suited for achieving real-time frequency. These technologies would serve the repair of dissimilar materials, specifically stainless steel with gray cast iron, very well.

5. Conclusions

The results described herein present laser-based DED as a feasible technology for restoring the mechanical strength of worn cast iron surfaces. Both wire-laser and powder-laser DED processes were employed for dissimilar deposition of stainless steel 316L on gray cast iron plates. The melt pool dynamics and resultant morphology varies between material feeding modes, creating different limitations within each mode. In-situ monitoring and ex-situ optimization showed that powder deposition is improved with lower laser power. Conversely, higher laser power was required to initiate full melting in wire deposition. In both cases, tensile strength was restored to the original cast iron strength, despite formation of gas-generated porosity and solidification fractures within the fusion zone. These results suggest low-cost wire is suitable as deposition media in laser-based remanufacturing of cast iron components.

Acknowledgements

The authors would like to thank Dr. David Trauernicht and Dr. Denis Cormier for their assistance with CT scanning. The authors would also like to thank the AMPrint Center for allowing the use of their high-speed camera.

Funding

This paper received no funding for the conceptualization, research, and outcomes for the results.

Competing Interests

The authors have no competing interests to report.

Chapter 5 – Part-Agnostic Ultrasonic Melt Pool Vibration in Wire-laser Directed Energy Deposition[§]

Jakob D. Hamilton[a], Irtaza Razvi[a,b], David Trauernicht[a,b], Denis Cormier[a,b], Iris V. Rivero[a]

[a] Department of Industrial and Systems Engineering, Rochester Institute of Technology, One Lomb Memorial Drive, Rochester, NY 14623
[b] AMPrint Center, Rochester Institute of Technology, One Lomb Memorial Drive, Rochester, NY, 14623

Corresponding Author: Iris V. Rivero, iris.rivero@rit.edu, One Lomb Memorial Drive, Rochester Institute of Technology, Rochester, NY 14623

Abstract

Ultrasonic vibration assistance has proven itself as a useful tool in homogenizing microstructures and improving structural properties in localized fusion processes (welding, additive manufacturing, etc.). Current implementations of vibration transmission are geometry-limited, requiring adjacent material to transmit oscillations. Next-generation additive manufacturing processes for large components or non-planar deposition require geometry-independent solutions for microstructural refinement. This study outlines a method of localized, part-agnostic melt pool vibration and preliminary results for the efficacy of improving structural outcomes. In-situ melt pool images confirm vibration transmission and cavitation within the molten material. Grain refinement with ultrasonic vibration corroborates previous literature on the microstructural outcomes with vibration assistance. The outlined methodology shows promise for unifying microstructures within large, multi-axis deposition strategies required in aerospace, agricultural, energy, and transportation sectors.

Keywords: additive manufacturing, directed energy deposition, ultrasonic vibration, melt pool imaging

1. Introduction

Directed energy deposition (DED) additive manufacturing (AM), is a localized fusion-based welding process in which a heat source, typically laser, arc plasma, or electron beam, melts powder or wire at a single location. The localized nature lends itself to building material onto existing structures, i.e. repair and remanufacturing, and pairing with subtractive manufacturing processes to enable hybrid

[§] This chapter is in preparation for submission to Additive Manufacturing.

manufacturing. With its roots in fusion-based welding, DED suffers from similar metallurgical issues: columnar grain formation, residual stresses, distortion, and porosity.

Vibration-assistance has been a popular area of study for defect remediation in fusion-based welding and deposition. Current grain refinement theory speculates that oscillations within a rapidly solidifying melt pool creates acoustic streaming and cavitation which, in turn, encourage grain refinement as solid dendrites fracture and redistribute within the melt [91], [123]. Constitutional supercooling, redistribution of secondary phases, and precipitation mitigation have also been noted [91], [123], [124]. Structurally, this reduces tensile residual stresses, interrupts pore formation, and improves the overall mechanical properties of the solidified structure [91], [95]. The outcomes have been notably amplified at frequencies above ultrasonic (>20 kHz) [125].

Vibration-assistance has been applied in several forms. Most popular implementations include a stage or transmitter which mechanically imparts oscillations to the substrate in one or more of the principal dimensions [91], [95], [123], [126]–[132]. The power requirements for vibrating large parts at ultrasonic frequencies eliminate the practicality of this technique. Similarly, the inertia changes as material is added, resulting in a loss of resonant frequency. While the inertial change in welding may be negligible, the same cannot be said for DED.

Other implementations avoid inertial limitations by providing oscillation through a localized transmitter near the melt pool. This transmitter maintains a fixed distance from the melt pool, thus ensuring consistent vibration kinetics at the melt pool. Zhou et al. implemented a fixed-distance ultrasonic probe to impart oscillations during laser welding of dissimilar Hastelloy and stainless steel alloys [124]. Ultrasonic vibration improved elemental distribution, grain refinement, microhardness, and load capacity of welded joints, proving the effectiveness of this technique. Yuan et al. applied a similar style of fixed-offset ultrasonic probe in laser-wire additive manufacturing [133], [134]. Ti-6Al-4V and stainless steel grains were subject to refinement and a transition from columnar to equiaxed morphology. Lei et al. noted a 13-16% improvement in tensile strength in a laser-welded magnesium alloy with a fixed-offset ultrasonic probe [135]. Strength improvements were attributed to homogeneous elemental distribution and

grain refinement. Liu et al. compared structural implications for fixed-position and trailing ultrasonic probes in welding of stainless steel sheets [136], [137]. The trailing probe showed a lower thermal gradient and longer melt pool tail in simulation, and experimental results showed higher refinement and uniformity with a trailing-probe implementation. While these authors have primarily found success, current implementations are constrained by part geometry. If a deposition layer is smaller than the probe offset distance, the probe will not contact the surface and vibration will not be imparted. Further geometrical limitations of probe-style implementations exist in non-planar or multi-axis deposition strategies.

An attractive alternative to applying vibration to the melt pool is direct vibration through a stirrer rod or through direct vibration of the filler material. The former approach was employed by Singh et al. in an arc welding process [42]. A 2.0 mm thoriated tungsten rod was placed in the melt pool and oscillated at 149 Hz. The authors reported grain refinement and a slight increase in microhardness due to vibrational assistance. Watanabe et al. found success by directly vibrating the filler wire in gas tungsten arc welding (GTAW) [43]. Vibration at 19 kHz refined grains at low welding speeds (<4 mm/s), where grain growth was the dominant solidification mechanism. Although marginal improvements in tensile strength were noted with vibration assistance, elongation was increased significantly.

Application of vibration-assistance in DED has primarily been limited to part-level vibration and semi-localized acoustic transmission. Direct melt pool vibration bypasses the energy and geometric limitations of these methods, but its application has not transitioned from welding to DED processes. This work outlines a direct method of melt pool vibration and its application in laser-wire DED for grain refinement and porosity remediation.

2. Design

The DED process used in this study was a Hybrid Manufacturing Technologies (McKinney, TX, USA) AMBIT FLEX system integrated within a Hardinge (Atlanta, GA, USA) GX250-5axis vertical milling center. The laser-wire deposition head and off-axis wire feed are shown in Figure 23. The off-axis wire feed, in addition to its ease of implementation, offers simple implementation of auxiliary devices to

enhance the wire feed, such as ultrasonic transducers. A major challenge with wire feeding is ensuring the wire, which tends to curl due to residual stresses from the drawing process, feeds toward a precise location under the laser. Deflection in any direction can induce unstable melting conditions (e.g., stubbing, balling) or cause the wire to miss the melt pool entirely. The wire feed nozzle is also subject to intense thermal radiation from the laser reflections and melt pool emissions. This, combined with the abrasion of the metal wire, can prematurely wear the nozzle orifice.

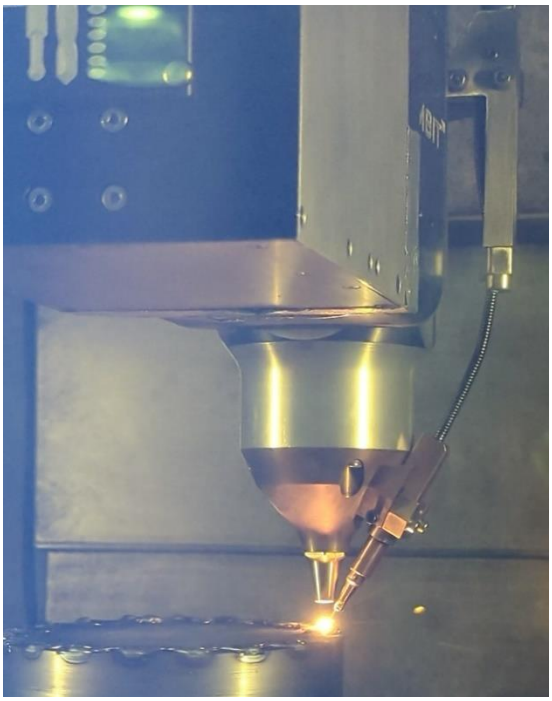

Figure 23. The AMBIT laser-wire DED head during deposition. The wire is delivered off-axis on the right side of the melt pool.

Based on the defined constraints the following requirements were reached for an ultrasonic wire-feed nozzle:

- The nozzle must maintain a precise wire position within the laser exposure region to maintain stable melting.
- The nozzle must resist melting and thermal distortion when under stable deposition conditions.
- The nozzle orifice must resist excess abrasion during the wire feeding process.

- The nozzle must impart ultrasonic (>20 kHz) oscillations to the wire which remain undamped at the precise melt pool position.

Because of the complex relationships between melt pool temperature, melt viscosity, and transmission depth, the minimum amplification distance was left as an unspecified experimental variable.

To fulfill the above requirements, a piezoelectric actuator was mounted within a custom wire-feed nozzle to impart linear oscillation to a sheath which directed the wire toward the melt pool. The design, illustrated in Figure 24, amplifies the minute strain of the piezo at a ratio of 5:1 at the approximate location of the melt pool. The selected piezo actuator (PA2JE) was purchased from Thorlabs (Newton, NJ, USA), and the relevant details are shown in Table 8. A spring, mounted coaxially with the piezo actuation axis, provided a load to assist in returning the piezo to its unstressed length during operation. The vibrating sheath was cut from stainless steel capillary tubing and provides excellent abrasion and thermal resistance. The sheath also allows for precise alignment of the wire within the laser spot. These attributes are particularly important for the orifice near the melt pool.

PA2JE Piezoelectric Chip Details

Dimensions	3.0 mm × 3.0 mm × 2.0 mm
Resonant Frequency	450 kHz
Max. Displacement at 75 V (No load)	2.0 µm ± 15%
Required load for max. displacement	144 N (32 lbs)

Table 8. Details of the piezoelectric chip selected for generating ultrasonic motion.

The piezo was driven by a square waveform and a custom amplifier circuit. The field effect transistor (FET) circuit supplied 44 V direct current to the piezo at a frequency dictated by the waveform generator.

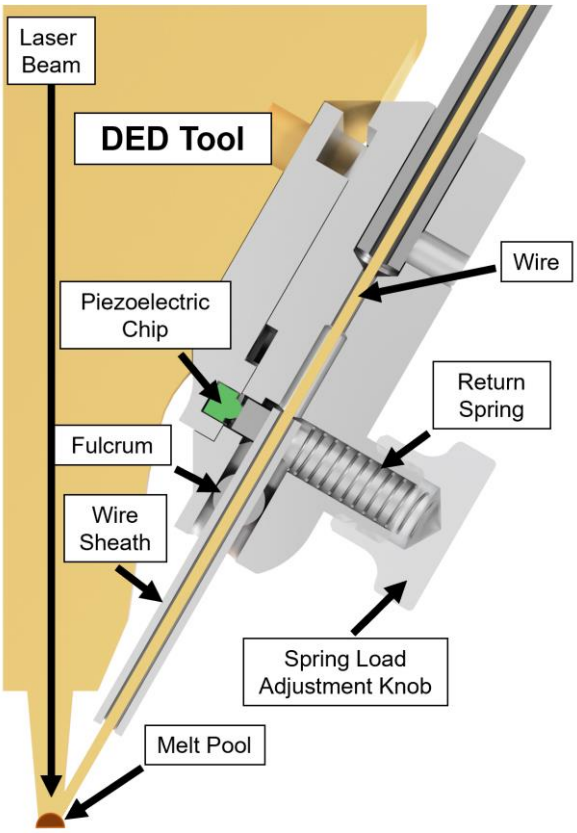

Figure 24. A cross-section schematic of the ultrasonic wire feed nozzle mounted on a representative DED laser tool.

3. Methodology

3.1 Materials

Stainless Steel 316L (SS316L) wire (Ø=1.1 mm) was selected for the feedstock material. Mild steel and stainless steel plates were used as substrates for single track and wall geometries, respectively. Stainless steel provides excellent strength and corrosion resistance, while mild steel is inexpensive and easy to machine. Both alloys show excellent weldability and are well suited within agricultural and transportation sectors.

3.2 Deposition

Maintaining stable deposition conditions is a key requirement for melt pool vibration to be effective. Any instances of stubbing or balling at the melt pool would disrupt the vibration mechanics at the end of the wire. Previous experimentation determined that stable melting occurs at a laser power of 1,500 W, a scanning speed of 500 mm/min, and a wire feed rate of 900 mm/min. Shielding gas flow rate was kept at 3 L/min to maintain a stable flow field around the melt pool and prevent excessive oxidation.

Off-axis wire feed also contributes to direction-dependent melt pool stability. Because of this, single tracks were printed in the -X and +Y direction. Walls were printed as one continuous track along the +Y and -Y directions, alternating Y direction as each layer was deposited. Vibration was conducted at a variety of frequencies. Control samples were produced without vibration and are labeled as '0 Hz' samples throughout the text.

3.3 Characterization

Several methods of capturing the process outcomes from vibration-assisted DED were employed. Off-axis high-speed imaging was performed using an Edgertronic SC2+ high-speed camera (Campbell, CA, USA). This imaging is well suited for capturing transient melt pool behavior and morphology during deposition. The orientation of the camera with respect to the melt pool is shown in Figure 25. All images were gathered at 13,000 frames per second. Microstructure was gathered from cross-section of track and wall samples. Samples were sectioned, cold mounted in epoxy, ground, and polished up to 1 μm using a diamond suspension. Mounted samples were electrolytically etched at 3V for several minutes in a solution of 56 g KOH and 100 mL deionized water. Optical microscopy was performed on etched samples. Computed tomography (CT) was also performed to unveil any variation in porosity between vibration conditions. CT scanning was performed on epoxy-mounted wall sections. Viewing and porosity analysis was performed using VGStudio MAX from Volume Graphics, Inc. (Charlotte, NC, USA).

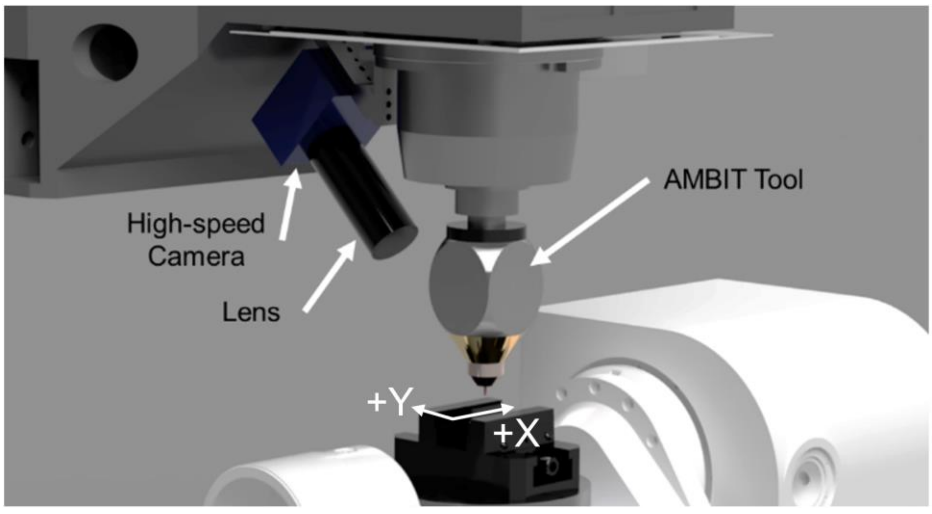

Figure 25. The off-axis high-speed camera mounted in the build chamber and aimed at the melt pool.

4. Results

4.1 High-speed Melt Pool Imaging

Collections of high-speed images are shown in Figure 25 and Figure 26. At low frequencies (<6,000 Hz), the wire displacement is obvious. A bright halo surrounds the solid wire at the interface between the wire and melt pool. This halo geometry is an excellent indicator of the wire position and cavitation driven by the oscillatory wire motion. At higher frequencies (>13,000 Hz), the vibration frequencies surpass the frame rate of the camera and are not directly visible. Amplitude was observed to also depend on frequency, with lower frequencies generating displacement up to 75 µm. At all frequencies, the amplitude of vibration remained sufficiently low to prevent liquid atomization, spatter ejection, and melt pool instability.

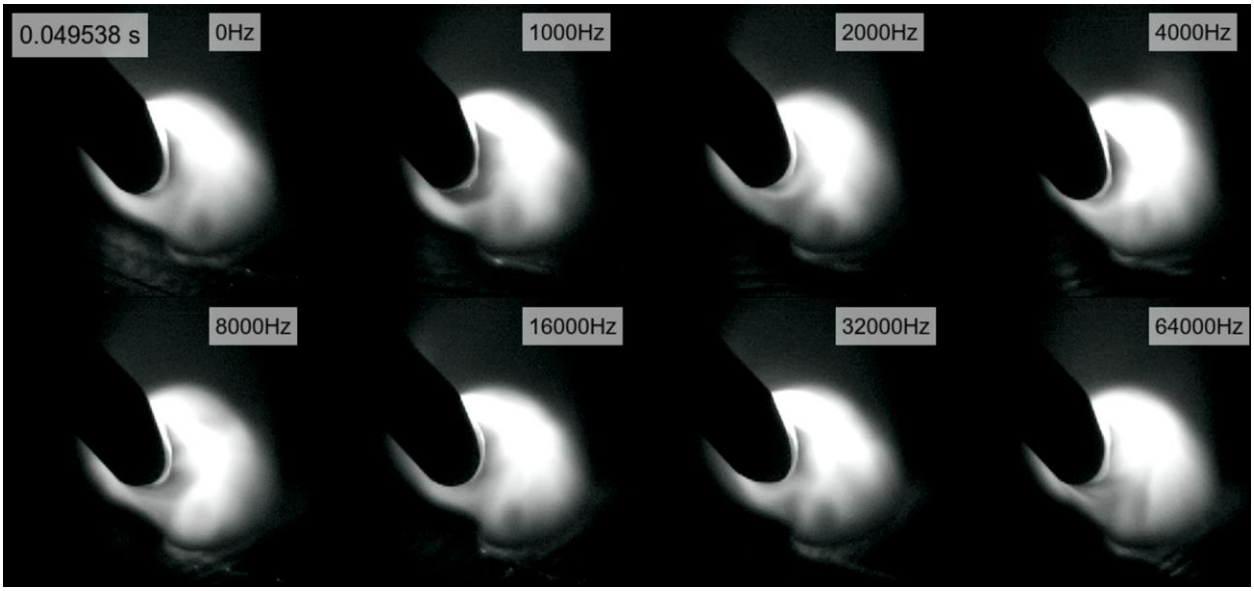

Figure 26. High-speed melt pool images of deposition at a variety of vibration frequencies. The movement direction is toward the camera. Accompanying videos are provided in the online version of the text.

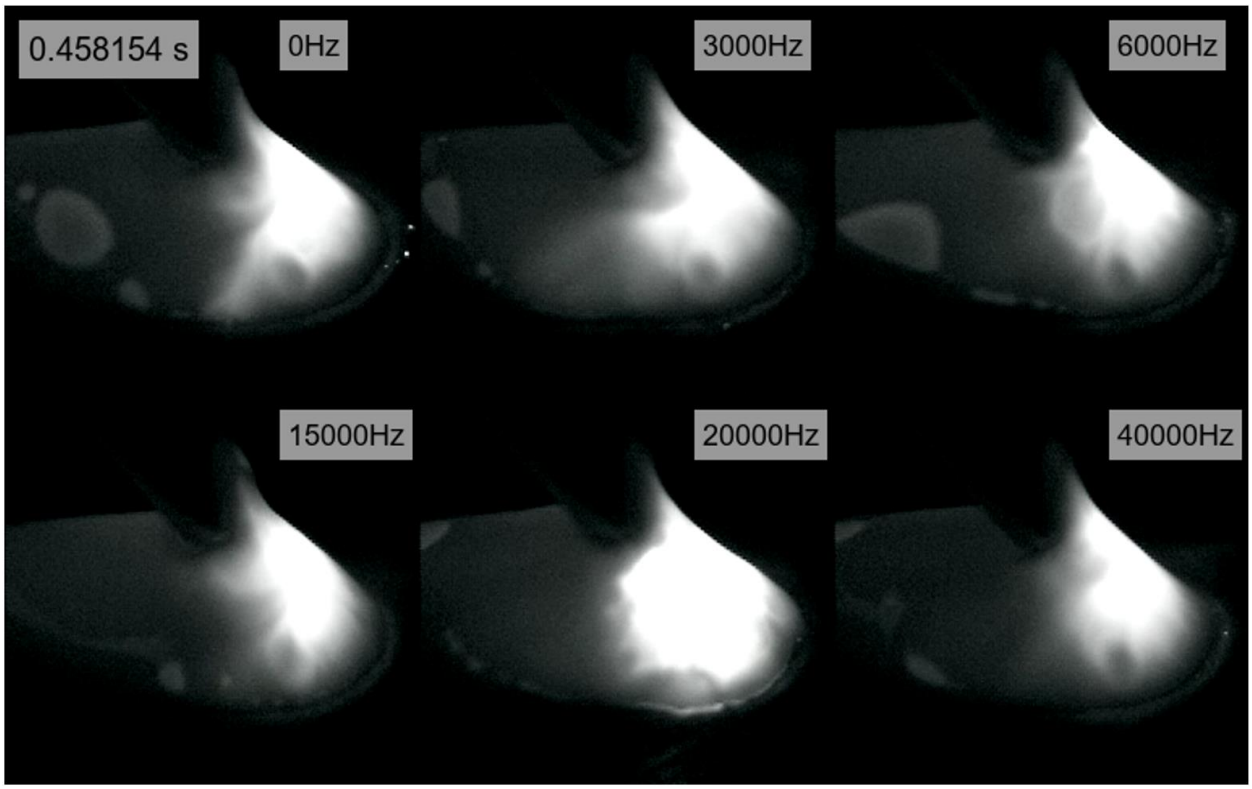

Figure 27. Melt pool imaging at different vibration frequencies. The melt pool is traveling toward the right in the image, i.e., away from the wire insertion side. Accompanying videos are provided in the online version of the text.

The direct effect of melt pool vibration is not immediately apparent in high-speed imaging. However, artifacts within the melt pool provide a nuanced understanding of the melt pool mechanics from sonic and ultrasonic oscillation. A crucial artifact is the wettability between the solid wire and liquid alloy. Figure 28 shows the variation in wettability with and without ultrasonic vibration. Without vibration, the molten liquid is repeatedly drawn up the wire due to surface tension. This force, acting against the constant force of gravity, creates an oscillating droplet along the wire. At 20,000 Hz, this transient behavior is not observed. This is effectively explained by the wettability and contact angle of a liquid under mechanical vibration. Wettability of a droplet is traditionally described as a relationship between the contact angle (θ) and the solid-gas (γ_{SG}), solid-liquid (γ_{SL}), and liquid-gas (γ_{LG}) surface free energies via Young's equation [138]–[140]:

$$\gamma_{SG} = \gamma_{SL} + \gamma_{LG} \cos\theta \tag{5.1}$$

Figure 28(d) depicts these variables in the context of wire-fed laser DED. The relationship between vibration within liquid media and the solid-surface contact angle has been established experimentally [141]. The contact angle, determined by the balance between adhesive and cohesive forces in a liquid-solid interaction, holds an inverse relationship with vibrational peak velocity. Physically, this is a consequence of the surface energy reduction caused by liquid cavitation. Eq. (1) holds that as γ_{LG} decreases and the remaining surface energies (γ_{SG}, γ_{SL}) remain constant, the contact angle (θ) must also decrease. This relationship remains true for contact angles less than 90 degrees. The decrease in contact angle plays a key role in wire-fed DED. As the material melts and surface tension begins to form a droplet, the lower contact angle effectively lowers the adhesive force along the wire, improving the transmission of liquid media from the wire into the melt pool.

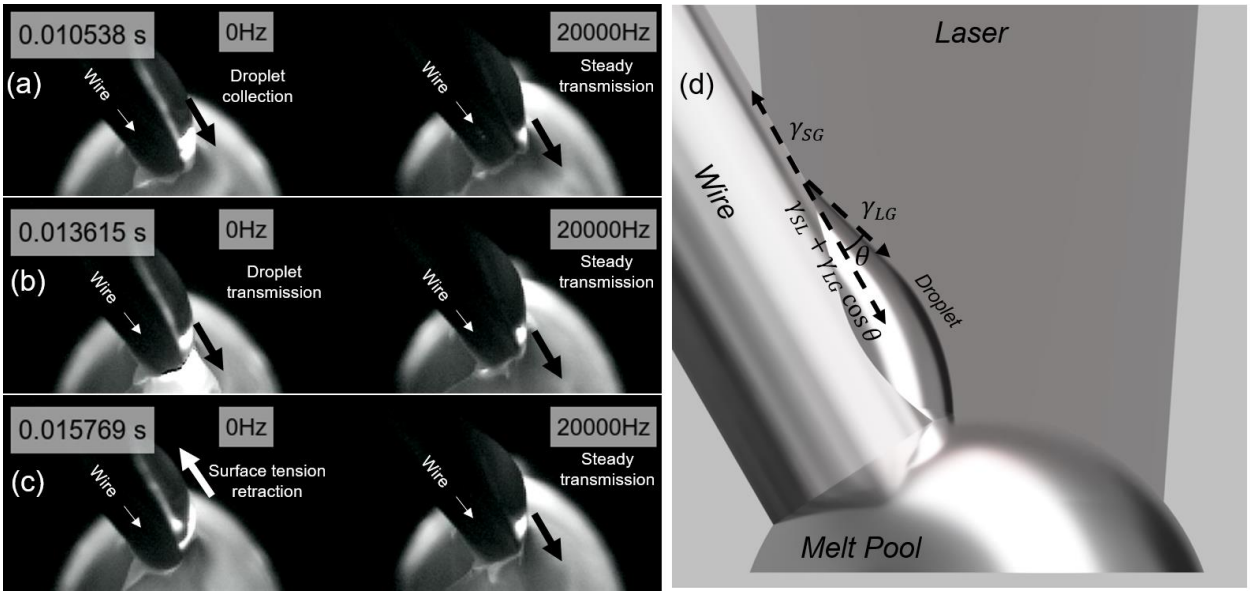

Figure 28. (a-c) High-speed images of wire transmission with and without ultrasonic vibration over time. (d) Depiction of the contact angle (θ) and wire-gas (γ_{SG}), wire-droplet (γ_{SL}), and droplet-gas (γ_{LG}) surface energy interactions at the wire insertion point.

Another vibration artifact is the formation and disruption of the oxide growth on the tail of the melt pool. Residual oxygen in the shielding atmosphere and on the wire and substrate surfaces quickly forms oxides during the solidification stage. Because of the thermal gradients within the melt pool, Marangoni flow initiates vortices in the melt pool tail which are visible in the movement of the discrete oxide regions (Figure 29). Ultrasonic wire vibrations were observed to catalyze a dispersion of the oxide

regions near the wire insertion location. Oxides, floating toward the wire due to Marangoni flow, break apart and are pushed further along the melt pool tail. Without vibration, the oxide region remains intact and is pushed toward the substrate/melt pool interface. This oxide dispersion behavior appears to be dependent on the frequency/amplitude relationship. At 15 kHz, the dispersion can be observed considerably farther from the wire insertion point than at 20 kHz. This likely reflects deeper transmission of the waves, a consequence of higher oscillation magnitude.

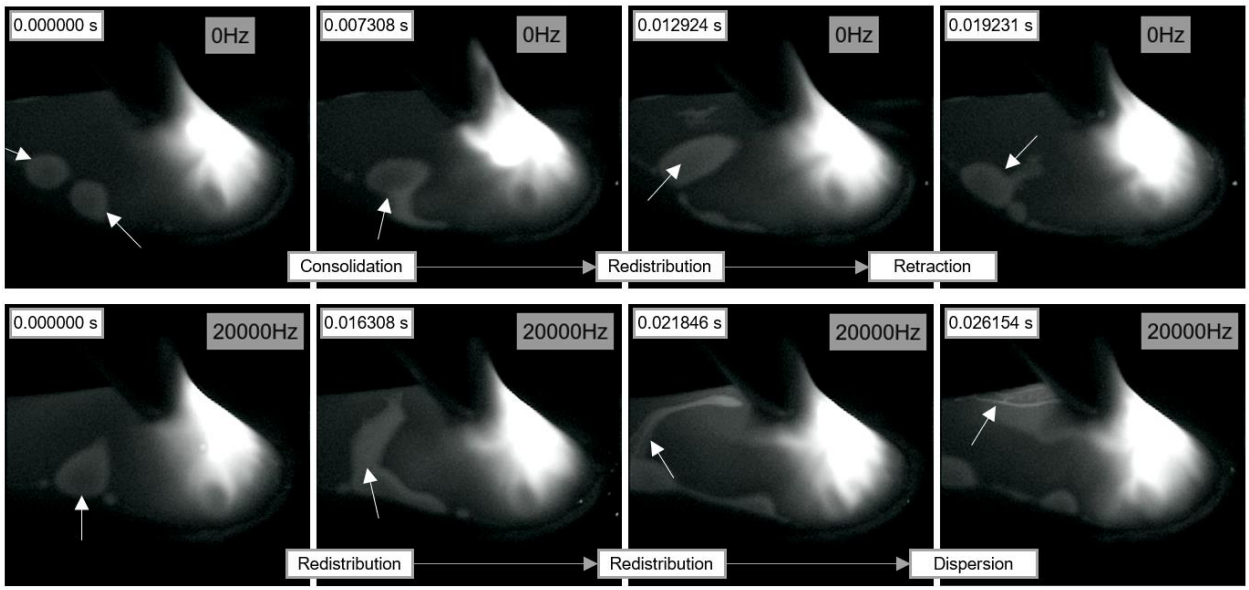

Figure 29. Flow and dispersion of discrete oxide regions on the solidifying melt pool without and with ultrasonic wire vibration. The build direction, i.e., melt pool motion, is toward the right side of the frame in these images. Accompanying videos are included in the online version of this text.

4.2 Microstructure

Sample microstructures, shown in Figure 30, featured columnar and cellular subgrains within macro-grains, typical of additively manufactured SS316L [142], [143]. These subgrains, ranging from 2-5 μm in size, are a consequence of the rapid solidification and elemental segregation [144]. Limited diffusion of Cr and Mo within the Fe-Ni melt creates Cr-Mo enrichment between austenite grains and formation of intergranular δ-ferrite. In both structures, grains are elongated and pointed toward the top of each melt track. Heterogeneous solidification theory dictates that grain nucleation will begin on solid surfaces and grain growth will primarily occur in the direction of heat flux. In DED, the solid-liquid boundary at the bottom of the dilution zone is the catalyst for grain formation. The heat flux points toward

the top of the melt pool and along the direction of travel of the laser, which is why columnar grain growth is vertical at the dilution zone and is assumed horizontal, i.e., normal to the cross section view, near the top of the melt track.

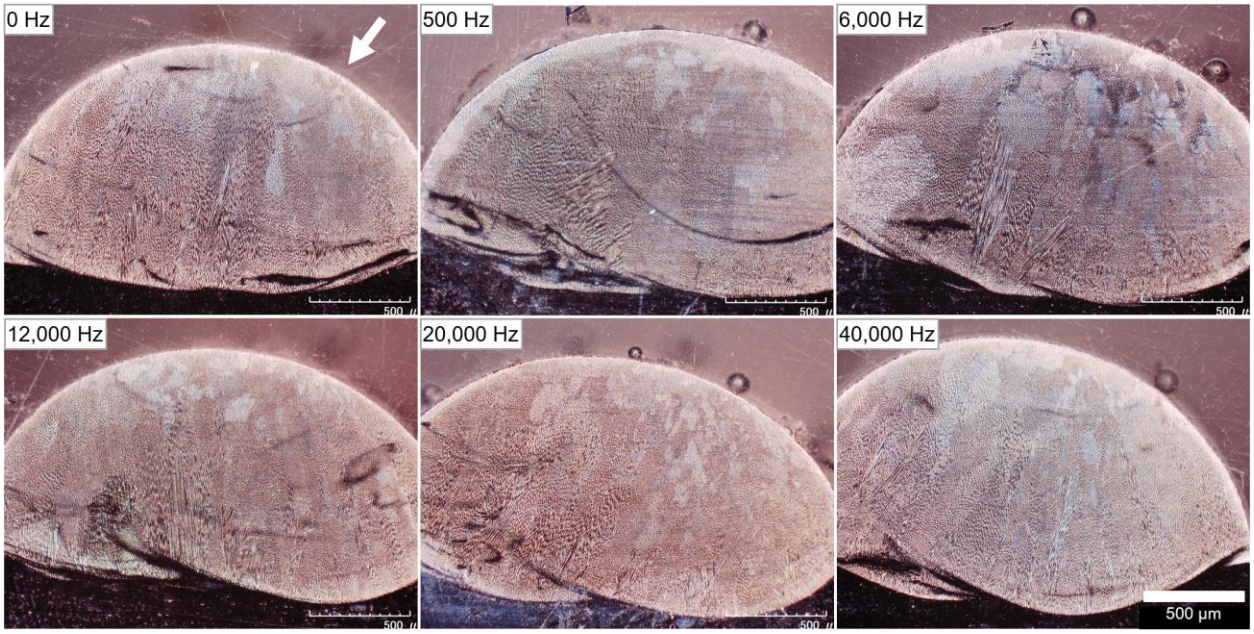

Figure 30. Cross section view of tracks produced without and with vibration assistance at a variety of frequencies. The white arrow indicates the approximate direction and location of the wire during deposition.

Visible in Figure 31, grains were refined using vibration assistance. Columnar grains 500-800 µm in length with elongated subgrains in the 0 Hz sample were notably absent in the 20 kHz sample. Instead, oblong acicular grains with short columnar or cellular subgrains comprised the bulk of the deposited track microstructure. It is well established that ultrasonic assistance lowers the columnar-to-equiaxed transition threshold in stainless steels [91], [128]. This attribute is notable in the microstructure of wall samples (Figure 32). While columnar dendrites spanning multiple layers are found with and without ultrasonic vibration, there is a notable difference in grain morphology between conditions. Samples produced with 20 kHz vibration show uniform cellular and short dendritic grains through the bulk of the wall. Without vibrational assistance, columnar grains are prominently found throughout the deposited layers. Current theory suggests that cavitation and melt pool turbulence disrupt the diffusion process at the solidification front, leading to fracture and redistribution of solid dendrites within the melt [91], [126]. Former dendrites either diffuse into the liquid state or behave as nucleation sites within the melt. The reformation of

dendrites within the molten metal is commonly believed to encourage changes in grain morphology and direction. It has also been speculated that there is a threshold energy for obtaining uniform grain refinement [132], [145]. With the columnar grains spanning multiple layers with and without ultrasonic vibration, it is clear the applied energy was not sufficient for complete grain refinement. The observed outcomes complement experimental findings from ultrasonic-assisted fusion welding and deposition literature [124], [128], [134].

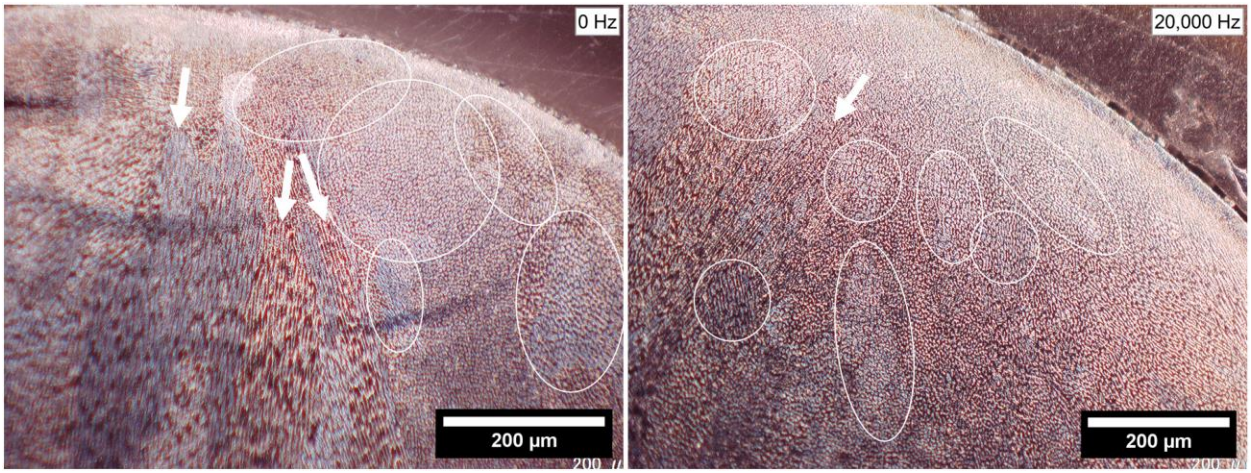

Figure 31. Grain refinement observed between tracks produced without vibration and with 20 kHz vibration. Cellular grains are circled, and columnar grains are marked with arrows.

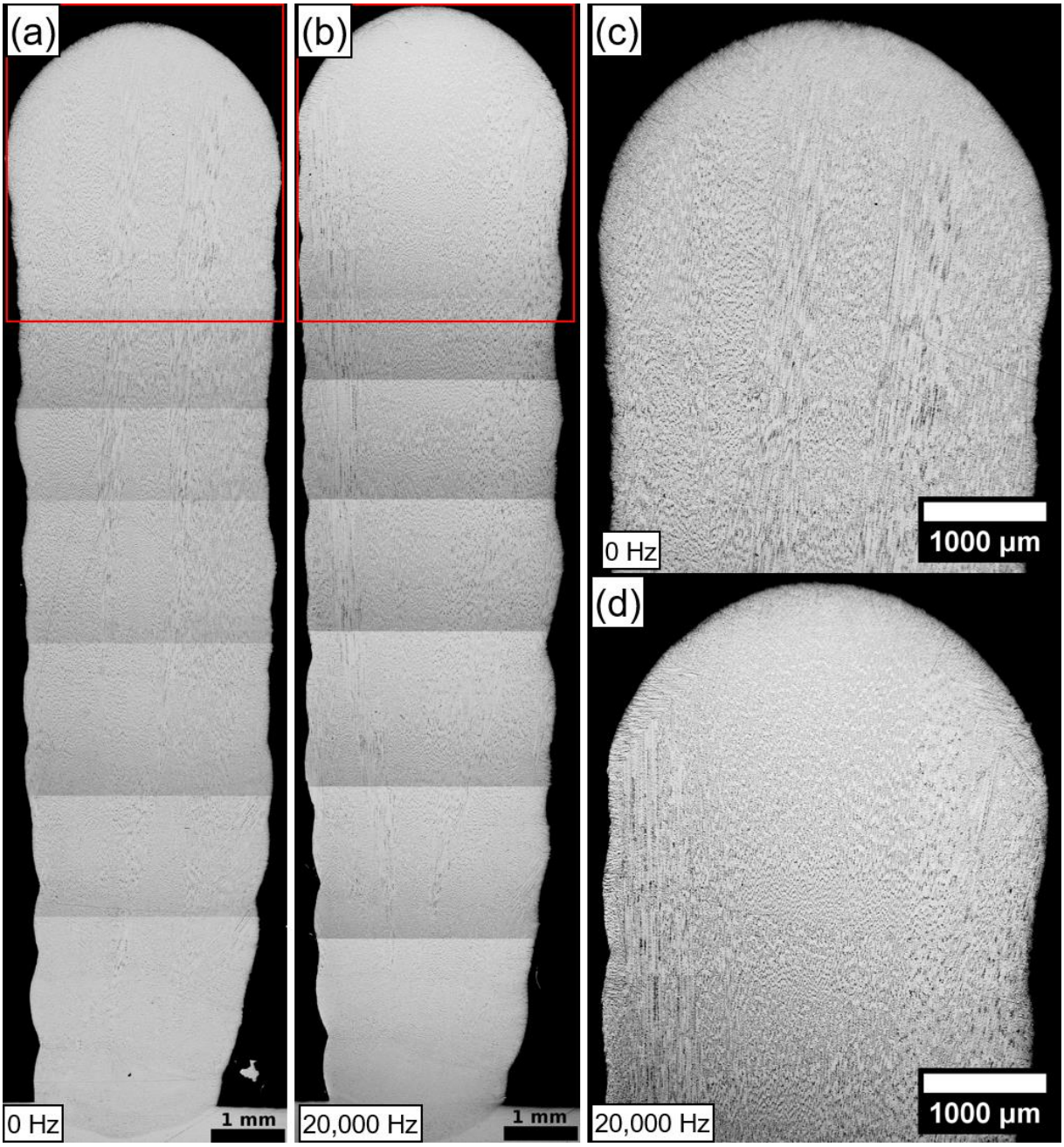

Figure 32. Microstructures in walls produced without (a, c) and with (b, d) 20 kHz ultrasonic vibration. The boxes mark the locations of images (c) and (d).

4.3 Porosity Analysis

CT scans were used to compare porosity levels in three wall samples: no vibration, 3 kHz vibration, and 20 kHz vibration (Figure 33). The interior region was selected and analyzed for voids. In all samples, no obvious pores were noted. No major differences were identified between samples produced with and without vibration assistance. This is largely in part to the stability generated by the

selected process parameters. As seen in the high-speed images, all samples formed stable melt tracks which remained consistently stable throughout deposition. The stable melt produced in these samples resisted lack of fusion, keyhole porosity, gas-generated porosity, and solidification fractures. In material combinations or parameter selections that are prone to porosity formation, vibration is typically expected to mitigate pore formation [95].

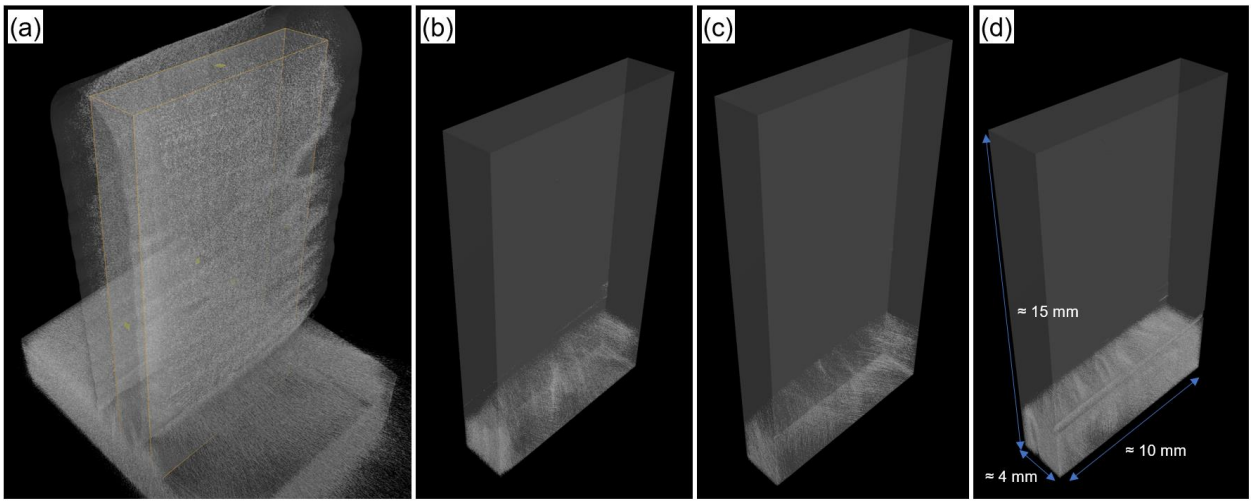

Figure 33. CT scans of walls produced with (b) no vibration, (c) 3 kHz vibration, and (d) 20 kHz vibration. (a) shows a representation of the boxed interior region used for the slices in (b)-(d).

5. Discussion

The vibration system described herein can be described as a driven, damped oscillating system. The position of the wire oscillation at the piezo contact point (Figure 34) is provided in Eq. 2:

$$x(t) = c_1 e^{At} + c_2 e^{Bt} + \frac{F_0}{m\omega_0^2} + C\cos\omega_d t + D\sin\omega_d t \tag{5.2}$$

$$A = -\gamma/2 + \sqrt{\gamma^2/4 - \omega_0^2} \tag{5.2.1}$$

$$B = -\gamma/2 - \sqrt{\gamma^2/4 - \omega_0^2} \tag{5.2.2}$$

$$C = \frac{F_0}{m(\omega_0^2 - \omega_d^2)}\left[1 - \frac{\gamma^2\omega_d^2}{(\omega_0^2 - \omega_d^2)^2 + \gamma^2\omega_d^2}\right] \tag{5.2.3}$$

$$D = \frac{F_0\gamma\omega_d}{m[(\omega_0^2 - \omega_d^2)^2 + \gamma^2\omega_d^2]} \tag{5.2.4}$$

The motion is defined in terms of the driving force (F_0) and frequency (ω_d) of the piezo, the inertial mass (m) and natural frequency of the system (ω_0), coefficients (c_1) and (c_2), and the damping coefficient (γ) provided by friction and fluid resistance in the melt pool. This relationship relies on several assumptions: the wire position remains fixed to the sheath during oscillation; the rotational motion about the fulcrum is sufficiently small to approximate linear motion; a small damping coefficient is assumed for underdamped motion; and gravity is neglected. A full derivation of the system dynamics is provided in Appendix C: Derivation of the Nozzle Motion Equation.

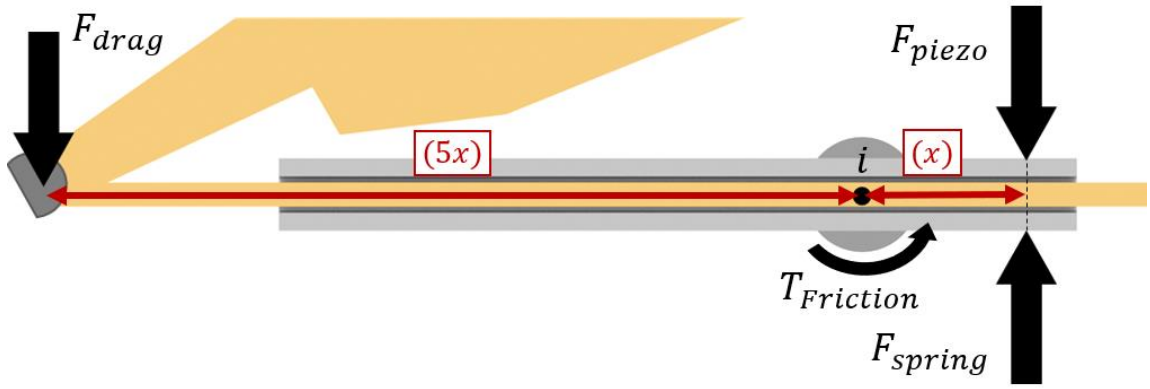

Figure 34. A kinetic representation of the ultrasonic wire feed nozzle. The forces and torque acting on the nozzle affect the natural frequency (ω_0) and damping coefficient (γ).

The amplitude of the vibration is primarily dictated by the ratio between the driving frequency and the natural frequency of the vibration system [146], [147]. As this ratio approaches 1, i.e., the driving frequency matches the natural frequency, constructive interference dominates and the amplitude reaches a global maximum. Tuning the vibration system to a specific operating frequency that maximizes the amplitude is crucial, especially when considering the minute displacements of the piezoelectric actuator. Details of the vibration tuning process are provided in Appendix D: Tuning and Verification of the Piezo Vibration. While there is no established literature expanding upon the displacement required for grain refinement and porosity reduction, there is a visible effect of amplitude on the wave transmission depth seen in high-speed images.

Although the physical phenomena of vibration-assistance during solidification have been outlined extensively through welding and AM literature, few works have supported theoretical phenomena with in-

situ imaging [129], [136]. Traditional theory suggests cavitation and acoustic streaming in the liquid pool cause fragmentation and dispersion of solid dendrites, leading to improved nucleation near the solidification front [91], [133], [148]. While observation of the solidification front using visible light is not possible, high-speed images presented evidence of cavitation and acoustic streaming via disruption of oxide formation as shown in Figure 27. Building onto the theory presented by Cong and Ning [91], direct melt agitation using the filler wire adds a mechanical component to the fluid forces. As shown in Figure 28, the stirring action assists with metal transfer into the melt pool by lowering the surface tension and contact angle of the wire as it melts. The improved wettability serves to expand the window of acceptable process parameters that prevent liquid balling on the wire.

An important consideration in the application of this methodology is the sensitivity of the wire position relative to the melt pool. Given that the resonant frequency of the actuator depends on the oscillating load, the fluid drag on the wire will affect the resonant frequency. The piezoelectric chip is designed for considerably higher loads; thus, this issue was avoided. However, if the wire contacts the solid boundary at the bottom of the melt pool, i.e., during stubbing, the vibration is completely damped, effectively minimizing the metallurgical benefits of vibration assistance. Methods of sensing to avoid stubbing would eliminate these issues.

6. Conclusions

Design and implementation of a geometry-independent, ultrasonic-assisted, laser-wire deposition system is presented. In-situ observations and structural outcomes for this novel technique are gathered:

- Wire vibration serves to mechanically-stir the melt pool, inducing cavitation and acoustic streaming directly within the liquid alloy and improving metal transfer from the wire to the melt pool.
- Frequency-amplitude relationships play a key role in determining the level of cavitation seen during deposition with higher amplitudes inducing deeper transmission within the melt.
- Grain refinement and a columnar-to-equiaxed transition is noted in ultrasonic-assisted single track and wall geometries.

- Computed tomography confirms that all deposition strategies avoided porosity formation, indicating stability in the material and process parameter combinations.

This work provides a basis for obtaining uniform structural outcomes in laser-wire DED. Additional work should focus on unveiling frequency-amplitude-outcome relationships and expanding the regime of vibrational kinetics.

Acknowledgements

The authors would like to thank A.R. Cardinali for their input into the design of the vibration system.

Funding

This paper received no funding for the conceptualization, research, and outcomes for the results.

Competing Interests

The authors have no competing interests to report.

Chapter 6 – Conclusions

6.1 Summary

Cast iron remains a popular material in agricultural, transportation, and manufacturing sectors for many reasons. The ancillary processing modes studied herein proved successful in expanding the window of acceptable process parameters for laser-based DED. While stainless steel has proven to be an effective cladding material for cast iron remanufacturing under specific temperature conditions, the elemental composition of the stainless steel and cast iron melt pool is not amenable to rapid solidification processes. Ni-based filler material, specifically Inconel 625, showed success in being able to repair gray cast iron to 86% of the original tensile strength without preheating or annealing. This was in large part due to the low Cr content in Inconel 625 alloy, leading to a preferential formation of austenite in the fusion zone rather than martensite. Inconel also provided superior mixing of base and filler materials, allowing for a gradient zone between the two materials. Careful control of these aspects ensures the dissimilar materials are amenable to laser-based remanufacturing.

The use of wire feeding also improved the outcomes in laser DED remanufacturing of cast iron. The primary advantage in wire feeding is the distinct melt pool morphology caused by continuous material insertion. There are two primary shape attributes that were observed to have beneficial effects: 1) the interaction between the laser and wire above the substrate, and 2) the surface tension effect pulling the melt pool against gravity. Because the wire is a continuous material, insertion into the laser path occludes the substrate from receiving high-intensity laser exposure. This prevents martensite formation and porosity generation. The benefit of this is obvious when comparing transient melt pool signatures. Melt pools in powder-laser DED undergo rapid growth and shrinkage as CO and CO_2 gases attempt to escape the melt pool. This results in discrete spikes in the melt pool size that are notably absent from comparable wire feed parameters. The latter benefit, the upward force of surface tension, helps to draw heat further from the gray cast iron. The molten metal at the end of the wire is naturally pulled upward as surface tension forms a droplet at the end of the wire. This upward pull maintains a taller deposition track with

low dilution, an ideal scenario for preventing gas generation and martensite formation in gray-cast iron remanufacturing.

Lastly, a pilot study showed feasibility for a geometry-agnostic, ultrasonic melt pool vibration nozzle for laser-wire DED. In-situ high-speed images provided a better understanding of the effects of melt pool vibration and the wire dynamics under harmonic motion. Outcomes in single-track and wall samples proved the effectiveness of ultrasonic melt pool vibration on refining and unifying the microstructures in as-printed stainless steel. The detailed design unlocks physical and geometrical limitations of current technology by removing the component volume as a vibration transmission medium. Few additive manufacturing processes can achieve fully dense, heterogeneous material properties, and this work builds toward that goal for wire-laser DED.

6.2 Future Work

This work, although it may have answered many questions, opened a plethora of additional questions of varying levels of difficulty and importance. In the context of wire DED, there is a considerable gap in our understanding of off-axis wire feed systems and how to maintain stable melting under different process disruptions (over-building, under-building, wire misalignment, etc.). Considerable process development is needed to transition wire-laser DED to a robust technology well suited for large components, repairs and remanufacturing, and process/part qualification. Likewise, very little is published about how shielding gas coverage in both powder and wire DED can affect the material properties and process integrity. Gas escapement events driven by oxygen contamination proved detrimental to the quality of powder-based remanufacturing. Tools like computational fluid dynamics simulations and Schlieren imaging are incredibly valuable in pursuit of a wholistic process understanding.

Other areas that are promising for the future are integration and feedback of sensor data within the build chamber. High-speed imaging is invaluable in providing a qualitative understanding of the melt pool physics under unique conditions. In-process non-destructive evaluation (NDE) is also an attractive approach, supplying direct structural quality information without physical modification to the existing structure. However, automated data collection and rapid decision making are required to generate

feedback about process stability. Of course, the robustness of the process design takes precedence in the order of importance, but reliable control mechanisms are needed to ensure any additive manufacturing process can withstand deviations during a build cycle.

There are many residual questions regarding the ultrasonic melt pool vibration system. There is very little information on requisite peak velocity to induce cavitation and acoustic streaming in a material, especially for a transient thermal process like DED. Similarly, the requisite vibration kinetics for inducing microstructural changes is not fully understood. On the macro-scale, this work left the structural outcomes of vibration assistance unanswered. With improved microstructural homogeneity, one would expect an improvement in isotropic strength, a serious limitation in both PBF and DED processes. In the context of dissimilar material repair, the additional cavitation is expected to improve elemental redistribution and residual stresses. Interfacial gradients of Fe and Ni proved successful at improving the bonding and reducing the structural disparities between GCI and the filler material in Chapter 3. Residual stress reduction is also ideal, as the stresses formed during solidification are a key factor in the interface fracture potential during solidification and cyclic loading.

From a process design standpoint, open questions remain. Oscillations were only studied in one direction. Oscillation around two or more axes adds complexity that could provide additional process benefits and robustness. One example would be tailoring the oscillation at specific locations within a part to obtain specific mechanical behavior. Akin to how a designer would orient fibers in a continuous fiber composite along the loading direction, one could preferentially orient columnar structures in uniaxial stressed areas and induce equiaxed grain structures in coaxial stressed areas. The same philosophy could be applied with residual stresses as with steel rebar reinforcement in concrete. If ultrasonic-assisted vibration can adequately modify the localized residual stress state, a process designer could apply vibration assistance preferentially to prestress surfaces expected to undergo cyclic tension.

DED remains a nascent technology with incredible flexibility owing to the coupled delivery of unspecified material and energy sources. Applications of arc plasma and high-carbon wire, for example, could be well suited for localized hardfacing. Implementations of laser and copper wire are fit for creating

sensors for structural health monitoring. Powder deposition for compositionally graded titanium would unlock design capabilities in aerospace and transportation and reduce end-use energy and emissions in aircraft and ground transportation. Creation of lattice structures also builds toward this goal, and DED has potential for both open- and closed-cell structures. Combining any of the above applications, e.g., compositionally graded lattice structures or load-monitoring hardfacing, is a) beyond exciting, b) incredibly useful, and c) near impossible with current manufacturing platforms. Considerable development is needed to get to these end goals, but DED technology has the potential. The multidisciplinary aspect of the process offers challenges for many areas: experimental, simulation, computation, controls, material science, physics, etc. As an engineer, I am excited and honored to be working alongside many bright scholars to create and transition these new technologies into practice.

References

[1] U.S EPA, "Inventory of U.S Greenhouse Gas Emissions and Sinks. EPA 430-R-21-005," *Environmental Protection Agency*, pp. 1689–1699, 2021.

[2] R. Steinhilper, "Recent trends and benefits of remanufacturing: From closed loop businesses to synergetic networks," *Proceedings - 2nd International Symposium on Environmentally Conscious Design and Inverse Manufacturing*, pp. 481–488, 2001, doi: 10.1109/ECODIM.2001.992404.

[3] H. Vasudevan, V. Kalamkar, and R. Terkar, "Remanufacturing for Sustainable Development: Key Challenges, Elements, and Benefits," *International Journal of Innovation, Management and Technology*, vol. 3, no. 1, pp. 84–89, 2012.

[4] H. Gunasekara, J. Gamage, and H. Punchihewa, "Remanufacture for sustainability: Barriers and solutions to promote automotive remanufacturing," *Procedia Manufacturing*, vol. 43, no. 2019, pp. 606–613, 2020, doi: 10.1016/j.promfg.2020.02.146.

[5] N. Nasr and M. Thurston, "Remanufacturing: A key enabler to sustainable product systems," *Proceedings of the 13th CIRP International Conference on Life Cycle Engineering, LCE 2006*, pp. 15–18, 2006.

[6] T. Roy *et al.*, "Evaluation of the mechanical properties of laser cladded hypereutectoid steel rails," *Wear*, vol. 432–433, no. January, p. 202930, 2019, doi: 10.1016/j.wear.2019.202930.

[7] B. Baufeld, E. Brandl, and O. Van Der Biest, "Wire based additive layer manufacturing: Comparison of microstructure and mechanical properties of Ti-6Al-4V components fabricated by laser-beam deposition and shaped metal deposition," *Journal of Materials Processing Technology*, vol. 211, no. 6, pp. 1146–1158, 2011, doi: 10.1016/j.jmatprotec.2011.01.018.

[8] E. Toyserkani, A. Khajepour, and S. F. Corbin, "Laser Cladding," Aug. 2004, doi: 10.1201/9781420039177.

[9] W. J. Sames, F. A. List, S. Pannala, R. R. Dehoff, and S. S. Babu, "The metallurgy and processing science of metal additive manufacturing," *International Materials Reviews*, vol. 61, no. 5, pp. 315–360, 2016, doi: 10.1080/09506608.2015.1116649.

[10] J. J. Lewandowski and M. Seifi, "Metal Additive Manufacturing: A Review of Mechanical Properties," *Annual Review of Materials Research*, vol. 46, no. 1, pp. 151–186, 2016, doi: 10.1146/annurev-matsci-070115-032024.

[11] Z. Wang, T. A. Palmer, and A. M. Beese, "Effect of processing parameters on microstructure and tensile properties of austenitic stainless steel 304L made by directed energy deposition additive manufacturing," *Acta Materialia*, vol. 110, pp. 226–235, 2016, doi: 10.1016/j.actamat.2016.03.019.

[12] Z. Wang, E. Denlinger, P. Michaleris, A. D. Stoica, D. Ma, and A. M. Beese, "Residual stress mapping in Inconel 625 fabricated through additive manufacturing: Method for neutron diffraction measurements to validate thermomechanical model predictions," *Materials and Design*, vol. 113, pp. 169–177, Jan. 2017, doi: 10.1016/j.matdes.2016.10.003.

[13] B. E. Carroll, T. A. Palmer, and A. M. Beese, "Anisotropic tensile behavior of Ti-6Al-4V components fabricated with directed energy deposition additive manufacturing," *Acta Materialia*, vol. 87, pp. 309–320, 2015, doi: 10.1016/j.actamat.2014.12.054.

[14] Z. E. Tan, J. H. L. Pang, J. Kaminski, and H. Pepin, "Characterisation of porosity, density, and microstructure of directed energy deposited stainless steel AISI 316L," *Additive Manufacturing*, vol. 25, pp. 286–296, Jan. 2019, doi: 10.1016/j.addma.2018.11.014.

[15] W. Woo, D. K. Kim, E. J. Kingston, V. Luzin, F. Salvemini, and M. R. Hill, "Effect of interlayers and scanning strategies on through-thickness residual stress distributions in additive manufactured ferritic-austenitic steel structure," *Materials Science and Engineering A*, vol. 744, pp. 618–629, Jan. 2019, doi: 10.1016/j.msea.2018.12.078.

[16] Y. Wang and J. Shi, "Microstructure and Properties of Inconel 718 Fabricated by Directed Energy Deposition with In-Situ Ultrasonic Impact Peening," *Metallurgical and Materials Transactions B: Process Metallurgy and Materials Processing Science*, vol. 50, no. 6, pp. 2815–2827, Dec. 2019, doi: 10.1007/s11663-019-01672-3.

[17] F. Sciammarella and B. Salehi Najafabadi, “Processing Parameter DOE for 316L Using Directed Energy Deposition,” *Journal of Manufacturing and Materials Processing*, vol. 2, no. 3, p. 61, 2018, doi: 10.3390/jmmp2030061.
[18] J. H. Yu, Y. S. Choi, D. S. Shim, and S. H. Park, “Repairing casting part using laser assisted additive metal-layer deposition and its mechanical properties,” *Optics and Laser Technology*, vol. 106, pp. 87–93, 2018, doi: 10.1016/j.optlastec.2018.04.007.
[19] V. Ocelík, U. de Oliveira, M. de Boer, and J. T. M. de Hosson, “Thick Co-based coating on cast iron by side laser cladding: Analysis of processing conditions and coating properties,” *Surface and Coatings Technology*, vol. 201, no. 12, pp. 5875–5883, 2007, doi: 10.1016/j.surfcoat.2006.10.044.
[20] F. Arias-González *et al.*, “Fiber laser cladding of nickel-based alloy on cast iron,” *Applied Surface Science*, vol. 374, pp. 197–205, 2016, doi: 10.1016/j.apsusc.2015.11.023.
[21] D. Nelson, “Effects of Residual Stress on Fatigue Crack Propagation,” in *Residual Stress Effects in Fatigue*, J. Throop and H. Reemsnyder, Eds., West Conshohocken, PA: ASTM International, 1982, pp. 172–194. doi: doi.org/10.1520/STP30104S.
[22] J. Zhang, X. Wang, S. Paddea, and X. Zhang, “Fatigue crack propagation behaviour in wire+arc additive manufactured Ti-6Al-4V: Effects of microstructure and residual stress,” *Materials and Design*, vol. 90, pp. 551–561, 2016, doi: 10.1016/j.matdes.2015.10.141.
[23] A. Saboori, G. Piscopo, M. Lai, A. Salmi, and S. Biamino, “An investigation on the effect of deposition pattern on the microstructure, mechanical properties and residual stress of 316L produced by Directed Energy Deposition,” *Materials Science and Engineering A*, vol. 780, Apr. 2020, doi: 10.1016/j.msea.2020.139179.
[24] X. Lu *et al.*, “Residual stress and distortion of rectangular and S-shaped Ti-6Al-4V parts by Directed Energy Deposition: Modelling and experimental calibration,” *Additive Manufacturing*, vol. 26, pp. 166–179, Mar. 2019, doi: 10.1016/j.addma.2019.02.001.
[25] C. R. D’Elia, M. R. Hill, M. E. Stender, and C. W. San Marchi, “Residual Stresses at Critical Locations in Additively-Manufactured Components,” in *Conference Proceedings of the Society for Experimental Mechanics Series*, Baldi Antonio, S. L. B. and Kramer, and P. Fabrice, and C. John, and B. Sven, and and H. Johan, Eds., Cham: Springer International Publishing, 2020, pp. 49–57. doi: 10.1007/978-3-030-30098-2_8.
[26] V. G. Efremenko, Y. G. Chabak, A. Lekatou, A. E. Karantzalis, and A. V. Efremenko, “High-Temperature Oxidation and Decarburization of 14.55 wt pct Cr-Cast Iron in Dry Air Atmosphere,” *Metallurgical and Materials Transactions A: Physical Metallurgy and Materials Science*, vol. 47, no. 4, pp. 1529–1543, 2016, doi: 10.1007/s11661-016-3336-7.
[27] Y. Li *et al.*, “Elimination of voids by laser remelting during laser cladding Ni based alloy on gray cast iron,” *Optics and Laser Technology*, vol. 112, no. August 2018, pp. 30–38, 2019, doi: 10.1016/j.optlastec.2018.10.055.
[28] Y. Li, X. Liu, S. Dong, X. Ren, S. Yan, and B. Xu, “Influence of laser power on interface characteristics and cracking behavior during laser remanufacturing of nodular cast iron,” *Engineering Failure Analysis*, vol. 122, no. January, p. 105226, 2021, doi: 10.1016/j.engfailanal.2021.105226.
[29] Y. Li, S. Dong, S. Yan, X. Liu, P. He, and B. Xu, “Microstructure evolution during laser cladding Fe-Cr alloy coatings on ductile cast iron,” *Optics and Laser Technology*, vol. 108, pp. 255–264, 2018, doi: 10.1016/j.optlastec.2018.07.004.
[30] S. Lee, J. Kim, D. S. Shim, S. H. Park, and Y. S. Choi, “Micro-Cracking in Medium-Carbon Steel Layers Additively Deposited on Gray Cast Iron Using Directed Energy Deposition,” *Metals and Materials International*, 2020, doi: 10.1007/s12540-019-00589-5.
[31] S. Da Sun *et al.*, “Effect of laser clad repair on the fatigue behaviour of ultra-high strength AISI 4340 steel,” *Materials Science and Engineering A*, vol. 606, pp. 46–57, 2014, doi: 10.1016/j.msea.2014.03.077.
[32] S. D. Sun, D. Fabijanic, M. Leary, S. C. Gallo, I. Fordyce, and M. Easton, “The effect of pre-heat temperature on the microstructure and abrasive wear properties of laser metal deposited near-

eutectic The effect of pre-heat temperature on the microstructure and abrasive wear properties of laser metal deposited near-eutectic Fe-28,” vol. 032008, 2020, doi: 10.2351/7.0000116.
[33] Y. Li *et al.*, “Microstructure characteristics and mechanical properties of new-type FeNiCr laser cladding alloy coating on nodular cast iron,” *Journal of Materials Processing Technology*, vol. 269, no. August 2018, pp. 163–171, 2019, doi: 10.1016/j.jmatprotec.2019.02.010.
[34] J. Yu *et al.*, “Influence of laser deposition patterns on part distortion, interior quality and mechanical properties by laser solid forming (LSF),” *Materials Science and Engineering A*, vol. 528, no. 3, pp. 1094–1104, 2011, doi: 10.1016/j.msea.2010.09.078.
[35] A. R. Nassar, J. S. Keist, E. W. Reutzel, and T. J. Spurgeon, “Intra-layer closed-loop control of build plan during directed energy additive manufacturing of Ti-6Al-4V,” *Additive Manufacturing*, vol. 6, pp. 39–52, 2015, doi: 10.1016/j.addma.2015.03.005.
[36] M. Mukherjee, “Effect of build geometry and orientation on microstructure and properties of additively manufactured 316L stainless steel by laser metal deposition,” *Materialia*, vol. 7, no. April, pp. 5–8, 2019, doi: 10.1016/j.mtla.2019.100359.
[37] K. S. B. Ribeiro, F. E. Mariani, and R. T. Coelho, “A Study of Different Deposition Strategies in Direct Energy Deposition (DED) Processes,” *Procedia Manufacturing*, vol. 48, no. 2019, pp. 663–670, 2020, doi: 10.1016/j.promfg.2020.05.158.
[38] Q. Chen, J. Liu, X. Liang, and A. C. To, “A level-set based continuous scanning path optimization method for reducing residual stress and deformation in metal additive manufacturing,” *Computer Methods in Applied Mechanics and Engineering*, vol. 360, Mar. 2020, doi: 10.1016/j.cma.2019.112719.
[39] K. L. Terrassa, T. R. Smith, S. Jiang, J. D. Sugar, and J. M. Schoenung, “Improving build quality in Directed Energy Deposition by cross-hatching,” *Materials Science and Engineering A*, vol. 765, no. August, p. 138269, 2019, doi: 10.1016/j.msea.2019.138269.
[40] M. Gao, Z. Wang, X. Li, and X. Zeng, “The effect of deposition patterns on the deformation of substrates during direct laser fabrication,” *Journal of Engineering Materials and Technology, Transactions of the ASME*, 2013, doi: 10.1115/1.4024195.
[41] M. A. Somashekara, M. Naveenkumar, A. Kumar, C. Viswanath, and S. Simhambhatla, “Investigations into effect of weld-deposition pattern on residual stress evolution for metallic additive manufacturing,” *International Journal of Advanced Manufacturing Technology*, vol. 90, no. 5–8, pp. 2009–2025, 2017, doi: 10.1007/s00170-016-9510-7.
[42] J. Singh, G. Kumar, and N. Garg, “Influence of vibrations in arc welding over mechanical properties and microstructure of butt-welded-joints,” vol. 2, no. 1, 2012.
[43] T. Watanabe, M. Shiroki, A. Yanagisawa, and T. Sasaki, “Improvement of mechanical properties of ferritic stainless steel weld metal by ultrasonic vibration,” *Journal of Materials Processing Technology*, vol. 210, no. 12, pp. 1646–1651, Sep. 2010, doi: 10.1016/j.jmatprotec.2010.05.015.
[44] D. M. Stefanescu, Ed., “Classification and Basic Types of Cast Iron[1],” in *Cast Iron Science and Technology*, ASM International, 2017, pp. 12–27. doi: 10.31399/asm.hb.v01a.a0006294.
[45] D. M. Stefanescu, Ed., “Specification, Selection, and Applications of Compacted Graphite Irons,” in *Cast Iron Science and Technology*, ASM International, 2017, pp. 659–664. doi: 10.31399/asm.hb.v01a.a0006312.
[46] D. M. Stefanescu, Ed., “Specification, Selection, and Applications of High-Alloy Iron Castings,” in *Cast Iron Science and Technology*, ASM International, 2017, pp. 689–707. doi: 10.31399/asm.hb.v01a.a0006341.
[47] D. M. Stefanescu, Ed., “A History of Cast Iron,” in *Cast Iron Science and Technology*, ASM International, 2017, pp. 3–11. doi: 10.31399/asm.hb.v01a.a0006320.
[48] D. M. Stefanescu, Ed., “Specifications and Selection of Gray Irons,” in *Cast Iron Science and Technology*, ASM International, 2017, pp. 527–560. doi: 10.31399/asm.hb.v01a.a0006308.
[49] D. M. Stefanescu, Ed., “Specification and Selection of Ductile Irons,” in *Cast Iron Science and Technology*, ASM International, 2017, pp. 593–597. doi: 10.31399/asm.hb.v01a.a0006325.

[50] M. Ngqase and X. Pan, “An Overview on Types of White Cast Irons and High Chromium White Cast Irons,” *J. Phys.: Conf. Ser.*, vol. 1495, no. 1, p. 012023, Mar. 2020, doi: 10.1088/1742-6596/1495/1/012023.
[51] D. M. Stefanescu, Ed., “Malleable Iron Castings[1],” in *Cast Iron Science and Technology*, ASM International, 2017, pp. 735–746. doi: 10.31399/asm.hb.v01a.a0006333.
[52] A. Saboori, A. Aversa, G. Marchese, S. Biamino, M. Lombardi, and P. Fino, “Application of directed energy deposition-based additive manufacturing in repair,” *Applied Sciences (Switzerland)*. 2019. doi: 10.3390/app9163316.
[53] S. Kou, *Welding Metallurgy*. Hoboken, NJ: Wiley-Interscience, 2003.
[54] F. T. Cheng, K. H. Lo, and H. C. Man, “A preliminary study of laser cladding of AISI 316 stainless steel using preplaced NiTi wire,” *Materials Science and Engineering A*, vol. 380, no. 1, pp. 20–29, 2004, doi: 10.1016/j.msea.2004.01.056.
[55] W. E. Frazier, “Metal additive manufacturing: A review,” *Journal of Materials Engineering and Performance*, vol. 23, no. 6, pp. 1917–1928, 2014, doi: 10.1007/s11665-014-0958-z.
[56] R. P. Martukanitz, “Directed-Energy Deposition Processes,” *Additive Manufacturing Processes*, vol. 24, pp. 220–238, 2020, doi: 10.31399/asm.hb.v24.a0006549.
[57] S. Wolff, T. Lee, E. Faierson, K. Ehmann, and J. Cao, “Anisotropic properties of directed energy deposition (DED)-processed Ti–6Al–4V,” *Journal of Manufacturing Processes*, vol. 24, pp. 397–405, 2016, doi: 10.1016/j.jmapro.2016.06.020.
[58] J. Yu, Y. Choi, D. Shim, and S. Park, “Repairing casting part using laser assisted additive metal-layer deposition and its mechanical properties,” *Optics and Laser Technology*, vol. 106, pp. 87–93, 2018, doi: 10.1016/j.optlastec.2018.04.007.
[59] B. Edenhofer, D. Joritz, M. Rink, and K. Voges, “Carburizing of steels,” in *Thermochemical Surface Engineering of Steels*, E. J. Mittemeijer and A. J. Marcel, Eds., 2015, pp. 485–553. doi: https://doi.org/10.1016/C2013-0-16318-0.
[60] X. Tong, H. Zhou, L. quan Ren, Z. hui Zhang, R. dong Cui, and W. Zhang, “Thermal fatigue characteristics of gray cast iron with non-smooth surface treated by laser alloying of Cr powder,” *Surface and Coatings Technology*, vol. 202, no. 12, pp. 2527–2534, 2008, doi: 10.1016/j.surfcoat.2007.09.014.
[61] F. Arias-González *et al.*, “Fiber laser cladding of nickel-based alloy on cast iron,” *Applied Surface Science*, vol. 374, pp. 197–205, 2016, doi: 10.1016/j.apsusc.2015.11.023.
[62] Y. Li *et al.*, “Deep pit repairing of nodular cast iron by laser cladding NiCu/Fe-36Ni low-expansion composite alloy,” *Materials Characterization*, vol. 151, no. November 2018, pp. 273–279, 2019, doi: 10.1016/j.matchar.2019.03.021.
[63] Z. Lestan, M. Milfelner, J. Balic, M. Brezocnik, and I. Karabegovic, “Laser deposition of Metco 15E, Colmony 88 and VIM CRU 20 powders on cast iron and low carbon steel,” *International Journal of Advanced Manufacturing Technology*, vol. 66, no. 9–12, pp. 2023–2028, 2013, doi: 10.1007/s00170-012-4478-4.
[64] R. Gonzalez, M. Cadenas, R. Fernandez, J. L. Cortizo, and E. Rodriguez, “Wear behavior of flame sprayed NiCrBSi coating remelted by flame or by laser,” *Wear*, vol. 262, no. 3–4, pp. 301–307, 2007, doi: 10.1016/j.wear.2006.05.009.
[65] A. R. Zulhishamuddin, S. N. Aqida, and M. Mohd Rashidi, “A comparative study on wear behaviour of Cr/Mo surface modified grey cast iron,” *Optics and Laser Technology*, vol. 104, pp. 164–169, 2018, doi: 10.1016/j.optlastec.2018.02.027.
[66] J. H. Yu, K. Y. Lee, D. S. Shim, and S. H. Park, “Characterization of mechanical behavior in repaired FC300 using directly deposited AISI-P21 and AISI-H13 metal powders,” *Proceedings of the Institution of Mechanical Engineers, Part B: Journal of Engineering Manufacture*, 2020, doi: 10.1177/0954405419843754.
[67] Z. Weng, A. Wang, Y. Wang, D. Xiong, and H. Tang, “Diode laser cladding of Fe-based alloy on ductile cast iron and related interfacial behavior,” *Surface and Coatings Technology*, vol. 286, pp. 64–71, 2016, doi: 10.1016/j.surfcoat.2015.12.031.

[68] S. Lee, J. Kim, D. S. Shim, S. H. Park, and Y. S. Choi, “Micro-Cracking in Medium-Carbon Steel Layers Additively Deposited on Gray Cast Iron Using Directed Energy Deposition,” *Metals and Materials International*, 2020, doi: 10.1007/s12540-019-00589-5.
[69] V. Ocelík, U. de Oliveira, M. de Boer, and J. T. M. de Hosson, “Thick Co-based coating on cast iron by side laser cladding: Analysis of processing conditions and coating properties,” *Surface and Coatings Technology*, vol. 201, no. 12, pp. 5875–5883, 2007, doi: 10.1016/j.surfcoat.2006.10.044.
[70] M. Pouranvari, “On the weldability of grey cast iron using nickel based filler metal,” *Materials and Design*, vol. 31, no. 7, pp. 3253–3258, 2010, doi: 10.1016/j.matdes.2010.02.034.
[71] M. Pascual, J. Cembrero, F. Salas, and M. P. Martínez, “Analysis of the weldability of ductile iron,” *Materials Letters*, vol. 62, no. 8, pp. 1359–1362, Mar. 2008, doi: 10.1016/j.matlet.2007.08.070.
[72] U. Jansson and E. Lewin, “Sputter deposition of transition-metal carbide films — A critical review from a chemical perspective,” *Thin Solid Films*, vol. 536, pp. 1–24, Jun. 2013, doi: 10.1016/j.tsf.2013.02.019.
[73] G. Hägg, *Z. Physiol. Chem.*, vol. 12, p. 33, 1931.
[74] D. Ding, Z. Pan, D. Cuiuri, and H. Li, “Wire-feed additive manufacturing of metal components: technologies, developments and future interests,” *International Journal of Advanced Manufacturing Technology*, vol. 81, no. 1–4, pp. 465–481, 2015, doi: 10.1007/s00170-015-7077-3.
[75] J. N. Rousseau, A. Bois-Brochu, and C. Blais, “Effect of oxygen content in new and reused powder on microstructural and mechanical properties of Ti6Al4V parts produced by directed energy deposition,” *Additive Manufacturing*, vol. 23, no. March, pp. 197–205, 2018, doi: 10.1016/j.addma.2018.08.011.
[76] W. U. H. Syed, A. J. Pinkerton, and L. Li, “A comparative study of wire feeding and powder feeding in direct diode laser deposition for rapid prototyping,” *Applied Surface Science*, vol. 247, no. 1–4, pp. 268–276, 2005, doi: 10.1016/j.apsusc.2005.01.138.
[77] K. Kellens, R. Mertens, D. Paraskevas, W. Dewulf, and J. R. Duflou, “Environmental Impact of Additive Manufacturing Processes: Does AM Contribute to a More Sustainable Way of Part Manufacturing?,” in *Procedia CIRP*, 2017, pp. 582–587. doi: 10.1016/j.procir.2016.11.153.
[78] K. M. Taminger and R. A. Hafley, “Electron Beam Freeform Fabrication for Cost Effective Near-Net Shape Manufacturing,” in *NATO/RTO AVT-139 Specialists: Meeting on Cost Effective Manufacture via Net Shape Processing*, 2006, pp. 1–19.
[79] W. B. Harris, *Health and Safety in Powder Metal Handling*. Oak Ridge, TN, 1957.
[80] B. Borges, L. Quintino, R. M. Miranda, and P. Carr, “Imperfections in laser clading with powder and wire fillers,” *International Journal of Advanced Manufacturing Technology*, vol. 50, no. 1–4, pp. 175–183, 2010, doi: 10.1007/s00170-009-2480-2.
[81] J. C. Heigel, M. F. Gouge, P. Michaleris, and T. A. Palmer, “Selection of powder or wire feedstock material for the laser cladding of Inconel® 625,” *Journal of Materials Processing Technology*, vol. 231, pp. 357–365, 2016, doi: 10.1016/j.jmatprotec.2016.01.004.
[82] T. E. Abioye, P. K. Farayibi, and A. T. Clare, “A comparative study of Inconel 625 laser cladding by wire and powder feedstock,” *Materials and Manufacturing Processes*, vol. 32, no. 14, pp. 1653–1659, 2017, doi: https://doi.org/10.1080/10426914.2017.1317787.
[83] B. Blinn *et al.*, “Process-influenced fatigue behavior of AISI 316L manufactured by powder- and wire-based Laser Direct Energy Deposition,” *Materials Science and Engineering A*, vol. 818, 2021, doi: doi.org/10/1016/j.msea.2021.141383.
[84] S. D. Sun *et al.*, “Effect of laser clad repair on the fatigue behaviour of ultra-high strength AISI 4340 steel,” *Materials Science and Engineering A*, vol. 606, pp. 46–57, Jun. 2014, doi: 10.1016/j.msea.2014.03.077.
[85] W. Cong and F. Ning, “A fundamental investigation on ultrasonic vibration-assisted laser engineered net shaping of stainless steel,” *International Journal of Machine Tools and Manufacture*, vol. 121, no. February, pp. 61–69, 2017, doi: 10.1016/j.ijmachtools.2017.04.008.

[86] D. Yuan, S. Shao, C. Guo, F. Jiang, and J. Wang, “Grain refining of Ti-6Al-4V alloy fabricated by laser and wire additive manufacturing assisted with ultrasonic vibration,” *Ultrasonics Sonochemistry*, vol. 73, p. 105472, 2021, doi: 10.1016/j.ultsonch.2021.105472.
[87] K. Kocatepe and C. F. Burdett, “Effect of low frequency vibration on macro and micro structures of LM6 alloys,” *Journal of Materials Science*, vol. 35, no. 13, pp. 3327–3335, 2000, doi: 10.1023/A:1004891809731.
[88] C. J. Todaro *et al.*, “Grain structure control during metal 3D printing by high-intensity ultrasound,” *Nature Communications*, vol. 11, no. 1, p. 142, Dec. 2020, doi: 10.1038/s41467-019-13874-z.
[89] C. J. Todaro, M. A. Easton, D. Qiu, M. Brandt, D. H. StJohn, and M. Qian, “Grain refinement of stainless steel in ultrasound-assisted additive manufacturing,” *Additive Manufacturing*, vol. 37, no. April 2020, p. 101632, 2021, doi: 10.1016/j.addma.2020.101632.
[90] C. Zhang, M. Gao, and X. Zeng, “Workpiece vibration augmented wire arc additive manufacturing of high strength aluminum alloy,” *Journal of Materials Processing Technology*, vol. 271, no. March, pp. 85–92, 2019, doi: 10.1016/j.jmatprotec.2019.03.028.
[91] W. Cong and F. Ning, “A fundamental investigation on ultrasonic vibration-assisted laser engineered net shaping of stainless steel,” *International Journal of Machine Tools and Manufacture*, vol. 121, no. February, pp. 61–69, 2017, doi: 10.1016/j.ijmachtools.2017.04.008.
[92] J. Tsujino, T. Sano, H. Ogata, S. Tanaka, and Y. Harada, “Complex vibration ultrasonic welding systems with large area welding tips,” *Ultrasonics*, vol. 40, no. 1, pp. 361–364, May 2002, doi: 10.1016/S0041-624X(02)00122-1.
[93] W. Chen, Y. Chen, T. Zhang, T. Wen, Z. Yin, and X. Feng, “Effect of ultrasonic vibration and interpass temperature on microstructure and mechanical properties of Cu-8Al-2Ni-2Fe-2Mn alloy fabricated by wire arc additive manufacturing,” *Metals*, vol. 10, no. 2, 2020, doi: 10.3390/met10020215.
[94] Q. Ma *et al.*, “Effects of Ultrasonic Vibration on Microstructure, Mechanical Properties, and Fracture Mode of Inconel 625 Parts Fabricated by Cold Metal Transfer Arc Additive Manufacturing,” *J. of Materi Eng and Perform*, vol. 30, no. 9, pp. 6808–6820, Sep. 2021, doi: 10.1007/s11665-021-06023-5.
[95] E. Foroozmehr, D. Lin, and R. Kovacevic, “Application of vibration in the laser powder deposition process,” *Journal of Manufacturing Processes*, vol. 11, no. 1, pp. 38–44, Jan. 2009, doi: 10.1016/j.jmapro.2009.07.002.
[96] N. Hansen, “Hall-petch relation and boundary strengthening,” *Scripta Materialia*, vol. 51, no. 8 SPEC. ISS., pp. 801–806, Oct. 2004, doi: 10.1016/j.scriptamat.2004.06.002.
[97] N. Chawla and K. K. Chawla, *Metal matrix composites*, vol. 9781461495. 2013. doi: 10.1007/978-1-4614-9548-2.
[98] C. Li, S. Sun, C. Liu, Q. Lu, P. Ma, and Y. Wang, “Microstructure and mechanical properties of TiC/AlSi10Mg alloy fabricated by laser additive manufacturing under high-frequency micro-vibration,” *Journal of Alloys and Compounds*, vol. 794, pp. 236–246, 2019, doi: 10.1016/j.jallcom.2019.04.287.
[99] D. Yuan *et al.*, “Improvement of the grain structure and mechanical properties of austenitic stainless steel fabricated by laser and wire additive manufacturing assisted with ultrasonic vibration,” *Materials Science and Engineering A*, vol. 813, no. March, p. 141177, 2021, doi: 10.1016/j.msea.2021.141177.
[100] J. Bennett *et al.*, “Repairing Automotive Dies with Directed Energy Deposition: Industrial Application and Life Cycle Analysis,” *Journal of Manufacturing Science and Engineering, Transactions of the ASME*, 2019, doi: 10.1115/1.4042078.
[101] J. D. Hamilton *et al.*, “Property-structure-process relationships in dissimilar material repair with directed energy deposition: Repairing gray cast iron using stainless steel 316L,” *Journal of Manufacturing Processes*, vol. 81, pp. 27–34, Sep. 2022, doi: 10.1016/j.jmapro.2022.06.015.

[102] E. Fernández, M. Cadenas, R. González, C. Navas, R. Fernández, and J. D. Damborenea, "Wear behaviour of laser clad NiCrBSi coating," *Wear*, vol. 259, no. 7–12, pp. 870–875, 2005, doi: 10.1016/j.wear.2005.02.063.
[103] Z. Lestan, M. Milfelner, J. Balic, M. Brezocnik, and I. Karabegovic, "Laser deposition of Metco 15E, Colmony 88 and VIM CRU 20 powders on cast iron and low carbon steel," *International Journal of Advanced Manufacturing Technology*, vol. 66, no. 9–12, pp. 2023–2028, 2013, doi: 10.1007/s00170-012-4478-4.
[104] J. D. Hamilton, S. Sorondo, B. Li, H. Qin, and I. V. Rivero, "Mechanical behavior of bimetallic stainless steel and gray cast iron repairs via directed energy deposition additive manufacturing," *Journal of Manufacturing Processes*, vol. 85, no. December 2022, pp. 1197–1207, 2023, doi: 10.1016/j.jmapro.2022.12.029.
[105] ASTM, "E384-22: Standard Test Method for Microindentation Hardness of Materials," *Book of Standards*, vol. 03.01, p. 40, Nov. 2022, doi: 10.1520/E0384-22.
[106] ASTM, "E8: Standard test methods for tension testing of metallic materials metric," *Annual book of ASTM standards*, vol. 3, pp. 57–72, 2016, doi: 10.1520/E0008.
[107] S. Kou and Y. K. Yang, "Fusion-Boundary Macrosegregation in Dissimilar-Filler Welds," *Welding journal*, vol. 86, no. 10, pp. 303s–312s, 2007.
[108] J. F. Lancaster, "9. Austenitic and High-alloy Steels," in *Metallurgy of Welding*, Woodhead Publishing, 1999. Accessed: Jan. 28, 2023. [Online]. Available: https://app-knovel-com.ezproxy.rit.edu/web/view/khtml/show.v/rcid:kpMWE00002/cid:kt003ZOMG1/viewerType:khtml//root_slug:9-austenitic-and-high-alloy-steels/url_slug:austenitic-high-alloy?b-toc-cid=kpMWE00002&b-toc-title=Metallurgy%20of%20Welding%20%286th%20Edition%29&b-toc-url-slug=austenitic-high-alloy&issue_id=kpMWE00002&view=collapsed&zoom=1
[109] M. Brennan, J. S. Keist, and T. A. Palmer, "Defects in Metal Additive Manufacturing Processes," *Additive Manufacturing Processes*, vol. 24, pp. 277–286, 2020, doi: 10.31399/asm.hb.v24.a0006557.
[110] J. Grubbs, B. C. Sousa, and D. Cote, "Exploration of the Effects of Metallic Powder Handling and Storage Conditions on Flowability and Moisture Content for Additive Manufacturing Applications," *Metals*, vol. 12, no. 4, p. 603, Mar. 2022, doi: 10.3390/met12040603.
[111] H. Siva Prasad, F. Brueckner, and A. F. H. Kaplan, "Powder incorporation and spatter formation in high deposition rate blown powder directed energy deposition," *Additive Manufacturing*, vol. 35, p. 101413, Oct. 2020, doi: 10.1016/j.addma.2020.101413.
[112] D.-G. Ahn, "Directed Energy Deposition (DED) Process: State of the Art," *Int. J. of Precis. Eng. and Manuf.-Green Tech.*, vol. 8, no. 2, pp. 703–742, Mar. 2021, doi: 10.1007/s40684-020-00302-7.
[113] J. Yu, Y. Choi, D. Shim, and S. Park, "Repairing casting part using laser assisted additive metal-layer deposition and its mechanical properties," *Optics and Laser Technology*, vol. 106, pp. 87–93, 2018, doi: 10.1016/j.optlastec.2018.04.007.
[114] H. Gunasekara, J. Gamage, and H. Punchihewa, "Remanufacture for sustainability: Barriers and solutions to promote automotive remanufacturing," *Procedia Manufacturing*, vol. 43, no. 2019, pp. 606–613, 2020, doi: 10.1016/j.promfg.2020.02.146.
[115] H. Vasudevan, V. Kalamkar, and R. Terkar, "Remanufacturing for Sustainable Development: Key Challenges, Elements, and Benefits," *International Journal of Innovation, Management and Technology*, vol. 3, no. 1, pp. 84–89, 2012.
[116] J. D. Hamilton, S. Sorondo, B. Li, H. Qin, and I. V. Rivero, "Mechanical behavior of bimetallic stainless steel and gray cast iron repairs via directed energy deposition additive manufacturing," *Journal of Manufacturing Processes*, vol. 85, pp. 1197–1207, Jan. 2023, doi: 10.1016/j.jmapro.2022.12.029.
[117] Y. Li *et al.*, "Microstructure characteristics and mechanical properties of new-type FeNiCr laser cladding alloy coating on nodular cast iron," *Journal of Materials Processing Technology*, vol. 269, no. August 2018, pp. 163–171, 2019, doi: 10.1016/j.jmatprotec.2019.02.010.

[118] G. Piscopo, E. Atzeni, A. Saboori, and A. Salmi, “An Overview of the Process Mechanisms in the Laser Powder Directed Energy Deposition,” *Applied Sciences*, vol. 13, no. 1, p. 117, Dec. 2022, doi: 10.3390/app13010117.
[119] R. P. Martukanitz, “Directed-Energy Deposition Processes,” *Additive Manufacturing Processes*, vol. 24, pp. 220–238, 2020, doi: 10.31399/asm.hb.v24.a0006549.
[120] A. E. Wilson-Heid, T. C. Novak, and A. M. Beese, “Characterization of the Effects of Internal Pores on Tensile Properties of Additively Manufactured Austenitic Stainless Steel 316L,” *Exp Mech*, vol. 59, no. 6, pp. 793–804, Jul. 2019, doi: 10.1007/s11340-018-00465-0.
[121] H. Gong, K. Rafi, H. Gu, G. D. Janaki Ram, T. Starr, and B. Stucker, “Influence of defects on mechanical properties of Ti–6Al–4V components produced by selective laser melting and electron beam melting,” *Materials & Design*, vol. 86, pp. 545–554, Dec. 2015, doi: 10.1016/j.matdes.2015.07.147.
[122] M. Motta, A. G. Demir, and B. Previtali, “High-speed imaging and process characterization of coaxial laser metal wire deposition,” *Additive Manufacturing*, vol. 22, no. February, pp. 497–507, 2018, doi: 10.1016/j.addma.2018.05.043.
[123] C. Ma *et al.*, “Investigation of In Situ Vibration During Wire and Arc Additive Manufacturing,” *3D Printing and Additive Manufacturing*, Nov. 2021, doi: 10.1089/3dp.2021.0053.
[124] S. Zhou, B. Wang, D. Wu, G. Ma, G. Yang, and W. Wei, “Follow-up ultrasonic vibration assisted laser welding dissimilar metals for nuclear reactor pump can end sealing,” *Nuclear Materials and Energy*, vol. 27, p. 100975, Jun. 2021, doi: 10.1016/j.nme.2021.100975.
[125] G. I. Eskin and D. G. Eskin, *Ultrasonic Treatment of Light Alloy Melts, Second Edition*. CRC Press, 2014.
[126] W. Chen, Y. Chen, T. Zhang, T. Wen, Z. Yin, and X. Feng, “Effect of ultrasonic vibration and interpass temperature on microstructure and mechanical properties of Cu-8Al-2Ni-2Fe-2Mn alloy fabricated by wire arc additive manufacturing,” *Metals*, vol. 10, no. 2, 2020, doi: 10.3390/met10020215.
[127] G. Manogharan, B. Yelamanchi, R. Aman, and Z. Mahbooba, “Experimental Study of Disruption of Columnar Grains During Rapid Solidification in Additive Manufacturing,” *JOM*, vol. 68, no. 3, pp. 842–849, Mar. 2016, doi: 10.1007/s11837-015-1800-2.
[128] C. J. Todaro, M. A. Easton, D. Qiu, M. Brandt, D. H. StJohn, and M. Qian, “Grain refinement of stainless steel in ultrasound-assisted additive manufacturing,” *Additive Manufacturing*, vol. 37, no. April 2020, p. 101632, 2021, doi: 10.1016/j.addma.2020.101632.
[129] X. Ji, E. Mirkoohi, J. Ning, and S. Y. Liang, “Analytical modeling of post-printing grain size in metal additive manufacturing,” *Optics and Lasers in Engineering*, vol. 124, no. July 2019, p. 105805, 2020, doi: 10.1016/j.optlaseng.2019.105805.
[130] C. Li, S. Sun, C. Liu, Q. Lu, P. Ma, and Y. Wang, “Microstructure and mechanical properties of TiC/AlSi10Mg alloy fabricated by laser additive manufacturing under high-frequency micro-vibration,” *Journal of Alloys and Compounds*, vol. 794, pp. 236–246, 2019, doi: 10.1016/j.jallcom.2019.04.287.
[131] E. Ingram, O. Golan, R. Haj-Ali, and N. Eliaz, “The Effect of Localized Vibration during Welding on the Microstructure and Mechanical Behavior of Steel Welds,” *Materials*, vol. 12, no. 16, Art. no. 16, Jan. 2019, doi: 10.3390/ma12162553.
[132] S. Zhou, G. Ma, W. Dongjiang, D. Chai, and M. Lei, “Ultrasonic vibration assisted laser welding of nickel-based alloy and Austenite stainless steel,” *Journal of Manufacturing Processes*, vol. 31, pp. 759–767, Jan. 2018, doi: 10.1016/j.jmapro.2017.12.023.
[133] D. Yuan, S. Shao, C. Guo, F. Jiang, and J. Wang, “Grain refining of Ti-6Al-4V alloy fabricated by laser and wire additive manufacturing assisted with ultrasonic vibration,” *Ultrasonics Sonochemistry*, vol. 73, p. 105472, 2021, doi: 10.1016/j.ultsonch.2021.105472.
[134] D. Yuan *et al.*, “Improvement of the grain structure and mechanical properties of austenitic stainless steel fabricated by laser and wire additive manufacturing assisted with ultrasonic vibration,”

Materials Science and Engineering A, vol. 813, no. March, p. 141177, 2021, doi: 10.1016/j.msea.2021.141177.
[135] Z. Lei, J. Bi, P. Li, Q. Li, Y. Chen, and D. Zhang, "Melt flow and grain refining in ultrasonic vibration assisted laser welding process of AZ31B magnesium alloy," *Optics & Laser Technology*, vol. 108, pp. 409–417, Dec. 2018, doi: 10.1016/j.optlastec.2018.07.015.
[136] Z. Liu, X. Jin, J. Zhang, Z. Hao, and J. Li, "Microstructure evolution and mechanical properties of SUS301L stainless steel sheet welded joint in ultrasonic vibration assisted laser welding," *Optics & Laser Technology*, vol. 153, p. 108193, Sep. 2022, doi: 10.1016/j.optlastec.2022.108193.
[137] Z. Liu, X. Jin, J. Li, Z. Hao, and J. Zhang, "Numerical simulation and experimental analysis on the deformation and residual stress in trailing ultrasonic vibration assisted laser welding," *Advances in Engineering Software*, vol. 172, p. 103200, Oct. 2022, doi: 10.1016/j.advengsoft.2022.103200.
[138] T. Young, "III. An essay on the cohesion of fluids," *Philosophical Transactions of the Royal Society of London*, vol. 95, pp. 65–87, Dec. 1805, doi: 10.1098/rstl.1805.0005.
[139] H. Y. Erbil, "The debate on the dependence of apparent contact angles on drop contact area or three-phase contact line: A review," *Surface Science Reports*, vol. 69, no. 4, pp. 325–365, Dec. 2014, doi: 10.1016/j.surfrep.2014.09.001.
[140] K. L. Mittal, Ed., *Contact Angle, Wettability and Adhesion, Volume 3*. London: CRC Press, 2003. doi: 10.1201/9789047403326.
[141] R. Galleguillos-Silva, Y. Vargas-Hernández, and L. Gaete-Garretón, "Wettability of a surface subjected to high frequency mechanical vibrations," *Ultrasonics Sonochemistry*, vol. 35, pp. 134–141, Mar. 2017, doi: 10.1016/j.ultsonch.2016.09.011.
[142] Y. M. Wang *et al.*, "Additively manufactured hierarchical stainless steels with high strength and ductility," *Nature Mater*, vol. 17, no. 1, Art. no. 1, Jan. 2018, doi: 10.1038/nmat5021.
[143] K. Saeidi and F. Akhtar, "Subgrain-controlled grain growth in the laser-melted 316 L promoting strength at high temperatures," *Royal Society Open Science*, vol. 5, no. 5, p. 172394, May 2018, doi: 10.1098/rsos.172394.
[144] J. Wanni, J. G. Michopoulos, and A. Achuthan, "Influence of cellular subgrain feature on mechanical deformation and properties of directed energy deposited stainless steel 316 L," *Additive Manufacturing*, vol. 51, p. 102603, Mar. 2022, doi: 10.1016/j.addma.2022.102603.
[145] G. K. Padhy, C. S. Wu, S. Gao, and L. Shi, "Local microstructure evolution in Al 6061-T6 friction stir weld nugget enhanced by ultrasonic vibration," *Materials & Design*, vol. 92, pp. 710–723, Feb. 2016, doi: 10.1016/j.matdes.2015.12.094.
[146] K. Ogata, *System Dynamics*. Pearson Education Limited, 2013.
[147] A. Ghatak, *Optics*. McGraw-Hill, 2005.
[148] K. Kocatepe and C. F. Burdett, "Effect of low frequency vibration on macro and micro structures of LM6 alloys," *Journal of Materials Science*, vol. 35, no. 13, pp. 3327–3335, 2000, doi: 10.1023/A:1004891809731.

Appendix A - Property-Structure-Process Relationships in Dissimilar Material Repair with Directed Energy Deposition: Repairing Gray Cast Iron using Stainless Steel 316L

The following journal article founded a basis in laser DED-based repair of gray cast iron and the structural reliance on process parameters. It was published in the Journal of Manufacturing Processes and appeared in Volume 81, September 2022, pages 27-34, DOI: https://doi-org.ezproxy.rit.edu/10.1016/j.jmapro.2022.06.015

Journal of Manufacturing Processes 81 (2022) 27–34

Contents lists available at ScienceDirect

Journal of Manufacturing Processes

journal homepage: www.elsevier.com/locate/manpro

Property-structure-process relationships in dissimilar material repair with directed energy deposition: Repairing gray cast iron using stainless steel 316L

Jakob D. Hamilton [a], Samantha Sorondo [a], Andrew Greeley [a], Xiao Zhang [b], Denis Cormier [a], Beiwen Li [c], Hantang Qin [b], Iris V. Rivero [a,*]

[a] Department of Industrial and Systems Engineering, Rochester Institute of Technology, One Lomb Memorial Drive, Rochester, NY 14623, United States of America
[b] Department of Industrial and Manufacturing Systems Engineering, Iowa State University, 2529 Union Drive, Ames, IA 50011, United States of America
[c] Mechanical Engineering Department, Iowa State University, 2529 Union Drive, Ames, IA 50011, United States of America

ARTICLE INFO

Keywords:
Additive manufacturing
Repair
Directed energy deposition
Gray cast iron

ABSTRACT

Directed energy deposition (DED) based remanufacturing leverages the flexibility of additive manufacturing to add value to broken or worn components. DED offers the ability to repair cast iron, a material difficult to repair with traditional welding techniques. Despite this, development of appropriate DED process conditions for bimetallic cast iron structures lags low- and medium-carbon steel repair. Thermal stresses and porosity generated by high-temperature deposition on cast iron often lower mechanical properties and hinder the qualification process. Herein, scanning speed, powder mass flow rate, and stepover width are studied in multiple-track structures deposited on gray cast iron. Dilution and residual stresses are found to be highly dependent on the selected process parameters. Samples with a higher volumetric energy input, e.g., slower scanning speeds and higher powder feed rates, showed improved density and lower residual stresses but suffered lower dilution into the substrate. The presented conditions further the development of additive manufacturing technologies for automotive repair.

1. Introduction

Additive manufacturing through directed energy deposition (DED) offers a new approach for repair and remanufacturing of high-value components. In DED, powder or wire feedstock is inserted into a high-intensity energy source, and the melted material is selectively deposited until a prescribed geometry is formed. The localized nature of this process, i.e., energy and material delivery occurring at a single location, makes it ideal for building up worn surfaces, mending fractures, or replacing missing geometrical features.

Lower thermal conditions in DED make it favorable for repair of cast iron components such as engine heads. Cast iron repair via DED benefits from the smaller heat affected zone (HAZ) and lower dilution compared to traditional welding processes. Yu et al. showed that laser cladding produced a HAZ 21 times smaller than shielded metal arc welding [1]. The authors attributed an increase in elongation to the smaller martensitic volume formed during the repair. Pouranvari showed the sensitivity of the HAZ to brittle fracture due to martensitic formation during welding [2]. Gouveia et al. also noted brittle ledeburitic formations at the weld interface, despite preheating and post-welding heat treatment [3]. Premature fracturing in the HAZ was the primary mode of failure during tensile testing. These studies note that careful control of the thermal cycle during shielded metal arc welding or post-weld heat treatment is necessary to regain ductility in the interfacial repair region. Pascual et al. also considered Ni- and Ni—Fe filler materials in cast iron welding [4]. While more expensive than Fe-based filler materials, 97.6 % Ni electrodes increased the weld ductility by decreasing the pearlitic concentration and size of graphite nodules in the heat affected zone. Preheating at 350 °C and annealing at 850 °C also improved sample ductility [4]. The high thermal input and cooling rates during welding may negate the beneficial carbon diffusion of Ni filler materials on cast iron [5]. Careful thermal control is required to minimize residual stresses that propagate through the weld zones and initiate cracks at graphite nodules and high hardness phases [3,6].

Despite having lower heat input, challenges during DED-based repair arise due to carbon nodules or flakes present in cast iron. Ocelík et al.

* Corresponding author at: Rochester Institute of Technology, One Lomb Memorial Drive, Rochester, NY 14623, United States of America.
E-mail address: iris.rivero@rit.edu (I.V. Rivero).

https://doi.org/10.1016/j.jmapro.2022.06.015
Received 17 January 2022; Received in revised form 4 June 2022; Accepted 13 June 2022
Available online 2 July 2022

Appendix B – Mechanical Behavior of Bimetallic Stainless Steel and Gray Cast Iron Repairs via Directed Energy Deposition Additive Manufacturing

The following journal article unveiled pivotal relationships between DED process parameters and structural outcomes in gray cast iron repair. It was published in the Journal of Manufacturing Processes and appeared in Volume 85, January 2023, pages 1197-1207, DOI: https://doi-org.ezproxy.rit.edu/10.1016/j.jmapro.2022.12.029

Journal of Manufacturing Processes 85 (2023) 1197–1207

Contents lists available at ScienceDirect

Journal of Manufacturing Processes

journal homepage: www.elsevier.com/locate/manpro

Mechanical behavior of bimetallic stainless steel and gray cast iron repairs via directed energy deposition additive manufacturing

Jakob D. Hamilton [a], Samantha Sorondo [a], Beiwen Li [b], Hantang Qin [c], Iris V. Rivero [a,*]

[a] Department of Industrial and Systems Engineering, Rochester Institute of Technology, 81 Lomb Memorial Drive, Rochester, NY 14623, United States of America
[b] Department of Mechanical Engineering, Iowa State University, 2529 Union Drive, Ames, IA 50011, United States of America
[c] Department of Industrial and Systems Engineering, University of Wisconsin - Madison, 1415 Engineering Drive, Madison, WI 53706, United States of America

ARTICLE INFO

Keywords:
Additive manufacturing
Repair
Directed energy deposition

ABSTRACT

The utility of gray cast iron in engine components remains tied to the mechanical performance and cost. Repair and remanufacturing of castings offer economical and sustainable benefits; however, high thermal input from traditional fusion-based welding is unable to restore the original mechanical quality owing to brittle microstructures and porosity formed in situ. Directed energy deposition (DED) is an additive manufacturing method that has received considerable interest for repairs owing to the highly controllable nature of the process. Despite this, few works have connected the effect of DED parameters on actual interfacial strength. Consequently, distinct DED parameter combinations were identified to maximize the strength and fatigue life of the repaired cast iron. High speed melt pool imaging and residual stress measurements are provided to aid in the understanding of the metallurgical quality and strength seen in these structures. In general, higher scanning speeds and lower thermal gradients promoted comparable tensile strength to that of the original gray cast iron. The results presented here provide a foundation to tune in the DED process to generate the required mechanical quality as a starting point for future process advancements.

1. Introduction

Gray cast iron is a widely used iron alloy in the automotive and transportation industries. Owing to its high strength and wear resistance, gray cast iron can withstand harsh conditions of engine blocks, mechanical housings, and other large components. Because of the high production costs, repairing or remanufacturing large cast iron components is often advantageous.

Cast iron repair commonly employs oxyacetylene or arc welding with mild steel, cast iron, stainless steel, or nickel alloy filler metal [1–3]. Under careful control, these materials allow for restoration of the original material strength. However, achieving this behavior requires overcoming several major challenges. The rapid melting and solidification promoted by welding forms large thermal gradients and brittle martensite in the heat affected zone (HAZ). Residual stresses driven by the large thermal gradients often result in undetectable fractures at the repair interface [1,2]. Controlling these outcomes requires careful control of the cooling rates in-process [4,5]. Gaseous porosity may also form during fusion-based repairs, further decreasing the mechanical integrity of the repair.

Directed energy deposition (DED) is an additive manufacturing technology that has recently been investigated as an alternative repair technology to welding. Lower heat input in laser-based DED has been offered as an advantage to minimize the thermal gradients and the size of the HAZ [6]. Despite this, micro-fracturing and pore formation at the repair interface deteriorate the repair strength. These defects are driven by the unique thermal conditions promoted in DED and can vary significantly with the selected deposition parameters.

Several studies have been offered to understand how distinct deposition parameters affect the interfacial characteristics of the repair [7–11]. Volatile compounds in the cast iron and trapped carrier gas contributed to microporosity in Ni-based alloy coatings on ductile and gray cast iron [9]. Ocelík et al. provided three recommendations for minimizing gas and inter-run porosity in coatings on cast iron: retain dilution between 5 and 15 %, retain a 100° angle between the cladding sidewall and the substrate, and minimize the amount of shielding gas [7]. Tong et al. added that the lengthened molten state created by slower scanning speeds allowed trapped gases to escape [8]. The reduced

Abbreviations: GCI, Gray Cast Iron; TC, Temperature Controlled; SS316L, Stainless Steel 316 L.

* Corresponding author at: 81 Lomb Memorial Drive, Rochester Institute of Technology, Rochester, NY 14623, United States of America.
E-mail address: iris.rivero@rit.edu (I.V. Rivero).

https://doi.org/10.1016/j.jmapro.2022.12.029
Received 2 August 2022; Received in revised form 13 November 2022; Accepted 12 December 2022
Available online 28 December 2022

Appendix C: Derivation of the Nozzle Motion Equation

The crucial portion of the nozzle motion can be isolated to the axis along the piezoelectric actuator and the *preload* force spring. The system may be simplified to the model in Figure C1.

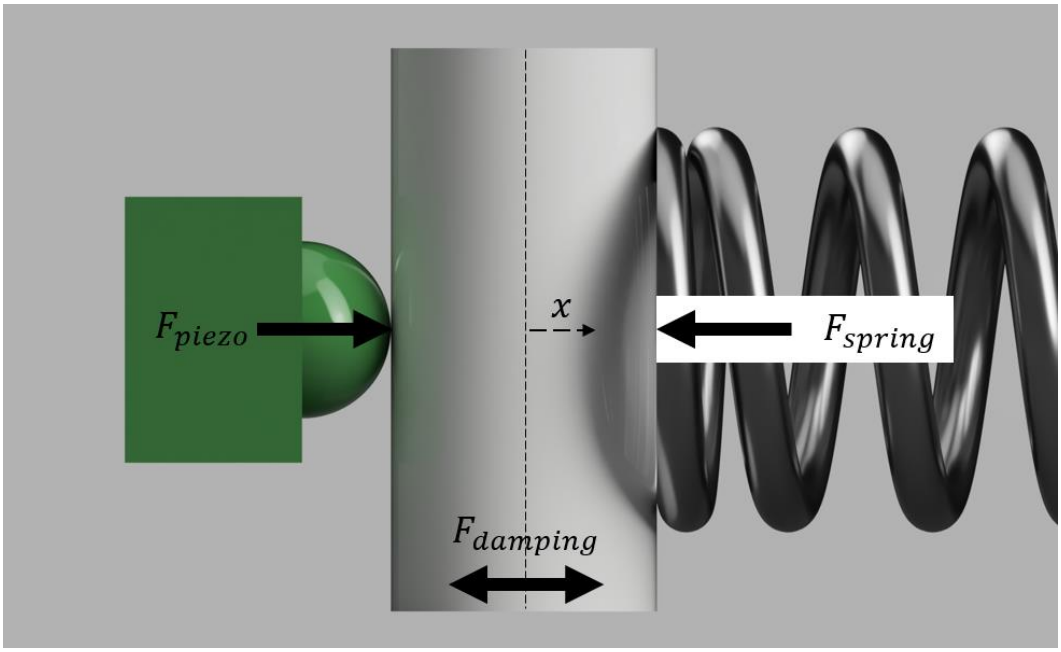

Figure 35. Schematic simplification of the nozzle oscillator with the applied forces.

The spring generates a force negatively proportional to the applied strain (Δx) and spring constant (k), obeying the Hooke's law, which can be rearranged as an acceleration of the inertial mass of the system (m) using Newton's Second Law of Motion:

$$F_{spring} = -k\Delta x \tag{C1}$$

$$\frac{d^2x}{dt^2} = -\left(\frac{k}{m}\right)\Delta x \tag{C2}$$

The damping force naturally generated by friction and fluid drag is considerably more difficult to quantify owing to the transient thermo-mechanical nature of the DED process. Instead, this quantity is expressed in terms of a damping coefficient (γ) and is negatively proportional to the velocity of the wire at any point in time. Again, this quantity can be expressed as an acceleration:

$$F_{damping} = -\gamma m\frac{dx}{dt} \tag{C3}$$

$$\frac{d^2x}{dt^2} = -\gamma \frac{dx}{dt} \tag{C4}$$

Lastly, the transient driving force of the piezo actuator is dictated by the amplified DC square-wave and the intrinsic strain behavior of the piezo. For practical purposes, this force is assumed to follow a cosine function based on the driving frequency (ω_d), the force amplitude (F_0), and time. Because the piezo is not rigidly attached to the wire sheath, it can only apply a *pushing* force. Therefore, the output force must only generate positive magnitude:

$$F_{piezo} = F_0(\cos \omega_d t + 1) \tag{C5}$$

Again, expressing this in terms of acceleration yields:

$$\frac{d^2x}{dt^2} = \frac{F_0}{m}(\cos \omega_d t + 1) \tag{C6}$$

Summing the acceleration caused by each component yields Eq. C7, the motion equation for this system.

$$\frac{d^2x}{dt^2} + \gamma \frac{dx}{dt} + \omega_0^2 x = \frac{F_0}{m}[\cos \omega_d t + 1] \tag{C7}$$

This equation can be described as a 2nd order, nonhomogeneous differential equation. The solution is comprised of the sum of two parts: the complementary and particular solution. The former is found by solving the equivalent homogeneous equation, i.e., setting the right side of the equation to zero and solving for *x*. The 1st and 2nd order differential requires a term that remains after differentiation, a perfect fit for an exponential function with constants (a) and (c).

$$\frac{d^2x}{dt^2} + \gamma \frac{dx}{dt} + \omega_0^2 x = 0 \tag{C8}$$

$$Guess: x(t) = ce^{at} \tag{C9}$$

$$x'(t) = cae^{at} \tag{C10}$$

$$x''(t) = ca^2e^{at} \tag{C11}$$

$$ce^{at}(a^2 + \gamma a + \omega_0^2) = 0 \tag{C12}$$

Because the exponential will never reach zero, the quantity in parentheses must be equal to zero. Finding the solutions to Eq. C13 require use of the quadratic function to find coefficient a.

$$(a^2 + \gamma a + \omega_0^2) = 0 \tag{C13}$$

$$a = -\gamma/2 \pm \sqrt{\gamma^2/4 - \omega_0^2} \tag{C14}$$

Therefore, the complementary solution is defined as:

$$x_c(t) = c_1 e^{At} + c_2 e^{Bt} \tag{C15}$$

$$A = -\gamma/2 + \sqrt{\gamma^2/4 - \omega_0^2} \tag{C16}$$

$$B = -\gamma/2 - \sqrt{\gamma^2/4 - \omega_0^2} \tag{C17}$$

The particular solution can be separated into the sum of two particular solutions:

$$x_{p1}(t) \rightarrow \frac{d^2x}{dt^2} + \gamma \frac{dx}{dt} + \omega_0^2 x = \frac{F_0}{m} \cos \omega_d t \tag{C18}$$

$$x_{p2}(t) \rightarrow \frac{d^2x}{dt^2} + \gamma \frac{dx}{dt} + \omega_0^2 x = \frac{F_0}{m} \tag{C19}$$

The latter of these (Eq. C19) has no transient terms on the right side of the equation, making the solution relatively simple:

$$Guess: x(t) = \frac{F_0}{m\omega_0^2} \tag{C20}$$

$$x''(t) = x'(t) = 0 \tag{C21}$$

$$0 + \gamma \cdot 0 + \omega_0^2 \left(\frac{F_0}{m\omega_0^2} \right) = \frac{F_0}{m} \tag{C22}$$

Thus,

$$x_{p2}(t) = \frac{F_0}{m\omega_0^2} \tag{C23}$$

The particular solution to Eq. C18 is found by guessing a solution with both sine and cosine functions:

$$Guess: x(t) = C \cos \omega_d t + D \sin \omega_d t \tag{C24}$$

$$x'(t) = -C\omega_d \sin \omega_d t + D\omega_d \cos \omega_d t \tag{C25}$$

$$x''(t) = -C\omega_d^2 \cos \omega_d t - D\omega_d^2 \sin \omega_d t \tag{C26}$$

Substituting these expressions into Eq. C18 yields:

$$\{-C\omega_d^2\cos\omega_d t - D\omega_d^2\sin\omega_d t\} + \gamma\{-C\omega_d\sin\omega_d t + D\omega_d\cos\omega_d t\} + \omega_0^2\{C\cos\omega_d t + D\sin\omega_d t\} = \frac{F_0}{m}\cos\omega_d t$$

$$\cos\omega_d t\left[-C\omega_d^2 + D\gamma\omega_d + C\omega_0^2\right] = \frac{F_0}{m}\cos\omega_d t$$

$$C\left(\omega_0^2 - \omega_d^2\right) + D\gamma\omega_d = \frac{F_0}{m} \tag{C27}$$

$$C = \frac{F_0/m - D\gamma\omega_d}{(\omega_0^2 - \omega_d^2)} \tag{C28}$$

$$\sin\omega_d t\left[-D\omega_d^2 - C\gamma\omega_d + D\omega_0^2\right] = 0$$

$$D\left(\omega_0^2 - \omega_d^2\right) - C\gamma\omega_d = 0$$

$$D\left(\omega_0^2 - \omega_d^2\right) - \left[\frac{F_0/m - D\gamma\omega_d}{(\omega_0^2 - \omega_d^2)}\right]\gamma\omega_d = 0$$

$$D\left(\omega_0^2 - \omega_d^2\right)^2 - \frac{F_0}{m}\gamma\omega_d + D\gamma^2\omega_d^2 = 0$$

$$D\left[\left(\omega_0^2 - \omega_d^2\right)^2 + \gamma^2\omega_d^2\right] = \frac{F_0}{m}\gamma\omega_d$$

$$D = \frac{F_0\gamma\omega_d}{m[(\omega_0^2 - \omega_d^2)^2 + \gamma^2\omega_d^2]} \tag{C29}$$

$$C = \frac{F_0}{m(\omega_0^2 - \omega_d^2)}\left[1 - \frac{\gamma^2\omega_d^2}{(\omega_0^2 - \omega_d^2)^2 + \gamma^2\omega_d^2}\right] \tag{C30}$$

Eqs. C29 and C30 are the simplified quantities for the coefficients in the particular solution. Returning these values into Eq. C27 confirms Eq. C24 as a valid solution for the 2nd particular solution.

$$\frac{F_0}{m(\omega_0^2 - \omega_d^2)}\left[1 - \frac{\gamma^2\omega_d^2}{(\omega_0^2 - \omega_d^2)^2 + \gamma^2\omega_d^2}\right]\left(\omega_0^2 - \omega_d^2\right) + \frac{F_0\gamma\omega_d}{m[(\omega_0^2 - \omega_d^2)^2 + \gamma^2\omega_d^2]}\gamma\omega_d = \frac{F_0}{m}$$

$$\frac{F_0}{m}\left[1 - \frac{\gamma^2\omega_d^2}{(\omega_0^2 - \omega_d^2)^2 + \gamma^2\omega_d^2}\right] + \frac{F_0}{m}\left[\frac{\gamma^2\omega_d^2}{(\omega_0^2 - \omega_d^2)^2 + \gamma^2\omega_d^2}\right] = \frac{F_0}{m}$$

$$1 - \left[\frac{\gamma^2\omega_d^2}{(\omega_0^2 - \omega_d^2)^2 + \gamma^2\omega_d^2} - \frac{\gamma^2\omega_d^2}{(\omega_0^2 - \omega_d^2)^2 + \gamma^2\omega_d^2}\right] = 1$$

$$1 = 1$$

Thus,

$$x_{p2}(t) = C\cos\omega_d t + D\sin\omega_d t \tag{C31}$$

$$D = \frac{F_0\gamma\omega_d}{m[(\omega_0^2 - \omega_d^2)^2 + \gamma^2\omega_d^2]} \tag{C32}$$

$$C = \frac{F_0}{m(\omega_0^2 - \omega_d^2)}\left[1 - \frac{\gamma^2\omega_d^2}{(\omega_0^2 - \omega_d^2)^2 + \gamma^2\omega_d^2}\right] \tag{C33}$$

The solution for the motion equation combines the complementary solution (Eqs. C15-C17) with both particular solutions (Eqs. C23 and C31-C33):

$$x(t) = c_1 e^{At} + c_2 e^{Bt} + \frac{F_0}{m\omega_0^2} + C\cos\omega_d t + D\sin\omega_d t \qquad (C34)$$

$$A = -\gamma/2 + \sqrt{\gamma^2/4 - \omega_0^2} \qquad (C35)$$

$$B = -\gamma/2 - \sqrt{\gamma^2/4 - \omega_0^2} \qquad (C36)$$

$$C = \frac{F_0}{m(\omega_0^2 - \omega_d^2)}\left[1 - \frac{\gamma^2\omega_d^2}{(\omega_0^2 - \omega_d^2)^2 + \gamma^2\omega_d^2}\right] \qquad (C37)$$

$$D = \frac{F_0\gamma\omega_d}{m[(\omega_0^2 - \omega_d^2)^2 + \gamma^2\omega_d^2]} \qquad (C38)$$

Appendix D: Tuning and Verification of the Piezo Vibration

Because of the small amplitude and short oscillation period at ultrasonic frequencies, verification of wire vibration became a crucial part to validating the success of the design. This process also became useful for finding resonant frequencies, i.e., where the wire oscillation amplitude is maximized. The chosen method relies on laser reflection and low-speed (<8 Hz) imaging. The verification setup is shown in Figure 36. A red laser is placed next to a camera at a distance far (>2 meters) from the vibration nozzle. Wire is fed through the nozzle to the location where it would theoretically enter the melt pool. The laser is pointed directly at the end of the wire and adjusted such that the signal is reflected directly back into the camera sensor. The specular reflection on the surface of the wire produces a static pattern visible in the camera's images. As the wire displaces, the reflection surface position also changes, creating a displacement in the camera's image. Because the wire vibration frequencies are 2-5 orders of magnitude higher than the image capture frequency, the displacement pattern will blur as the vibration amplitude increases.

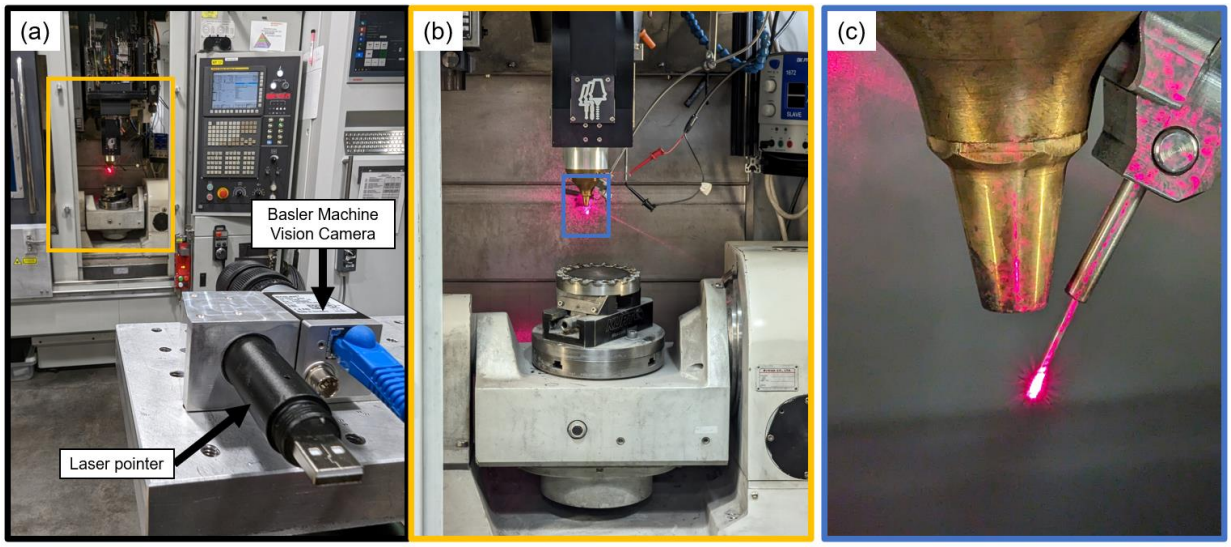

Figure 36. The vibration verification setup. The camera views the reflection of the laser pointer on the wire. Harmonic motion of the wire results in blurring in the camera image. (b) is the close-up image of the inset in (b).

Reflection patterns at select nozzle frequencies are shown in Figure 37. Under 30 kHz, vibration is present in the wire at most frequencies. Several resonant peaks are noted at 2 kHz, 12 kHz, and between

20 kHz and 24 kHz. Above 28 kHz, the amplitude decreases such that any resonant peaks are difficult to locate. These peaks are a function of the mechanics of the nozzle design. Changing the nozzle features such as the preload spring force, the piezo electric element, the mechanical amplification distance, etc, will modify the amplitude peaks.

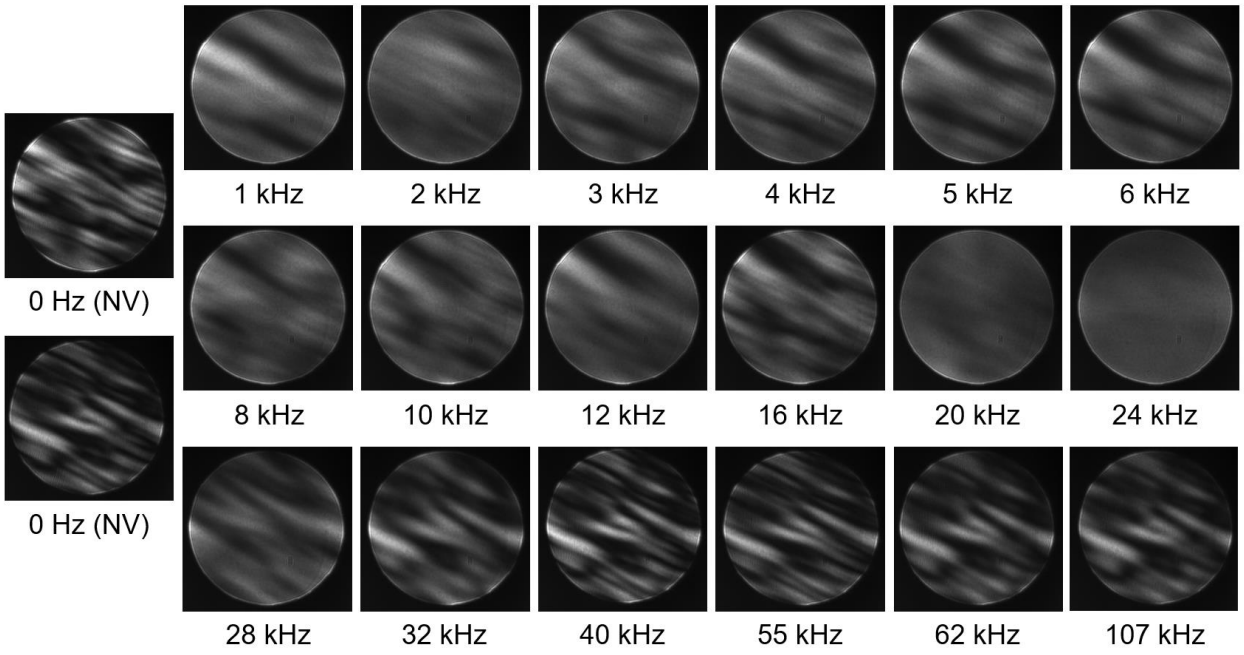

Figure 37. Laser reflection patterns at various driving frequencies for the piezoelectric actuator. Blurring indicates high vibration amplitude.